

PHOTODISSOCIATION DYNAMICS  
OF GROUP V HYDRIDES

by

William P. Schroeder

---

A Dissertation Presented to the  
FACULTY OF THE USC GRADUATE SCHOOL  
UNIVERSITY OF SOUTHERN CALIFORNIA  
In Partial Fulfillment of the  
Requirements for the Degree  
DOCTOR OF PHILOSOPHY  
(CHEMISTRY)

May 2013

Copyright 2013

William P. Schroeder

This dissertation is dedicated to my favorite lab partner, life partner, and best friend,

Christi A. Schroeder.

AΩ

# Table of Contents

<b>Abstract</b>		1
<b>Chapter 1</b>	<b>Relativistic Effects in Chemistry</b>	2
1.1	Introduction	2
1.2	Relativistic Effects	3
	1.2.1 Qualitative Effects	3
	1.2.2 Early Relativistic Quantum Mechanics	8
	1.2.3 Dirac Equation	11
	1.2.4 Relativistic Many-Body Problem	17
1.3	The Potential Energy Surface (PES)	19
1.4	Photodissociation Dynamics	25
1.5	Chapter 1 References	28
<b>Chapter 2</b>	<b>Experimental Methods</b>	30
2.1	Introduction	30
2.2	Time-of-Flight Spectroscopy	30
	2.2.1 Hydrogen Time-of-Flight Spectroscopy	30
	2.2.2 High- <i>n</i> Rydberg Time-of-Flight Spectroscopy	31
2.3	Experimental Setup and Details	32
	2.3.1 Vacuum Chamber and System	32
	2.3.2 Laser Systems	36
	2.3.3 Electronic Control and Detection	37
	2.3.4 System Alignment	38
2.4	Data Collection and Processing	39
2.5	Chapter 2 References	42
<b>Chapter 3</b>	<b>The UV Photodissociation Dynamics of Arsine (AsH<sub>3</sub>)</b>	43
3.1	Introduction	43
3.2	Experimental	50
3.3	Results	51
3.4	Discussion	55
	3.4.2 AsH <sub>2</sub> internal excitations	58
	3.4.3 Secondary Photolysis: AsH <sub>2</sub> → AsH + H	62
3.5	Conclusions	64
3.6	Chapter 3 References	67
<b>Chapter 4</b>	<b>Supplemental Data, Design Considerations and Safety</b>	70
4.1	Introduction	71

4.2	Supplemental Data	71
4.2.1	Antimony Trihydride (SbH <sub>3</sub> )	71
4.2.2	Hydrogen Iodide (HI)	76
4.2.3	Diazirine (c-H <sub>2</sub> N <sub>2</sub> )	81
4.3	Design Analysis and Considerations	83
4.3.1	Vacuum Ultraviolet Generation	83
4.4	Safety	88
4.5	Chapter 4 References	92
<b>Chapter 5</b>	<b>Future Directions</b>	<b>93</b>
5.1	Introduction	93
5.2	AsH <sub>2</sub>	93
5.3	SbH <sub>3</sub> and SbH <sub>2</sub>	95
5.4	BiH <sub>3</sub> and BiH <sub>2</sub>	98
5.5	Chapter 5 References	100
<b>Bibliography</b>		<b>102</b>

## Abstract

This dissertation discusses the ultraviolet photodissociation dynamics and compares important molecular properties of the group-V hydrides ( $\text{NH}_3$ ,  $\text{PH}_3$ ,  $\text{SbH}_3$ , and  $\text{BiH}_3$ ). High- $n$  Rydberg time-of-flight (HRTOF) spectroscopy has been used to study the 193.3 nm photolysis of  $\text{AsH}_3$ . The center-of-mass (c.m.) translational energy distribution for the one-photon process,  $\text{AsH}_3 + h\nu \rightarrow \text{AsH}_2 + \text{H}$ ,  $P(E_{c.m.})$ , indicates that  $\text{AsH}_2$  internal excitation accounts for  $\sim 64\%$  of the available energy [i.e.,  $h\nu - D_0(\text{H}_2\text{As-H})$ ]. Secondary  $\text{AsH}_2$  photodissociation also takes place. Analyses of superimposed structure atop the broad  $P(E_{c.m.})$  distribution suggest that  $\text{AsH}_2$  is formed with significant a-axis rotation as well as bending excitation. Comparison of the results obtained with  $\text{AsH}_3$  versus those of the lighter group-V hydrides ( $\text{NH}_3$ ,  $\text{PH}_3$ ) lends support to the proposed mechanisms. Of the group-V hydrides,  $\text{AsH}_3$  lies intermediate between the nonrelativistic and relativistic regimes, requiring high-level electronic structure theory.

The room temperature absorption spectrum of  $\text{SbH}_3$  has been recorded. The absorption spectrum is a broad continuum with no discernible structure; however, a long-wavelength tail is evident. The HRTOF technique has also been used to investigate the photodissociation dynamics of  $\text{SbH}_3$  following 193.3 nm photolysis. The overall shapes of the translational energy distributions were inconsistent, precluding confident analysis. In spite of this, it is apparent that  $\text{SbH}_2$  products are formed with substantial internal excitation and secondary photodissociation occurs. These general observations are consistent with the results obtained for  $\text{AsH}_3$ .

# Chapter 1

## Relativistic Effects in Chemistry

### 1.1 Introduction

It is a fact of life that special relativity influences profoundly a number of physical and chemical properties of molecules that contain heavy atoms. Physicists and chemists alike have examined relativistic effects on atomic and molecular length scales since the seminal work of Dirac<sup>1</sup> and others laid the foundations of relativistic quantum mechanics and, shortly thereafter, relativistic quantum field theory. The marriage of quantum mechanics and special relativity into a quantum field theory that begets relativistic quantum mechanics is one of the great scientific feats of the twentieth century. This theory had its inception in the late 1920's and it continues to be an active research area to this very day.

On the other hand, *relativistic quantum chemistry* only began as a serious endeavor starting around 1960, namely, when computers entered the scene, thereby making it possible to carry out calculations with sufficient accuracy that comparisons with experimental data became feasible. Since then many significant scientific and computational advances have been realized, the latter aided greatly by concomitant advances in computer technology. Nowadays relativistic quantum chemistry is discussed

thoroughly in texts and monographs,<sup>2-6</sup> and it is often introduced in graduate courses in physical chemistry, though usually at an elementary level.

As mentioned above, when heavy elements are present in a molecule, relativity can affect the molecule's physical and chemical properties in ways that can be quite pronounced. Witness for example the low melting point of mercury,<sup>2</sup> its interesting chemical bonds,<sup>3</sup> the glimmer of gold,<sup>4</sup> and the mysterious role that antiparticles play when electrons approach a highly charged nucleus (for example, at distances comparable to a Compton wavelength divided by  $2\pi$ ).<sup>5</sup> Changes in *physical properties* such as bond lengths, transition energies, and polarizations have been studied for some time,<sup>6</sup> and, not surprisingly, it is now widely appreciated that relativity also influences *chemical properties*. A well-known example is the so-called inert pair effect, which describes the reluctance of the sixth period elements (Hg – Rn) to use  $6s$  electrons in bonding.<sup>7</sup>

## 1.2. Relativistic Effects

### 1.2.1. Qualitative Effects

Perhaps the simplest illustration of a manifestation of relativity can be seen through consideration of the velocity, energy, and orbital radius of a hydrogen-like relativistic electron, *i.e.*, a single electron bound to a nuclear charge of  $+Ze$ , where it is understood that  $Z$  is substantially larger than unity. Some important properties of this system are listed below:

$$\langle v \rangle = \left( \frac{2\pi e^2}{nh} \right) Z \quad (1.01)$$

$$E = - \left( \frac{2\pi^2 e^4}{n^2 h^2} \right) mZ^2 \quad (1.02)$$

$$\langle r \rangle = \frac{Ze^2}{mv^2} \quad (1.03)$$

where  $n$  is the principle quantum number,  $e$  is the magnitude of the electron charge,  $v$  is the magnitude of the radial component of the velocity,  $h$  is Planck's constant,  $Z$  is the atomic number, and brackets  $\langle \dots \rangle$  denote expectation value. According to the theory of special relativity, the *apparent mass* of a moving object increases with its velocity. Classically this can be expressed as

$$m_r = \frac{m_0}{\sqrt{1 - \beta^2}}, \quad (1.04)$$

where  $m_0$  is the rest mass of the object,  $\beta \equiv v / c$ , and  $m_r$  denotes the so-called relativistic mass. It is not as if the mass of a particle truly increases, but the mass *appears to increase*, and equation (1.04) accounts for all phenomena that one is likely to encounter in relativistic quantum chemistry. High-level physics theory does not go along with this picture of the mass changing, but for our purposes this is an acceptable way of thinking. When dealing with light nuclei, which accounts for a great deal (indeed, the majority) of chemistry,  $v \ll c$  applies. In this case, relativistic effects can usually be neglected. However, as  $v$  approaches  $c$ , the ratio  $m_r / m_0$  can exceed unity by a large enough fraction to warrant its inclusion in the quantum mechanical theory. Substituting the expression for

the expectation value  $\langle v \rangle$  given by equation (1.01) into equation (1.04), *i.e.*,  $\beta \rightarrow \langle v \rangle / c$ , yields the quantum mechanical version of the ratio  $m_r / m_0$ .

In calculating  $m_r / m_0$  for the elements in the periodic table, one finds that there is less than a 1% change for all elements in the first three periods. This same treatment of the sixth period elements, however, shows a large increase in the  $m_r / m_0$  ratio, often exceeding 10%.<sup>8</sup> It stands to reason that these elements would experience large relativistic effects. Substitution of  $m_r$  for  $m$  in equations (1.02) and (1.03) reveals that as  $Z$  increases the electron energy increases and the orbital radius decreases relative to the  $m_r = m_0$  non-relativistic limit.<sup>8</sup>

The average radial speed for a  $1s$  electron in an atom is

$$\langle v \rangle = \alpha Z, \tag{1.05}$$

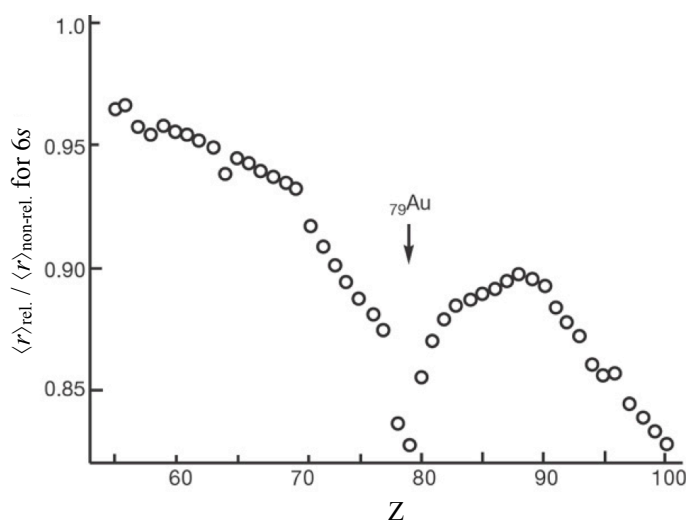
where  $\alpha$  is the fine-structure constant:  $\alpha = e^2 / \hbar c \approx 1/137$ . Clearly, relativistic effects depend strongly on  $Z$  in the sense that they manifest mainly in the heavier elements. For example, in the case of mercury, equation (1.05) yields an expectation value for the radial component of the velocity of the  $1s$  electron of  $0.58 c$ . This results in a reduction of the orbital radius by 23%.<sup>9</sup>

Paul Dirac's seminal 1928 paper<sup>1</sup> initiated the rapid subsequent development of relativistic quantum mechanics, not only by Dirac himself, but also through the efforts of a host of other scientists. For a time Dirac was unconvinced that relativity played a significant role in determining molecular structure due to the low velocities of valence electrons.<sup>4</sup> However, because of the fact that all  $s$ -orbitals are orthogonal to one another,

contraction of the core  $s$ -orbitals must affect the valence  $s$ -orbital electrons, as well as  $p$ -orbital electrons, albeit to a lesser degree. This contraction and stabilization of the  $s$ - and  $p$ -electrons leads to greater screening of the nuclear attraction of the  $d$ - and  $f$ -electrons, resulting in expansion of the  $d$ - and  $f$ -orbitals. This indirect relativistic effect of orbital radial expansion leads to energetic destabilization of the  $d$ - and  $f$ -orbitals,<sup>4</sup> as shown in figure 1.1. These and other (analogous) effects result in heavy-atom-containing molecules having properties such as ionization energies, bond strengths, and valence states that deviate in interesting ways from their lighter molecular counterparts.

**Figure 1.1.** Orbital contraction of gold's core  $s$ -orbitals results (through destabilization of its  $d$ -orbitals) in the low energy transitions originating from gold's  $d$ -orbitals that account for its "glitter." This figure (from google images) shows the resulting contraction of the  $6s$  orbital that destabilizes the  $d$ - and  $f$ -orbitals.

*Image from Google images.*



An atomic orbital can be described most efficiently by making use of a collection of quantum numbers for the electrons: the principle quantum number  $n$ , the orbital angular momentum quantum number  $l$  and its projection  $m_l$ , the spin angular momentum quantum number  $s$  and its projection  $m_s$ , and the total angular momentum (excluding nuclear spin) quantum number  $j$  and its projection  $m_j$ . Of course, not all of these can be used at the

same time, *i.e.*, in a basis, and conserved and approximately conserved quantities vary from case to case. In the relativistic treatment of the electron, particularly with heavy atoms, the operators for both the electron's orbital angular momentum  $\mathbf{l}$  and its spin angular momentum  $\mathbf{s}$  each fail to have good quantum numbers because of spin-orbit interaction.<sup>4</sup> However, their vector sum:  $\mathbf{j} = \mathbf{l} + \mathbf{s}$ , is conserved and has good quantum numbers  $j$  and  $m_j$ . Here and hereafter bold type is used to denote three-dimensional vector quantities.

In relatively light atoms (say  $Z < 30$ ),<sup>4</sup> individual electron spins interact with one another to form a total spin angular momentum  $\mathbf{S}$ . In the same vein, individual orbital angular momenta interact with one another to form a total orbital angular momentum  $\mathbf{L}$ . These momenta undergo Russell-Saunders ( $\mathbf{LS}$ ) coupling to form the total angular momentum:  $\mathbf{J} = \mathbf{L} + \mathbf{S}$ . Thus, energies associated with  $L \geq 1$  are split by spin-orbit interaction into a multiplet. For example, for  $S = \frac{1}{2}$  the  $J$  values are  $L \pm \frac{1}{2}$ . For  $L = 1$ , the states are denoted  ${}^2P_J = {}^2P_{1/2}$  and  ${}^2P_{3/2}$ . Sommerfeld was the first (in 1916) to report splitting due to spin-orbit interaction.<sup>10</sup> Atoms with larger nuclear charges often have spin-orbit interaction energies that are larger than either the spin-spin or the orbit-orbit interactions. In these cases, the orbital angular momentum of a given electron interacts with its spin angular momentum, giving an angular momentum  $\mathbf{j}$  for said electron. These individual momenta then interact to form the total angular momentum  $\mathbf{J}$  through the interaction known as  $\mathbf{j}-\mathbf{j}$  coupling.

### 1.2.2. Early Relativistic Quantum Mechanics

A brief overview of the history and reasoning that resulted ultimately in the Dirac equation is given here. A large number of texts treat this material in considerable depth.<sup>2-5</sup> To begin, consider the expression for the energy of a free particle in non-relativistic classical mechanics. This could not be simpler:

$$E = \frac{p^2}{2m}. \quad (1.06)$$

The following straightforward substitutions serve to introduce quantization:

$$E \rightarrow i\hbar \frac{\partial}{\partial t} \quad \mathbf{p} \rightarrow -i\hbar \nabla. \quad (1.07)$$

Thus, the Schrödinger equation for a free particle of mass  $m$  is

$$-\frac{\hbar^2}{2m} \nabla^2 \psi = i\hbar \frac{\partial \psi}{\partial t}. \quad (1.08)$$

For electrically charged particles it is necessary to include particle-field interactions. The electromagnetic potentials ( $\mathbf{A}$  and  $V$ ) are introduced straightaway into the above Schrödinger equation by invoking the principle of minimal coupling.<sup>11</sup> For example,  $\mathbf{p} \rightarrow \mathbf{p} - q\mathbf{A} / c$ , where  $\mathbf{A}$  is the vector potential and  $q$  is the particle's charge. Likewise, the scalar potential energy term  $qV$  is added to the Hamiltonian.<sup>11</sup>

Let us now turn to relativistic classical mechanics, in which case the relationship between a free particle's energy and momentum is given by

$$E^2 = p^2 c^2 + m^2 c^4. \quad (1.09)$$

To isolate the energy (as opposed to dealing with the square of the energy), it is tempting to take square roots of each side of equation (1.09). However, this introduces a mysterious minus sign:  $E = \pm(p^2c^2 + m^2c^4)^{1/2}$ . Specifically, the square root forces us to deal with what appears to be negative kinetic energy, and other egregious problems are present as well, *e.g.*, negative probability density. For example, making the same substitution as the one given in equation (1.07) yields a rather unusual expression for the relativistic analog of the Schrödinger equation:

$$i\hbar \frac{\partial \varphi}{\partial t} = \pm \sqrt{-\hbar^2 c^2 \nabla^2 + m^2 c^4} \varphi. \quad (1.10)$$

Note that  $\varphi$  is used here rather than  $\psi$  to distinguish solutions of this equation from those of the Schrödinger equation.

The operator on the right hand side of equation (1.10) is not easy to interpret, and in fact, to the best of my knowledge, it has never been tamed. The right hand side stymied Schrödinger to the point that he abandoned (temporarily) his attempt to develop a quantum mechanical theory based on equation (1.09). He settled instead for the non-relativistic version that we now refer to as the Schrödinger equation. An alternative strategy is to deal directly with an equation that uses the squared quantities. In this case, the substitutions given by equation (1.07) are introduced into the energy-momentum relation of classical relativity:  $E^2 = p^2c^2 + m^2c^4$ , to yield

$$\left( i\hbar \frac{\partial}{\partial t} \right)^2 \varphi = (-\hbar^2 c^2 \nabla^2 + m^2 c^4) \varphi. \quad (1.11)$$

Minor rearrangement yields the d'Alembertian form that is referred to as the Klein-Gordon equation:

$$\left( \partial_{ct}^2 - \nabla^2 + \left( \frac{mc}{\hbar} \right)^2 \right) \varphi = 0 \quad (1.12)$$

where the convenient notation  $\partial_{ct} \equiv \partial/\partial t$  ( $1/c$ ) has been used. This equation is Lorentz covariant, *i.e.*, it retains its form under Lorentz transformation. It can be expressed compactly by using relativistic four-vector notation, with implied summation over repeated indices (one up, one down).

$$\left( \partial^\nu \partial_\nu + \left( \frac{mc}{\hbar} \right)^2 \right) \varphi = 0, \quad (1.13)$$

and it has plane wave solutions of the form:

$$\varphi = \frac{1}{\sqrt{V}} \exp(i(\mathbf{p} \cdot \mathbf{r} - \omega t) / \hbar) \quad (1.14)$$

However, a negative energy solution as well as a positive energy solution is possible for each value of  $\mathbf{p}$ . This can be difficult to comprehend as the total energies for free particles can never be negative. Interpretation of this is discussed in the next section.

### 1.2.3. Dirac Equation

Dirac set out to derive a theory for relativistic spin- $1/2$  fermions by enlisting a first-order differential equation. To achieve an equation in which the time derivative appears

only in first order, as opposed to the Klein-Gordon equation, where the time derivative appears in second order, Dirac realized that the  $\nabla^2$  term in the kinetic energy operator must be abandoned. The relativistic equation must instead contain a term that is linear in  $\nabla$  and none that are quadratic in  $\nabla$ . The general form for such an equation for a free particle can be written:

$$i\partial_{ct}\psi = -\left(i\alpha^i\partial_i - \frac{mc}{\hbar}\beta\right)\psi. \quad (1.15)$$

It is necessary to determine  $\beta$  and  $\alpha^i$ . It is apparent that  $\beta$  and  $\alpha^i$  must be matrices (or at least matrices provide the most convenient representation) and the state vector  $\psi$  must be a spinor. For all practical purposes the lowest dimensional matrix representation of  $\beta$  and  $\alpha^i$  that satisfies the various requirements is  $4 \times 4$ . Dirac realized that in the absence of interaction with an electromagnetic field equation (1.15) must be compatible with the Klein-Gordon equation, *i.e.*, each of the spinor components must satisfy the Klein-Gordon equation. In fact, he used this as the basis of a strategy for deriving the forms of the  $\beta$  and  $\alpha^i$  matrices. It is interesting that this compatibility, in which each of the spinor components satisfies the Klein-Gordon equation in the absence of electromagnetic fields, ensures that the Dirac equation (like the Klein-Gordon equation) has both positive and negative energy solutions. However, unlike the Klein-Gordon case the Dirac probability density is positive real and spin is present. Nonetheless, each theory faces the challenge of interpreting the negative energy solutions that arise. This was remedied in the mid-1930's when it was realized that the Klein-Gordon and Dirac equations are, in fact,

equations in relativistic quantum field theory, not equations in quantum mechanics *per se*. The quanta of the Dirac field are fermions that obey the Dirac equation, but without suffering the burden of negative kinetic energies.<sup>5,12</sup>

To proceed, the operators in equation (1.15) are each squared, yielding an expression that contains second derivatives with respect to time and space. This expression contains the ingredients of the Klein-Gordon equation plus a number of unwanted terms. This is precisely what is needed. Specifically,  $\beta$  and  $\alpha^i$  are chosen such that the unwanted terms taken together sum to zero. Carrying out the above steps yields

$$\partial_{ct}^2 \psi = - \left( i\alpha^i \partial_i - \frac{mc}{\hbar} \beta \right)^2 \psi \quad (1.16)$$

$$= \left( \alpha^i \alpha^j \partial_i \partial_j + i \frac{mc}{\hbar} \alpha^i \beta \partial_i + i \frac{mc}{\hbar} \beta \alpha^i \partial_i - \beta^2 \left( \frac{mc}{\hbar} \right)^2 \right) \psi . \quad (1.17)$$

In going from equation (1.16) to (1.17), use has been made of the fact that the partial derivatives commute with the  $\beta$  and  $\alpha^i$  matrices, because the matrix elements in  $\beta$  and  $\alpha^i$  are numbers. Minor rearrangement highlights the relationship between equation (1.17) and the Klein-Gordon equation given by equation (1.12).

$$\underbrace{\left( \mathbf{1} \partial_{ct}^2 - (\alpha^i)^2 \partial_i^2 + \beta^2 \left( \frac{mc}{\hbar} \right)^2 \right)}_{\text{Klein-Gordon}} \underbrace{- i \frac{mc}{\hbar} \{ \alpha^i, \beta \} \partial_i - (\{ \alpha^1, \alpha^2 \} \partial_1 \partial_2 + \text{c.p.})}_{= 0} \psi = 0 \quad (1.18)$$

where  $\mathbf{1}$  is the unit matrix, squiggly brackets  $\{ \dots \}$  denote anti-commutation, and c.p. tells us to add the other two cyclic permutations of the indices.<sup>11</sup>

Equation (1.18) reveals the conditions that  $\beta$  and  $\alpha^i$  must satisfy. The first three terms must be retained because they comprise the Klein-Gordon equation, whereas the other terms must vanish. Setting  $\beta^2 = \mathbf{1}$  and  $(\alpha^i)^2 = \mathbf{1}$  recovers the Klein-Gordon equation for each component of the 4-spinor  $\psi$ . The properties of the  $\alpha^i$  and  $\beta$  matrices are summarized as follows:

$$(\alpha^i)^2 = \beta^2 = \mathbf{1} \tag{1.19}$$

$$\alpha^i \alpha^j + \alpha^j \alpha^i = \{\alpha^i, \alpha^j\} = 2\delta^{ij} \mathbf{1} \tag{1.20}$$

$$\alpha^i \beta + \beta \alpha^i = \{\alpha^i, \beta\} = 0. \tag{1.21}$$

The properties given by the above equations are sufficient to establish the lowest dimension of the matrices. When equation (1.21) is multiplied from either the left or right by  $\beta$ , it yields  $\alpha^i = -\beta \alpha^i \beta$ . Taking the trace of each side and using the trace's cyclic invariance yields  $\text{Tr } \alpha^i = -\text{Tr } \alpha^i$ . Thus, the trace vanishes.<sup>12</sup>

Equation (1.19) indicates that the eigenvalues of the matrices each have magnitude of unity, and the eigenvalues are real. They are each either +1 or -1. Because the trace is the sum of the eigenvalues, it follows that the number of +1's is equal to the number of -1's, and therefore the matrices are of even dimension. They cannot be  $2 \times 2$  because no combination of the Pauli matrices and the unit matrix (a complete basis in the space of two-dimensional complex matrices) exists that satisfies the anti-commutation relations.

This leaves  $4 \times 4$ , with the understanding that higher even dimensions are formally allowed, though to the best of my knowledge they are used infrequently if at all.

Let us now obtain a set of  $4 \times 4$   $\alpha^i$  and  $\beta$  matrices that obeys the rules given by equations (1.19) – (1.21). These matrices can be constructed by using the Pauli matrices,  $\sigma^i$ , and the unit matrix,  $\mathbf{1}$ . An example is

$$\alpha^i = \begin{pmatrix} 0 & \sigma^i \\ \sigma^i & 0 \end{pmatrix} \text{ and } \beta = \begin{pmatrix} \mathbf{1} & 0 \\ 0 & -\mathbf{1} \end{pmatrix}. \quad (1.22)$$

Each matrix element in the above matrices is itself a  $2 \times 2$  matrix. It is convenient (conventional) to replace the symbol  $\beta$  with  $\alpha^0$ . Writing the  $\alpha^i$  and  $\alpha^0$  matrices in explicit  $4 \times 4$  form yields:

$$\alpha^0 = \begin{pmatrix} 1 & 0 & 0 & 0 \\ 0 & 1 & 0 & 0 \\ 0 & 0 & -1 & 0 \\ 0 & 0 & 0 & -1 \end{pmatrix} \quad \alpha^1 = \begin{pmatrix} 0 & 0 & 0 & 1 \\ 0 & 0 & 1 & 0 \\ 0 & 1 & 0 & 0 \\ 1 & 0 & 0 & 0 \end{pmatrix}$$

$$\alpha^2 = \begin{pmatrix} 0 & 0 & 0 & -i \\ 0 & 0 & i & 0 \\ 0 & -i & 0 & 0 \\ i & 0 & 0 & 0 \end{pmatrix} \quad \alpha^3 = \begin{pmatrix} 0 & 0 & 1 & 0 \\ 0 & 0 & 0 & -1 \\ 1 & 0 & 0 & 0 \\ 0 & -1 & 0 & 0 \end{pmatrix} \quad (1.23)$$

An exact solution to the Dirac equation for the hydrogen atom yields eigenfunctions that are four-component spinors. Interpretation is that the two "large" spinor components of the positive energy solution correspond to the two possible spin projections of the

electron. The other two components (the small components) reflect the fact that something else is going on, *i.e.*, antiparticles are lurking. The small components vanish as  $v/c \rightarrow 0$ .<sup>11</sup>

The Dirac equation for an electron yields twice as many solutions as one might expect on the basis of non-relativistic quantum mechanics, and half of these solutions have negative energies.<sup>12</sup> The negative energies arise from what can best be called frustrated particle-antiparticle formation. They describe an electron, but one that arises when a positron-electron pair is created (say near a highly charged nucleus) on a short timescale. There is of course insufficient energy for the pair to survive, as this would require  $\sim 1$  MeV. In this case the positron annihilates the incident electron, leaving the electron that arose as part of the positron-electron pair. The spinor is for an electron. It is related to a positron spinor through an operation called charge conjugation. This stuff is beyond the scope of this thesis. The existence of antiparticles was included in Dirac's theory. Nonetheless, experimental discovery of the positron was not made until 1933 by Anderson.<sup>13</sup>

The Dirac equation given by equation (1.15) is easily converted to relativistic covariant form. To carry this out, go back to equation (1.15) and make the substitutions  $\partial_{ct} = \partial_0$  and  $\beta = \alpha^0$ :

$$\left( i\partial_0 + i\alpha^i \partial_i - \alpha^0 \frac{mc}{\hbar} \right) \psi = 0, \quad (1.24)$$

and multiply from the left by  $-\alpha^0$  to obtain:

$$\left( -i \left( \underbrace{\alpha^0}_{\gamma^0} \partial_0 + \underbrace{\alpha^i}_{\gamma^i} \partial_i \right) + \frac{mc}{\hbar} \right) \psi = 0 \Rightarrow \left( -i \gamma^\nu \partial_\nu + \frac{mc}{\hbar} \right) \psi = 0. \quad (1.25)$$

Standard form for field-free  
Dirac equation

where

$$\gamma^0 = \begin{pmatrix} 1 & 0 & 0 & 0 \\ 0 & 1 & 0 & 0 \\ 0 & 0 & -1 & 0 \\ 0 & 0 & 0 & -1 \end{pmatrix} \quad \gamma^1 = \begin{pmatrix} 0 & 0 & 0 & 1 \\ 0 & 0 & 1 & 0 \\ 0 & -1 & 0 & 0 \\ -1 & 0 & 0 & 0 \end{pmatrix}$$

$$\gamma^2 = \begin{pmatrix} 0 & 0 & 0 & -i \\ 0 & 0 & i & 0 \\ 0 & i & 0 & 0 \\ -i & 0 & 0 & 0 \end{pmatrix} \quad \gamma^3 = \begin{pmatrix} 0 & 0 & 1 & 0 \\ 0 & 0 & 0 & -1 \\ -1 & 0 & 0 & 0 \\ 0 & 1 & 0 & 0 \end{pmatrix}. \quad (1.26)$$

Again, application of the minimal coupling principle yields the gauge invariant Dirac equation, *i.e.*, including interaction of the particle with an electromagnetic field:<sup>11</sup>

$$\left( -i \gamma^\nu \left( \partial_\nu + i \frac{q}{c} A_\nu \right) + \frac{mc}{\hbar} \right) \psi = 0. \quad (1.27)$$

#### 1.2.4. Relativistic Many-Body Problem

Equation (1.27) ostensibly applies to a single electron. However, this electron is in the presence of an electromagnetic field, and in a molecule this field can be taken as arising from the other charged particles. There can be externally applied fields as well, but the important point is that the electron many-body problem can be approached by using equation (1.27), suitably adapted to as high a degree of accuracy as needed and/or deemed reasonable on the basis of computational limits, *i.e.*, time. The first step is converting the 4-spinor to a 2-spinor. This involves an expansion of the relativistic

Hamiltonian in powers of  $c^{-n}$ , and unless one is very ambitious, terms are retained to order  $c^{-2}$  but not higher. The math is tedious but straightforward. It is worked out in a number of texts.<sup>11</sup> The result is given in the equation below:

$$\begin{aligned}
 \hat{H} = & \underbrace{mc^2 + \frac{p^2}{2m} + qV}_{\text{obvious}} - \underbrace{\frac{q}{mc} \vec{A} \cdot \vec{p}}_{\text{useful for spectroscopic transitions}} + \underbrace{\frac{q^2}{2mc^2} A^2}_{\text{usually ignored}} - \underbrace{\frac{p^4}{8m^3c^2}}_{\text{energy-momentum correction}} \\
 & - \underbrace{\frac{q}{mc} \vec{s} \cdot \vec{B}}_{\text{Zeeman}} - \underbrace{\frac{q\hbar^2}{8m^2c^2} \nabla \cdot \vec{E}}_{\text{Darwin}} + \underbrace{\frac{q}{2m^2c^2} \frac{\partial_r V}{r} \vec{s} \cdot \vec{l}}_{\text{spin-orbit}}
 \end{aligned} \tag{1.28}$$

Referring to equation (1.28), the first three terms need no explanation. The  $\mathbf{A} \cdot \mathbf{p}$  term is often expressed as proportional to  $\boldsymbol{\mu} \cdot \mathbf{E}$ ; it is useful in spectroscopy. To the best of my knowledge, the  $A^2$  term does not enter relativistic quantum chemistry. The term  $p^4 / 8m^3c^2$  is obtained from the expansion:  $\pm(m^2c^4 + p^2c^2)^{1/2} = mc^2 + p^2 / 2m - p^4 / 8m^3c^2 \dots$  It is not a correction to the kinetic energy, but a term that arises through the relativistic energy-momentum relation. The  $\mathbf{s} \cdot \mathbf{B}$  term is the Zeeman contribution. The last term is the familiar spin-orbit interaction. Note that the Zeeman and spin-orbit terms have the correct  $g$  factor value of 2 for the electron. The next to last term—the Darwin term—is the hardest to interpret. Indeed, its interpretation is beyond the scope of this thesis. It arises through an interaction that, at first sight, seems harmless enough. It is the same interaction that yields the spin-orbit term, as indicated in figure 1.2.

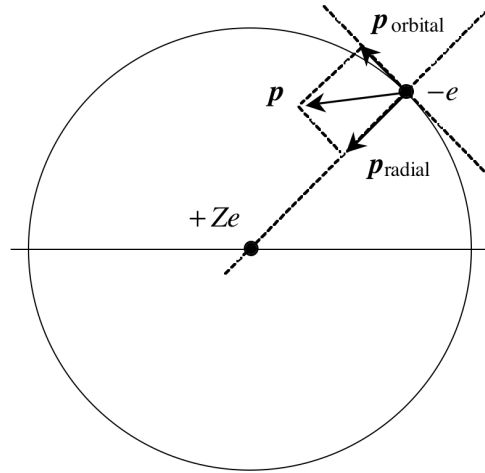


**Figure 1.2.** A charge of  $+Ze$  creates an electric field that accelerates the electron ( $-e$ ). The component of the momentum that is perpendicular to  $r$  contributes orbital angular momentum, resulting in spin-orbit interaction. Consequently, orbital and spin angular momentum are not separately conserved, whereas their sum:  $\mathbf{j} = \mathbf{l} + \mathbf{s}$ , is conserved.

Referring to figure 1.2, an electron that approaches the charge  $+Ze$  experiences a force. The field created by  $+Ze$  accelerates the electron radially. In general the particle's momentum can be separated into two components: one radial, the other perpendicular to the radial direction. The Darwin term deals with the radial component, whereas the spin-orbit term deals with the component that points in the angular direction. The Darwin term is distinct from the usual radial interaction, say of an  $s$  electron with a nucleus. This is why it is mysterious. Moreover, note that it is quite singular. The Coulomb potential varies inversely with distance, so  $\nabla \cdot \mathbf{E}$  varies as  $r^{-3}$ .

The extension of equation (1.28) falls under several headings (Breit-Pauli, and so on). An alternate approach is to subsume the so-called scalar terms (energy-momentum correction and Darwin) into an effective core potential. This is discussed further in Chapter 3.

### 1.3. Potential Energy Surfaces

A fundamental concept that is of paramount importance to all chemists, particularly physical chemists, is that of the potential energy surface (PES). A PES is obtained by solving the electronic Schrödinger equation at a set of nuclear coordinates, then at another (nearby) set of nuclear coordinates, and so on. This provides the electronic energy of a molecule as a function of the molecule's nuclear coordinates, *i.e.*, the PES. The fact that molecular geometry is expressed in terms of nuclear coordinates is a consequence of the Born-Oppenheimer (BO) approximation,<sup>14</sup> which is the centerpiece of all of molecular science.

In 1927 Max Born and his remarkably precocious graduate student J. Robert Oppenheimer<sup>14</sup> showed that, to a high degree of approximation, the nuclei in a molecule are stationary with respect to electron motion because of the large difference in time scales for nuclear versus electronic motion. Though such an approximation leads to inexact values for the energies, the errors introduced through the BO approximation (BOA) are generally no worse than the order of the mass ratio, which is usually  $< 10^{-4}$ . In addition to the fact that this approximation is generally quite accurate, it is also amenable to straightforward correction using perturbation theory.<sup>15</sup>

The Hamiltonian for the non-relativistic Schrödinger equation is

$$H = T_e + T_n + V_{ee} + V_{en} + V_{nn}, \quad (1.29)$$

where  $T_e$  and  $T_n$  are the electron and nuclear kinetic energies, and  $V_{ee}$ ,  $V_{en}$ , and  $V_{nn}$  are

Coulomb interaction potentials involving the electrons and the nuclei. These terms can be expressed as:

$$T_e = -\sum_i \frac{\hbar^2}{2m_e} \nabla_i^2 \quad (1.30)$$

$$T_n = -\sum_a \frac{\hbar^2}{2m_a} \nabla_a^2 \quad (1.31)$$

$$V_{ee} = \frac{1}{2} \sum_{i,j} \frac{1}{|\mathbf{r}_{ij}|} \quad (1.32)$$

$$V_{en} = -\sum_{i,a} \frac{Z_a}{|\mathbf{r}_i - \mathbf{R}_a|} \quad (1.33)$$

$$V_{nn} = \frac{1}{2} \sum_{a,b} \frac{Z_a Z_b}{|\mathbf{R}_{ab}|}, \quad (1.34)$$

where  $\mathbf{r}$  and  $\mathbf{R}$  represent the electronic and nuclear coordinates, respectively. In the above notation, it is understood that  $a = a_k$  with summation taken over  $k$ . These terms enable the Schrödinger equation to be solved for fixed nuclear coordinates by using

$$H_e \psi_i^e(\mathbf{r}; \mathbf{R}) = U_i(\mathbf{R}) \psi_i^e(\mathbf{r}; \mathbf{R}), \quad (1.35)$$

where  $H_e$  represents the electronic Hamiltonian and  $\psi_i^e(\mathbf{r}; \mathbf{R})$  is the  $i^{\text{th}}$  eigenfunction with eigenenergy,  $U_i(\mathbf{R})$ . The electronic Hamiltonian is given by

$$H_e = T_e + V_{ee} + V_{en} + V_{nn} \quad (1.36)$$

The term  $T^n$  is put aside in the BO approximation. The resulting electronic energy wave functions  $\psi_i^e(\mathbf{r};\mathbf{R})$  depend parametrically on  $\mathbf{R}$ . They correspond to specific electron configurations that yield the adiabatic PES,  $U_i(\mathbf{R})$ . In the BO approximation (BOA), the kinetic energies of the nuclei have no effect on the wave functions. This limits nuclear motion to a single PES and forbids transitions between adiabatic surfaces. Using a single adiabatic surface to describe the dynamics is great when it is applicable. However, it fails near a point of intersection (degeneracy), where non-adiabatic transitions can result in simultaneous propagation on more than one adiabatic surface. In other words, a system that does not experience an intersection can be described with good accuracy in the adiabatic regime.<sup>15</sup>

The non-separable terms in the molecular wave function are due to nuclear kinetic energy terms in the molecular Hamiltonian. These terms act to couple the potential energy surfaces. In the region of an avoided curve crossing or conical intersection these terms cannot be neglected and the BOA breaks down. The adiabatic representation requires the inclusion of the matrix elements neglected in the BOA:

$$\langle \psi_i | \frac{\partial}{\partial \mathbf{R}} | \psi_{i'} \rangle \quad \text{and} \quad \langle \psi_i | \frac{\partial^2}{\partial \mathbf{R}^2} | \psi_{i'} \rangle, \quad (1.37)$$

where  $\psi_i$  are the electronic wave functions calculated for fixed nuclear coordinates  $\mathbf{R}$ .

The adiabatic surfaces are obtained by finding solutions to the Schrödinger equation using the full electronic Hamiltonian, including spin-orbit coupling terms.<sup>16</sup> The adiabatic surfaces  $\psi_1$  and  $\psi_2$  indicated in figure 1.3 do not cross because they have a non zero spin-orbit coupling

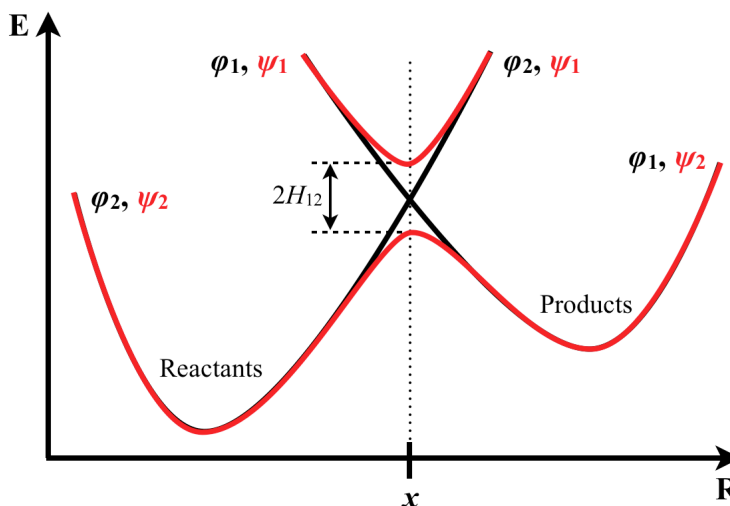


**Figure 1.3.** This diagram indicates the relationship between adiabats ( $\psi$ ) to diabats ( $\phi$ ). For reaction coordinate  $R \ll x$  (*i.e.* outside the coupling region),  $\psi_1 = \phi_1$  and  $\psi_2 = \phi_2$ , and for  $R \gg x$  (*i.e.* outside the coupling region),  $\psi_1 = \phi_2$  and  $\psi_2 = \phi_1$ . The diabats  $\phi_1$  and  $\phi_2$  are coupled via  $H_{12}$ .<sup>16</sup>

matrix element,  $H_{12} = \langle \psi_1 | H_{SO} | \psi_2 \rangle$ . The eigenfunctions are mixtures of different spin states, and there is a well-defined maximum on the lower surface. In cases when the mixing is modest the system will undergo transitions from one surface to another. These can be described in terms of diabatic surfaces  $\phi_1$  and  $\phi_2$ , as sudden changes in spin state, or as hops between the adiabatic surfaces  $\psi_1$  and  $\psi_2$ .

The Schrödinger equation is typically solved with the nuclear coordinates fixed, and then the equations of motion for the nuclear degrees of freedom are solved. This approach breaks down when two potential energy surfaces of the same symmetry are close to each other. In this case, the decoupling of electronic and nuclear motion is no longer justified. As a result, the simultaneous motions along multiple PES's and the coupling elements

between them must be taken into account. This is generally no small feat, as the nuclear kinetic energy coupling matrix elements indicated in equation (1.37) become complicated when there are many nuclear degrees of freedom. In this case it is usually useful to perform a transformation to a diabatic representation in which the non-adiabatic coupling matrix elements are made as small as possible. This linear (usually unitary) transformation serves to minimize off-diagonal nuclear kinetic energy matrix elements, thus making the equations easier to solve. The adiabatic potential energy surfaces are combined to produce a set of diabatic potentials, by using a transformation of the form:<sup>11</sup>

$$\begin{pmatrix} \varphi_1 \\ \varphi_2 \end{pmatrix} = \begin{pmatrix} \cos \theta & -\sin \theta \\ \sin \theta & \cos \theta \end{pmatrix} \begin{pmatrix} \psi_1 \\ \psi_2 \end{pmatrix}, \quad (1.38)$$

where the  $\psi_i$  are the adiabatic wave functions, the  $\varphi_i$  are the derived diabatic electronic wave functions and  $\theta$  is the nuclear coordinate mixing angle parameter. Assuming that all of the wave functions are real, the above orthogonal transformation can be used to relate real bases. By setting the condition in the new basis that the derivative coupling is equal to zero for all  $\theta$ :

$$\langle \varphi_2 | \nabla | \varphi_1 \rangle, \quad (1.39)$$

the diabatic basis can be established. This gradient is with respect to nuclear degrees of freedom, whereas the integration is carried over electronic degrees of freedom. As a result of this transformation the electronic Hamiltonian operator is no longer diagonal.<sup>16</sup> However, in general the coupling due to these non-diagonal elements is more easily dealt

with than the kinetic energy coupling terms. In the diabatic representation the coupling is due to the scalar electronic energy:

$$i\hbar \frac{\partial}{\partial t} \begin{pmatrix} \varphi_1 \\ \varphi_2 \end{pmatrix} = \left\{ \begin{pmatrix} T_{11} & 0 \\ 0 & T_{22} \end{pmatrix} + \begin{pmatrix} V_{11} & V_{12} \\ V_{21} & V_{22} \end{pmatrix} \right\} \begin{pmatrix} \varphi_1 \\ \varphi_2 \end{pmatrix}. \quad (1.40)$$

An example of a conical intersection is the degeneracy point where the  $\tilde{X}^1A_1'$  and  $\tilde{A}^1A_2''$  potentials of  $\text{NH}_3$  meet, as seen in Figure 1.4. These states are shown as a function of two molecular coordinates, the N-H distance,  $R$ , and the out of plane angle,  $\theta$ , with all

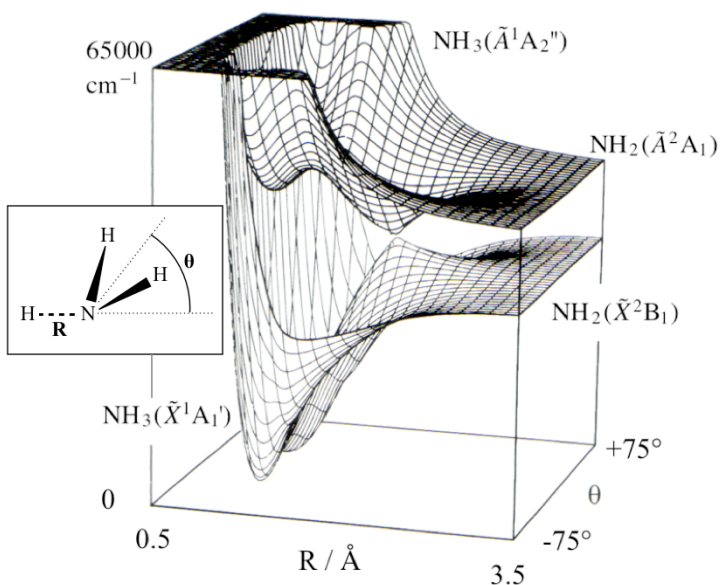


**Figure 1.4.** Conical intersection of  $\text{NH}_3(\tilde{A})$  corresponding diabatically to  $\text{NH}_2(\tilde{X})$  state along  $\theta = 0$ .<sup>11</sup>

other nuclear degrees of freedom held fixed in space.<sup>11</sup> This degeneracy point is a specific type of intersection known as a conical intersection. This intersection is intriguing due in part to the symmetry variation around the point of degeneracy. Both the upper and lower adiabats have different symmetries on either side of the intersection. This difference of symmetries between the diabats dictates that the off-diagonal matrix elements are zero, which facilitates curve crossing along the  $\theta = 0$  line where the adiabatic and diabatic curves are the same. These potentials of  $\text{NH}_3$  and the related photodissociation dynamics are discussed in greater detail in Chapter 3.

## 1.4. Photodissociation Dynamics

Photodissociation is the process by which a bound molecular system is fragmented as a consequence of the absorption of one or more photons. This might occur when the absorbed electromagnetic energy is converted to internal energy of the molecule and this internal energy exceeds a bond energy. Experiments in photodissociation dynamics often provide state-to-state information of the molecular dynamics that occur and can further our understanding of chemical reactions beyond the level of chemical kinetics. These experiments can also help elucidate such processes as molecular energy transfer, chemical bond formation and dissolution, and transitions that take place among molecular states.<sup>17-19</sup> Of particular interest in the present context is determining how the total available energy is distributed among the center-of-mass translational and various fragment internal degrees of freedom.

Photodissociation can, roughly speaking, be of two kinds: direct and indirect. The determination of dissociation type is dependent on the topography of the PES's of the molecular system in question. When a photon excites a molecule from the ground electronic state to an excited state that is repulsive along a reaction coordinate, the excited complex will dissociate in a process referred to as direct dissociation.<sup>20</sup> In

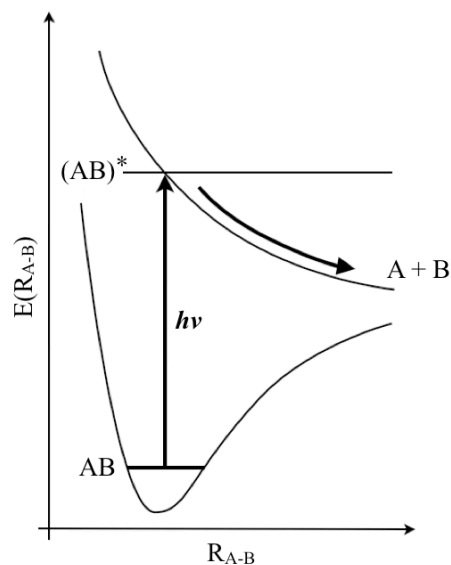


**Figure 1.5.** Schematic illustration of UV photodissociation from a purely repulsive excited state.<sup>21</sup>

this case (figure 1.5), the photon energy in excess of the bond energy is partitioned among the translational and internal energies of the photodissociation fragments. Figure 1.5 illustrates the simplest form of direct dissociation: the photodissociation fragments repel each other, resulting in rapid dissociation.

On the other hand, if the upper electronic state is not purely repulsive, direct dissociation is prohibited and the wave packet can be trapped on the upper state for some period of time. If the photon excites the molecule to an electronic state that is not repulsive, and consequently undergoes transition to another state that is repulsive,

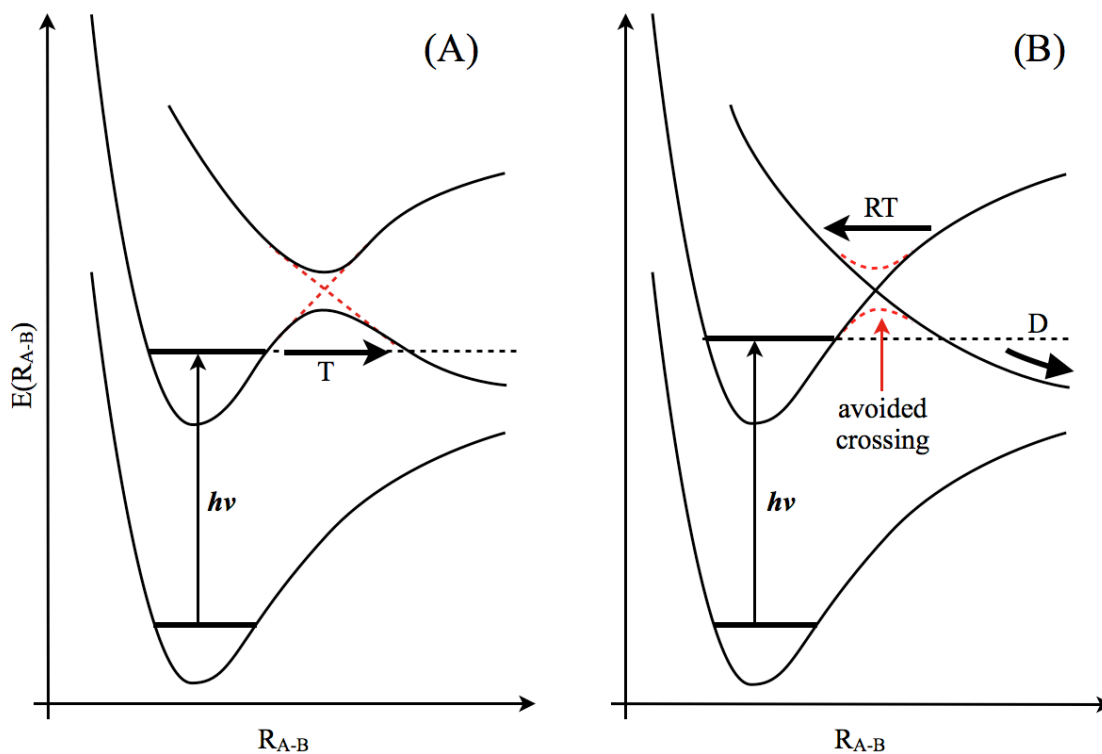


**Figure 1.6.** Schematic illustration of UV photodissociation via (A) vibrational and (B) electronic predissociation. In (A) a quasi-bound resonance is excited which allows decay via tunneling (T) whereas in (B) the system undergoes a radiationless transition (RT) to the repulsive state and decays.<sup>21</sup>

dissociation can occur with a rate dependent upon the coupling between the two states involved. This so-called electronic predissociation is illustrated in figure 1.6(B).<sup>20</sup>

Another potential obstruction to dissociation may be an avoided crossing with a higher electronic state, in which case the photon is said to excite a quasi-stable resonance state which delays immediate dissociation. This case can be seen in figure 1.6(A). Regardless of type, the dissociation is dependent on the initial quantum state of the parent molecule and the energy of the absorbed photon. Details of the dissociation dynamics can be inferred from the rotational-vibrational distribution of the populated states. The dependence of the fragment coordinate primarily dictates the vibrational state distribution, while orientation angle tends to determine the rotational state distributions. The electronic state populations are determined by the degree of nonadiabatic coupling between the pertinent electronic states. In general, the number of vibrational modes populated tends to be limited by energetic constraints, but many more rotational modes can frequently be populated making specific assignment challenging.

## 1.5. Chapter 1 References

1. Dirac, P.A.M. *Proceedings of the Royal Society A: Mathematical, Physical and Engineering Sciences*. **1928**, 177, 778.
2. Pitzer, K. S. *Acc. Chem. Res.* **1979**, 12, 271.
3. Christiansen, P. A.; Ermler, W. C.; Pitzer, K. S. *Annu. Rev. Phys. Chem.* **1985**, 36, 407.
4. Pyykkö, P.; Desclaux, J.-P. *Acc. Chem. Res.* **1979**, 12, 276.
5. Balasubramanian, K. *Relativistic Effects in Chemistry, Part A*; John Wiley & Sons, Inc: New York, 1997.
6. Balasubramanian, K. *Relativistic Effects in Chemistry, Part B*; John Wiley & Sons, Inc.: New York, 1997.
7. Rich, R. *Periodic Correlations*; W. A. Benjamin: New York, 1965.
8. Barysz, M; Ishikawa, Y. *Relativistic Methods for Chemists*. Springer Science +BusinessMedia: New York, 2010
9. Thayer, John S. *J. Chem. Educ.* **2005**, 11, 1721
10. Christiansen, P. A.; Ermler, W. C.; Pitzer, K. S. *Annu. Rev. Phys. Chem.* **1985**, 36, 407.
11. Wittig, C.F. *unpublished manuscript*
12. Greinier, W. *Relativistic Quantum Mechanics*; Springer: New York, 1997.
13. Anderson, C.D. *Physical Review*. **1933**, 43, 491.
14. Born, M; Oppenheimer, J.R. *Annalen der Physik*. **1927**, 389, 457.
15. Miller, W. H. *Dynamics of Molecular Collisions, Part B*; Plenum Press: New York, 1976.
16. Harvey, Jeremy N. *Phys. Chem. Chem. Phys.* **2006**, 9, 331.

17. Ashfold, M. N. R.; Baggott, J. E. *Molecular Photodissociation Dynamics*; Royal Society of Chemistry: Piccadilly, 1987.
18. Butler, L. J.; Neumark, D. M. *J. Phys. Chem.* **1996**, *100*, 12801.
19. Simmons, J. P. *J. Phys. Chem.* **1984**, *88*, 1287.
20. Shinke, R. *Photodissociation Dynamics*; Cambridge University Press: Cambridge, 1993.
21. Shinke, R. *Photodissociation Dynamics*. *John Wiley & Sons* [online]. CPA11. <http://www.wiley.com/legacy/wileychi/ecc/samples/sample03.pdf>

# Chapter 2

## Experimental Methods

### 2.1 Introduction

This chapter discusses in detail the methodology used in the Wittig laboratory to study molecular photodissociation dynamics. Section 2.2 illustrates the overall technique of high- $n$  Rydberg hydrogen time-of-flight (HRTOF) spectroscopy while section 2.3 delves deeper into the individual components of this sophisticated experiment. Further subsections address the finer points of the experimental parameters and the many degrees of freedom required to perform these experiments.

### 2.2 Time-of-flight Spectroscopy

#### 2.2.1 Hydrogen ion Time-of-flight Spectroscopy

The time-of-flight (TOF) principle has been used in mass spectrometry since the late 1940's, however the field continues to develop as new technologies continue to expand the potential of the basic technique. The advent of cold molecular beam expansions of liquids and gasses into a vacuum has allowed the time-of-flight technique to be employed for the investigation of molecular photodissociation dynamics by studying the translational energy of hydrogen molecular fragments induced by laser photodissociation.<sup>1</sup> This early variant of the technique relied upon studying hydrogen

containing molecules and ionizing the nascent hydrogen atoms prior to escaping the interaction region for detection of the ion. While this technique provided a greater energy resolution relative to electron bombardment of neutral hydrogen photofragments, it still suffers from Coulombic repulsion of the protons created in a relatively small space and short time.<sup>2</sup> This smearing of the velocity and angular distributions of the hydrogen fragments led to the refinement of the technique to monitor the kinetic energy distributions of the neutral hydrogen atom via a high- $n$  Rydberg state.

### 2.2.2 High- $n$ Rydberg Time-of-flight Spectroscopy

Significant improvement over hydrogen ion TOF spectroscopy was introduced and developed by the group of Karl Welge<sup>1</sup>. This innovation is based on the generation of a neutral hydrogen fragment that has been promoted from the ground state to a high- $n$  Rydberg state via two-photon resonant excitation,

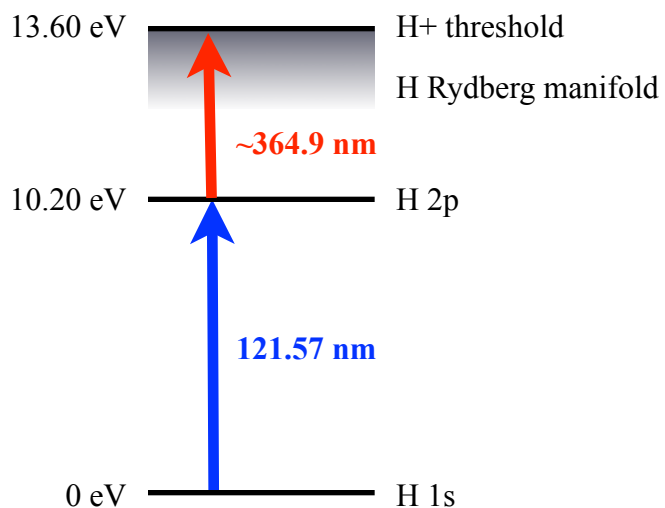


**Figure 2.1.** Energy diagram showing 2-photon 2-color excitation scheme used to promote neutral hydrogen atoms to a high- $n$  following photodissociation.

as indicated in figure 2.1. This is achieved by using two separately tunable laser pulses that intersect the interaction region after a small time delay relative to the photolysis

pulse. The first laser frequency is tuned to the hydrogen Lyman- $\alpha$  transition at 121.57 nm. This photon promotes the electron from the  $n = 1$  to  $n = 2$  state.

The second laser pulse is tuned to a frequency ( $\sim 364.9$  nm) that promotes the electron to a Rydberg state of high principal quantum number (typically  $n \approx 40-50$ ).<sup>3</sup> These states lie just below (a few wavenumbers) the ionization threshold of 13.579 eV. The ensuing Rydberg hydrogen atom thus prepared has an emission lifetime of roughly tens of microseconds.<sup>3</sup> The fact that the atom is neutral ensures that its trajectory is free from the field interactions that complicate hydrogen ion TOF spectroscopy. importantly, this lifetime can be further prolonged by the presence of a weak DC field during the preparation of the Rydberg atom, which diminishes radiative decay rates dramatically, enabling even quite slow H atoms (*e.g.*, with flight times of hundreds of  $\mu\text{s}$ ) to be detected. This alleviates the space charge effects that arise in  $\text{H}^+$  TOF spectroscopy, and consequently a greater kinetic energy resolution is realized: typical  $\delta E / E$  values are  $\sim 0.5\%$ .<sup>4</sup>

As the ionization potential of Rydberg atoms scale with  $n^{-2}$ , the nascent hydrogen Rydberg atom can be readily ionized with a weak DC electric potential applied when passing through a mesh screen pair immediately prior to detection with multi-channel plate detectors (MCP's).<sup>3</sup>

## 2.3 Experimental Setup and Details

### 2.3.1 Vacuum Chamber

A schematic drawing of the vacuum chambers, pumps, and associated parts used in all of the experiments reported herein is presented in figure 2.2. Though this arrangement has been described in detail elsewhere,<sup>3,5</sup> a number of aspects that are particularly germane to the present studies are covered here. The heart of the experimental apparatus is a variably pumped stainless steel high vacuum chamber constructed and retrofitted in a piecemeal fashion over the past two decades. The chamber is divided into three regions, each pumped by a dual-phase pumping system. The detector region is separated by an “8 inch” pneumatically actuated gate valve allowing it to be isolated when not in use for detection. This section is maintained at a pressure of  $\sim 5 \times 10^{-9}$  torr (when closed) by a turbomolecular pump (Pfeiffer TPU 240) backed by a mechanical pump (Edwards E28), with an overall rate of 230 L/s. This ensures the sensitive MCP detectors are maintained in a “clean” state when not in use to prolong lifetime.

The sample is introduced to the source region of the chamber via a pulsed molecular beam nozzle (General Valve, 1.0 mm orifice) operated by a pulse driver (Parker Iota One) with a repetition rate of 10 Hz. The orifice of the molecular beam nozzle is 1.0 mm and lies 1.5 cm upstream from a skimmer cone with a 1.0 mm orifice size. This skimmer cone provides separation of the source region from the main region of the chamber and serves to collimate the molecular beam. The source region is pumped by a “10 inch” diffusion pump (Varian VHS-10) backed by a mechanical pump (Varian

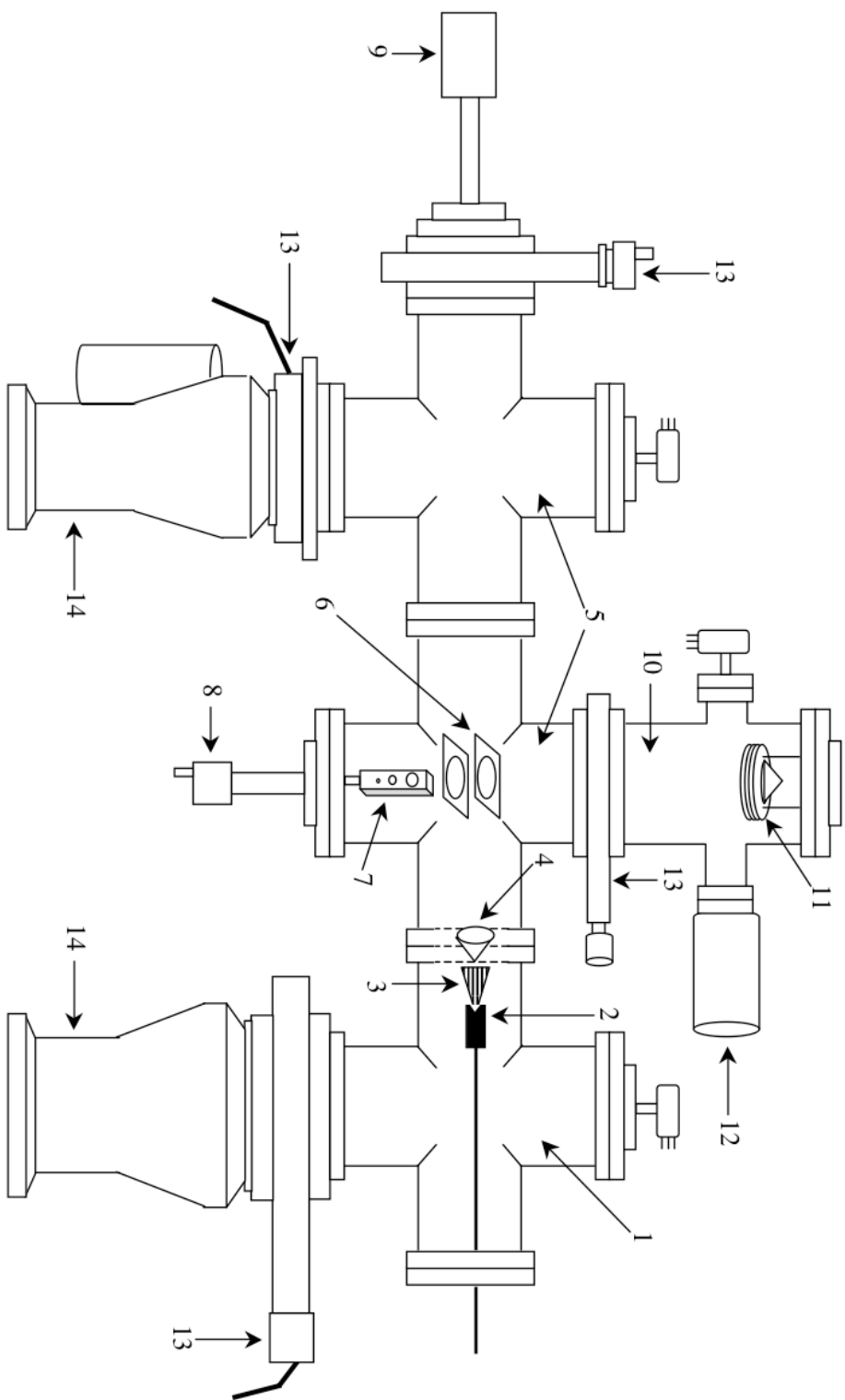


**Figure 2.2.** Schematic of the HRTOF chamber and apparatus with components: 1) source chamber, 2) pulsed nozzle, 3) molecular beam, 4) skimmer cone, 5) main chamber, 6) interaction region electrodes, 7) alignment bar, 8) linear motion positioner, 9) residual gas analyzer, 10) TOF tube, 11) MCP detector assembly, 12) turbomolecular pump, 13) gate valves, 14) diffusion pumps

SD700), and maintains a pressure of  $\sim 7 \times 10^{-7}$  torr (when the molecular beam is off).

The collimated molecular beam enters the main chamber through the skimmer cone and passes through the interaction region where it is intersected by three temporally separated (but spatially overlapped) laser beams. The main chamber is pumped by a cryo-cooled (Edwards 160) 10 inch diffusion pump (Edwards MK2 DiffStack™) backed by a mechanical pump (Varian SD700). This chamber maintains an operational pressure of  $\sim 5 \times 10^{-7}$  torr.

The interaction region consists of two parallel plates stacked horizontally above and below the intersection region which act as electrodes for ion repulsion (when necessary) and for the application of a weak dc potential ( $\sim 20$  V/cm). There is also an alignment bar that can be raised to assist with the alignment of the three independent laser beams onto the molecular beam. Further downstream from the interaction region connected to the main chamber via a “10 inch” gate valve is a quadrupole mass spectrometer (Stanford Research Systems Rare Gas Analyzer 300) which aids in identifying the composition of the molecular beam and in system troubleshooting. All vacuum pressure measurements are supplied by ionization vacuum gauges (see figure 2.2).

The main flight path is the vertical distance from the interaction region to the face of the MCP detector and can be changed with the addition of flange extensions between the main and detector chambers. The flight path used for subsequent discussions is  $\sim 43.5$  cm and is determined experimentally using the photodissociation of HCl as a benchmark, since the dissociation values and spin-orbit split values are well known for this system.<sup>3</sup>

### 2.3.2 Laser Systems

The interaction region is comprised of the confluence of three laser beams, each entering the chamber separately, and the molecular beam. Figure 2.3 indicates

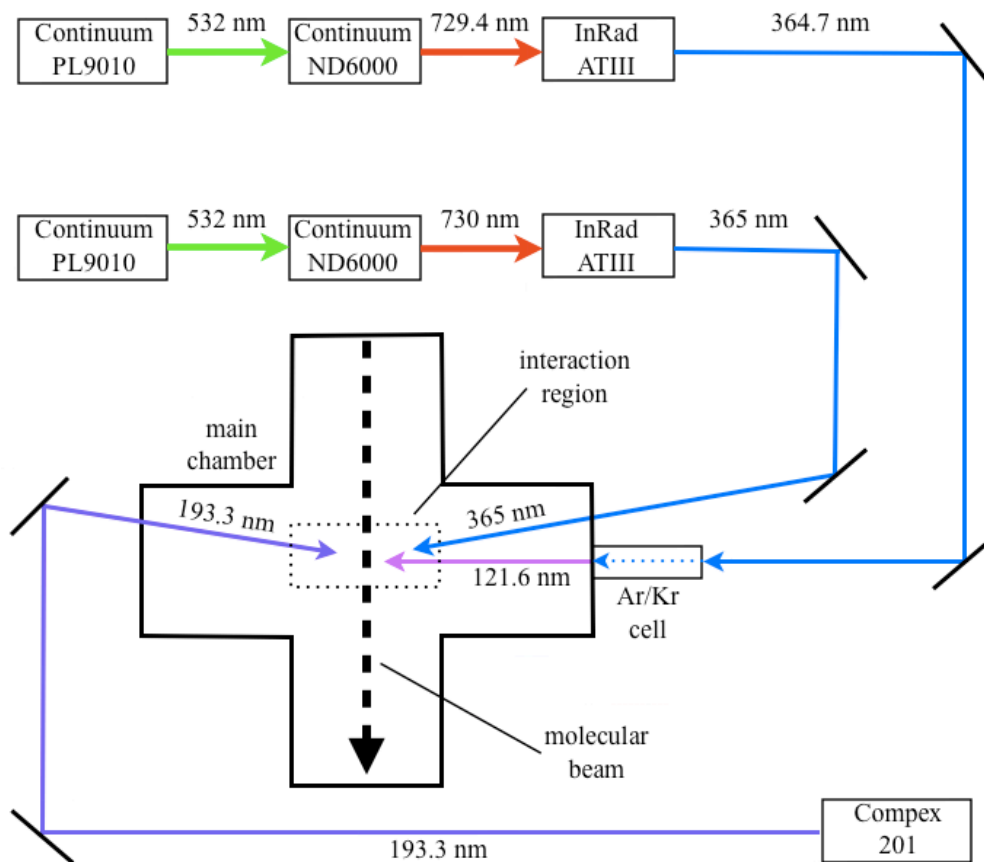


**Figure 2.3.** Schematic of the laser systems and beam paths as seen from above the vacuum chamber.

schematically how these four beams come together. The photodissociation beam is generated by the output of an excimer laser (LamdaPhysik Compex 201) capable of producing a variety of fixed frequencies determined by the internal gas mixture. The photolysis wavelength of 193.3 nm was provided by an ArF mixture with a repetition rate

of 10 Hz and focused into the interaction region using a 100 cm focal length synthetic quartz converging lens. This beam counter-propagates the other two laser beams in the interaction region with an offset angle of  $6^\circ$ .

Subsequent to photodissociation the nascent hydrogen atoms are excited with 2-color 2-photon absorption to the previously discussed Rydberg state. Neutral ground state hydrogen atoms are excited via the  $2p \leftarrow 1s$  (Lyman- $\alpha$ ) transition with 121.57 nm radiation. This radiation is created by the second harmonic (532 nm) of a Nd:YAG (Continuum Powerlite 8010) pumped dye laser (Continuum ND6000, LDS 750 laser dye) to produce 729.42 nm, which is subsequently frequency doubled in a KDP-C crystal autotracker (Inrad ATIII) to produce 364.71 nm. This near-UV radiation is focused by an 80 mm  $\text{MgF}_2$  lens into a 10-cm cell containing an Ar/Kr mixture thus producing the VUV radiation by non-resonant frequency tripling.<sup>6</sup>

The second laser beam used in the tagging process is radiation of  $\sim 365$  nm created by the identical process described above without the tripling process. This leaves the nascent hydrogen atoms prepared in a Rydberg state of  $n \sim 50$ . A typical photolysis/probe delay for these experiments is  $\sim 20 - 40$  ns.<sup>5</sup>

### **2.3.3 Electronic Control and Detection Systems**

As the Rydberg hydrogen atoms approach the detectors they are intercepted by a perpendicular fine wire mesh which has a small dc bias potential applied to facilitate field ionization. The nascent protons then strike the face of the MCP assembly (shown in

figure 2.2) and are detected with near unit efficiency.<sup>5,7</sup> The detectors (Photonis 30434) are two parallel stacked chevron-style 50 mm multi-channel plates operated at a potential of ~2 kV and paired with a conical anode. The electron signal produced is amplified by a pulsed fast-gated  $10 \times$  amplifier (Avtech AV-141C) and collected using a digital oscilloscope (Tektronix TDS540, 500 MHz).

All of the lasers and the molecular beam are pulsed at a rep. rate of 10 Hz, and the triggering and timing of all are controlled by a series of triggering boxes (Stanford Research Systems DG535). The individual pulse timing of all three laser beams is monitored in real time at the input windows by UV-sensitive fast (1 ns rise time) photodiodes (ThorLabs DET 210).

### **2.3.4 System Alignment**

The convergence of three laser beams with the pulsed molecular beam in both space and time is a non-trivial experimental process, which is facilitated by a custom machined alignment jig that can be raised with a positioning micrometer. This alignment jig has multiple orthogonal holes to allow propagation of both the molecular beam and laser beams (see figure 2.2). The position of the molecular beam is determined by using a HeNe alignment laser representing the molecular beam path, aligned through the nozzle, faceplate and skimmer through the interaction region. With this point benchmarked, the photolysis (193 nm) and Rydberg (~365 nm) beams can be aligned through the corresponding perpendicular hole. This provides a close starting point for spatial overlap

of these two laser beams with the molecular beam. Unfortunately, alignment of the non-visible Lyman- $\alpha$  beam is confounded by divergence of the 121.6 nm light and untripled 364.8 nm light when passing through an optic with imperfect alignment.

The position of the Lyman- $\alpha$  radiation must still be determined with respect to the molecular beam. This is accomplished by using an ion signal generated from its interaction with an expanded beam of nitric oxide (NO, Matheson 99.95%) into the main chamber producing detectable NO<sup>+</sup> cations. The position of the Lyman- $\alpha$  beam can be adjusted in the horizontal plane to maximize the spatial overlap by monitoring the detected ion signal. Although this procedure provides a starting point for system alignment, it is no magic bullet. Complications and difficulties of this procedure and others will be discussed in detail in chapter 4.

## 2.4 Data Collection and Processing

Raw data collection provides a TOF distribution which is converted to a kinetic energy distribution of the hydrogen photofragment(s). The parent hydride molecule prepared in the molecular beam can be represented by AB-H and undergoes the following general photolysis reaction:



where H is the detected hydrogen fragment and AB is the remaining photofragment. Knowing the length of the flight path and using the appropriate time-to-energy Jacobian

shown in equation (2.02),<sup>5</sup> each point in the TOF spectrum can be converted to a total kinetic energy spectrum with equation (2.03),

$$P(E_{c.m.}) \propto t^3 f(t(E_{c.m.})) \quad (2.02)$$

$$E_{\text{TOT}}^{\text{kin}} = E_{\text{H}}^{\text{kin}} + E_{\text{AB}}^{\text{kin}} = \frac{1}{2} m_{\text{H}} v_{\text{H}}^2 + \frac{1}{2} m_{\text{AB}} v_{\text{AB}}^2 \quad (2.03)$$

where  $m_{\text{H}}$  and  $v_{\text{H}}$  are mass and velocity of the hydrogen atom and  $m_{\text{AB}}$  and  $v_{\text{AB}}$  are the mass and velocity of the AB photofragment.

This relationship is true for the laboratory frame but must be converted to the center-of-mass (c.m.) frame of reference for a detector and flight path perpendicular to the molecular beam. These corrections can be made by using the following relationships:

$$m_{\text{H}} v_{\text{H}}^{\text{c.m.}} = m_{\text{AB}} v_{\text{AB}}^{\text{c.m.}} \quad (2.04)$$

$$v_{\text{H}} = \sqrt{(v_{\text{H}}^{\text{c.m.}})^2 + (v_{\text{MB}})^2} \quad (2.05)$$

where  $v_{\text{mb}}$  is the velocity of the molecular beam and equation (2.04) is from conservation of momentum in the c.m. system. The final relationship for the center-of-mass translational energy spectrum then becomes:

$$E_{\text{TOT}}^{\text{c.m.}} = E_{\text{H}}^{\text{c.m.}} + E_{\text{AB}}^{\text{c.m.}} = \frac{m_{\text{H}}}{2} \left( 1 + \frac{m_{\text{H}}}{m_{\text{AB}}} \right) \left( \frac{d_{\text{TOF}}}{t_{\text{H}}} \right) \quad (2.06)$$

Conservation of energy allows for the determination of the internal energy distribution of the remaining photofragment, AB by the following relationship:

$$E_{\text{avail}} = h\nu + E_{\text{int}}(\text{ABH}) - D_0(\text{AB} - \text{H}) = E_{\text{int}}(\text{AB}) + E_{\text{trans}}^{\text{c.m.}} \quad (2.07)$$

where  $h\nu$  is the photon energy,  $D_0$  is the AB–H bond dissociation energy, and  $E_{\text{int}}$  is the internal energy. It can be noted that the internal energy of the hydrogen atom is zero, and the internal energy of the parent molecule AB–H is negligible due to the use of a cold molecular beam.<sup>8</sup> This reduces equation (2.07) to the following expression:

$$h\nu - D_0(\text{AB} - \text{H}) = E_{\text{int}}(\text{AB}) + E_{\text{trans}}^{c.m.} \quad (2.08)$$

thus yielding the expression for the internal energy distribution of the photofragment AB.

## 2.5 Chapter 2 References

1. Schnieder, L.; Meier, W.; Welge, K. H.; Ashfold, M. N. R.; Western C. M. *J. Chem. Phys.* **1990**, *92*, 7027.
2. Ashfold, M. N. R.; Lambert, I. R.; Mordaunt, D. H.; Morley, G. P.; Western, C. M. *J. Phys. Chem.* **1992**, *96*, 2938.
3. Gallagher, T. F. *Rydberg Atoms*; Cambridge Univ. Press: Cambridge, 1994. 4142
4. Zhang, J.; Dulligan, M.; Wittig, C. *J. Phys. Chem.* **1997**, *107*, 1403.
5. Zhang, J.; Dulligan, M.; Wittig, C. *J. Phys. Chem.* **1995**, *99*, 7446.
6. Hilbig, R.; Wallenstein, R. *IEEE J. Quant. Electron.* **1981**, *8*, 1556.
7. Wiza, J. L. *Nuclear Instruments and Methods*, **1979**, *162*, 587.
8. Scoles, G. *Atomic and Molecular Beam Methods*; Oxford University Press: New York, 1988, Vol. 1.
9. Lee, Y.T.; McDonald, J. D.; Lebreton, P. R.; Herschbach, D. R. *Rev. Sci. Instrum.* **1969**, *40*, 1402.
10. Xie, X.; Schnieder, L.; Wallmeier, H.; Boettner, R.; Welge, K. H.; Ashfold, M. N. R. *J. Chem. Phys.* **1990**, *92*, 1608.
11. Biesner, J.; Schnieder, L.; Schmeer, J.; Ahlers, G.; Xie, X.; Welge, K. H.; Ashfold, M. N. R.; Dixon, R. N. *J. Chem. Phys.* **1988**, *88*, 3607.
12. Biesner, J.; Schnieder, L.; Ahlers, G.; Xie, X.; Welge, K. H.; Ashfold, M. N. R.; Dixon, R. N. *J. Chem. Phys.* **1989**, *91*, 2901.
13. Schnieder, L.; Meier, W.; Welge, K. H.; Ashfold, M. N. R.; Western C. M. *J. Chem. Phys.* **1990**, *92*, 7027.

## Chapter 3

### The UV Photodissociation Dynamics of Arsine

#### 3.1 Introduction

The ultraviolet photolysis of gaseous  $\text{AsH}_3$  is germane to the fabrication of semiconductor and electro-optical devices.<sup>1-4</sup> For example, it has been demonstrated that the 193.3 nm irradiation of  $\text{AsH}_3$  can be used to stimulate and manipulate the growth of III-V semiconductor compounds such as GaAs, InGaAs, InGaAsP, etc. during metalorganic chemical vapor deposition (MOCVD).<sup>2,3</sup>  $\text{AsH}_3$  is of fundamental scientific interest as well. For example, a sensible goal is a quantitative understanding of how molecular properties and photochemical and photophysical mechanisms vary when the lightest Group-V hydride,  $\text{NH}_3$ , is replaced by progressively heavier counterparts ( $\text{PH}_3$ ,  $\text{AsH}_3$ ,  $\text{SbH}_3$ ,  $\text{BiH}_3$ ) *i.e.*, that span the non-relativistic and relativistic regimes. High quality experimental data for the full complement of Group-V hydrides would comprise a benchmark against which theoretical models could be tested.

Though there has been a great deal of theoretical and experimental research on  $\text{NH}_3$ , much less has been done with the heavier Group-V hydrides. Experimentalists must contend with toxicity and sample preparation / handling issues, and theoreticians must contend with large numbers of electrons and relativistic effects. The increase in nuclear charge has a pronounced effect on electron velocities, especially for *s*-orbitals. As speed

increases (approaching the speed of light for the heaviest elements), radii decrease and orbital energies are lowered.<sup>5,6</sup> This orbital contraction shields the nuclear charge from the valence electrons, leading to ionization energies, bond energies, and orbital energies that do not follow trends that have been established for lighter atoms.<sup>5,6</sup>

Extensive research on the photochemistry and photophysics of NH<sub>3</sub> has yielded high quality potential energy surfaces (PES's) and a consensus regarding the properties of the lowest excited surfaces and the dynamical processes that transpire on them.<sup>7-14</sup> This system is a textbook example of predissociation and nonadiabatic dynamics. The ground state electron configuration is  $(1a_1)^2(2a_1)^2(1e)^4(3a_1)^2$  ( $C_{3v}$  notation). The promotion of an electron from the lone pair orbital  $3a_1$  ( $1a''$  in the  $D_{3h}$  limit) to the  $3s$   $a_1'$  Rydberg orbital accounts for the  $\tilde{A}^1A_2'' \leftarrow \tilde{X}^1A_1$  transition, with its pyramidal-to-planar geometry change. Consequently, the  $\tilde{A} \leftarrow \tilde{X}$  absorption spectrum displays a prominent progression in the  $\nu_2$  umbrella mode.

Vibrational levels of the  $\tilde{A}^1A_2''$  state are predissociated to the extent that there is no discernible rotational structure.<sup>11</sup> There is a small barrier to dissociation on this surface that arises from the Rydberg-to-valence transformation that accompanies lengthening of the N–H bond.<sup>7,9,15</sup> The height of this barrier increases with out-of-plane bend angle (minimizing at planar geometries). For  $\tilde{A}^1A_2''$  vibrational levels  $\nu_2' = 1$  and 2, dissociation proceeds via tunneling through the barrier. An  $\tilde{A}/\tilde{X}$  conical intersection also plays a quite significant role.<sup>7-10</sup>

Referring to figure 3.1, in  $C_{2v}$  symmetry  $\text{NH}_3(\tilde{A})$  correlates diabatically with  $\text{NH}_2(\tilde{X}^2B_1)$ , while  $\text{NH}_3(\tilde{X})$  correlates diabatically with  $\text{NH}_2(\tilde{A}^2A_1)$ . For nonplanar geometries ( $\theta \neq 90^\circ$  in figure 3.1), the  $\text{NH}_3\tilde{X}$  and  $\tilde{A}$  states are each of the same symmetry and there is an avoided crossing. Consequently,  $\text{NH}_3(\tilde{A})$  correlates adiabatically with  $\text{NH}_2(\tilde{A})$ , while  $\text{NH}_3(\tilde{X})$  correlates adiabatically with  $\text{NH}_2(\tilde{X})$ . Figure 3.1 illustrates these aspects of the surfaces.<sup>16</sup>

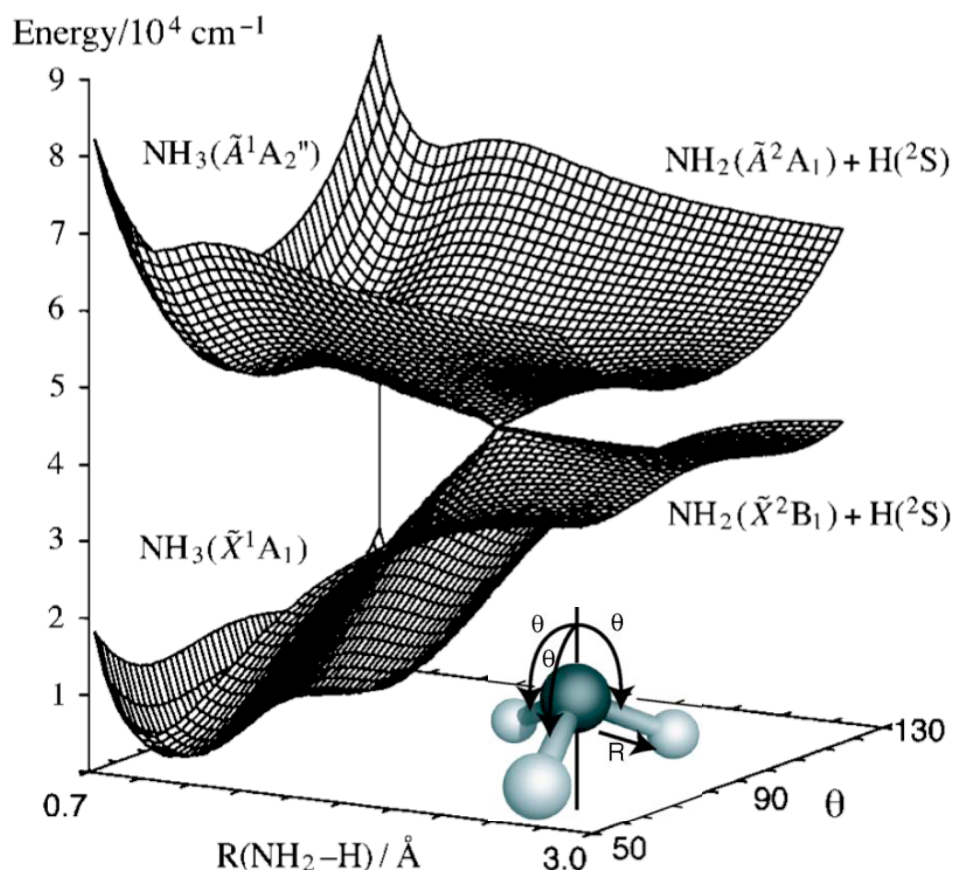


**Figure 3.1.** Conical intersection between the ground and excited surfaces of  $\text{NH}_3$  is indicated (adapted from reference 16). Vertical excitation from the  $\text{NH}_3 X^1A_1$  ground vibrational level to  $\tilde{A}^1A_2''$  can lead to dissociation to  $\text{NH}_2(\tilde{A}^2A_1)$  via adiabatic paths, or to  $\text{NH}_2(\tilde{X}^2B_1)$  via nonadiabatic paths that pass near the conical intersection.  $\theta$  is the angle between an  $\text{NH}$  bond and the normal to the trigonal plane.  $\theta = 90^\circ$  corresponds to planar geometry.

The barrier and conical intersection influence the dissociation dynamics of  $\text{NH}_3(\tilde{A})$ . Biesner *et al.* studied this for  $0 \leq \nu_2' \leq 6$  using H atom photofragment translational energy spectroscopy.<sup>17</sup> They found that  $\text{NH}_2$  is born with significant internal excitation, mainly in the form of *a*-axis rotation. They concluded that  $\text{NH}_3$  out-of-plane bending is encouraged by the shape of the potential in the vicinity of the conical intersection, resulting in considerable  $\text{NH}_2(\tilde{X})$  *a*-axis rotation. In contrast, near-planar dissociation leads to  $\text{NH}_2$  with modest *a*-axis rotation. It is intuitive that umbrella mode vibrational excitation correlates with *a*-axis rotation. It should be noted that competition between adiabatic and nonadiabatic pathways is energy dependent, with  $\text{NH}_2(\tilde{A})$  accounting for 10-30% of the  $\text{NH}_2$  product when  $\text{NH}_3$  is excited to  $\nu_2' = 6$  of its  $\tilde{A}$  state.<sup>17</sup> These experimental findings are in accord with theoretical calculations and results from other experiments.<sup>7,12,14,17</sup>

The dissociation dynamics of  $\text{PH}_3$  are similar to those of  $\text{NH}_3$ , albeit with several important differences. The  $\tilde{A} \leftarrow \tilde{X}$  transition involves the promotion of the lone pair orbital  $5a_1$  to the  $4s$   $a_1$  Rydberg orbital, and calculations indicate a small barrier on the  $\text{PH}_3(\tilde{A})$  surface.<sup>18</sup> The height of this barrier is comparable to the zero point energy of the stretching vibration. The  $\tilde{A} \leftarrow \tilde{X}$  absorption spectrum is a broad continuum, consistent with rapid  $\tilde{A}$  predissociation.<sup>19</sup> Whereas the  $\text{NH}_3(\tilde{A})$  equilibrium geometry is planar, the  $\text{PH}_3(\tilde{A})$  equilibrium geometry has been calculated to be nonplanar ( $\theta_{\text{H-P-H}} \sim 114^\circ$ ).<sup>18</sup> The ground state of  $\text{PH}_3^+$  is also nonplanar,<sup>20</sup> so it is intuitive that  $\text{PH}_3(\tilde{A})$  is nonplanar. The  $\tilde{A} \leftarrow \tilde{X}$  transition increases the equilibrium bond angle from  $93.5^\circ$  to  $114^\circ$ ,<sup>18</sup> which ensures

significant  $\nu_2$  vibrational excitation. Table 3.1 gives values of relevant equilibrium angles for  $\text{NH}_3$ ,  $\text{PH}_3$ , and  $\text{AsH}_3$ .

It has been suggested that the  $\text{PH}_3 \tilde{A}/\tilde{X}$  conical intersection affects the dissociation dynamics in a manner that is analogous to the case of  $\text{NH}_3$ . Several experimental studies have shown that  $\text{PH}_2$  is born with substantial internal excitation,<sup>21-23</sup> though the exact nature of this excitation is more difficult to discern than for  $\text{NH}_2$ . Lambert *et al.*<sup>21</sup> investigated the UV photolysis of

$\text{PH}_3$  by using high- $n$  Rydberg time-of-flight (HRTOF) spectroscopy. They found that  $\text{PH}_2(\tilde{X})$  rovibrational excitation accounts, on average, for  $\sim 62\%$  of the available energy. Structured translational energy distributions indicated significant  $\text{PH}_2(\tilde{X})$   $a$ -axis rotation, as well as bending excitation. It was postulated that  $\text{PH}_2(\tilde{X})$  vibrational excitation is due to the change in bond angle: from  $114^\circ$  in  $\text{PH}_3(\tilde{A})$  to  $91.4^\circ$  in  $\text{PH}_2(\tilde{X})$ . The data also showed evidence of  $\text{PH}_2(\tilde{X})$  photodissociation.

The scarcity of experimental and theoretical data on  $\text{AsH}_3$  is striking compared to what is available for the lighter Group-V hydrides. For example, no information concerning dissociation pathways on  $\tilde{A}$  and  $\tilde{X}$  surfaces is available. However, taking cues from  $\text{PH}_3$  and  $\text{NH}_3$ , it is *assumed* that there is a small barrier to dissociation on  $\tilde{A}$  and an

$\text{NH}_3(\tilde{X}^1A_1)$	$107^\circ$	
$\text{NH}_3(\tilde{A}^1A_2'')$	$120^\circ$	$\text{NH}_3(\tilde{A}) \rightarrow \text{NH}_2(\tilde{X})$
$\text{NH}_2(\tilde{X}^2B_1)$	$103.4^\circ$	$\theta_{\text{H-N-H}}^{\text{equil}} : 120^\circ \rightarrow 103.4^\circ$
$\text{NH}_2(\tilde{A}^2A_1)$	$144^\circ$	
$\text{PH}_3(\tilde{X}^1A_1)$	$93.5^\circ$	
$\text{PH}_3(\tilde{A}^1A_1)$	$114^\circ$	$\text{PH}_3(\tilde{A}) \rightarrow \text{PH}_2(\tilde{X})$
$\text{PH}_2(\tilde{X}^2B_1)$	$91.4^\circ$	$\theta_{\text{H-P-H}}^{\text{equil}} : 114^\circ \rightarrow 91.4^\circ$
$\text{PH}_2(\tilde{A}^2A_1)$	$123.1^\circ$	
$\text{AsH}_3(\tilde{X}^1A_1)$	$92.1^\circ$	
$\text{AsH}_3(\tilde{A}^1E)$	$112^\circ$	$\text{AsH}_3(\tilde{A}) \rightarrow \text{AsH}_2(\tilde{X})$
$\text{AsH}_2(\tilde{X}^2B_1)$	$90.4^\circ$	$\theta_{\text{H-As-H}}^{\text{equil}} : 112^\circ \rightarrow 90.4^\circ$
$\text{AsH}_2(\tilde{A}^2A_1)$	$123^\circ$	

**Table 3.1.** Equilibrium H-M-H angles for M =N, P and As, as related electronic states. See text for details and references.

$\tilde{A}/\tilde{X}$  conical intersection. The  $\tilde{A} \leftarrow \tilde{X}$  absorption is continuous, with weak superimposed structure, as with  $\text{PH}_3$ . Analyses of  $\text{AsH}_3$  and  $\text{PH}_3$  absorption spectra reveal that  $\nu_2' \sim \nu_2''/2$  in these cases, whereas  $\nu_2' \sim \nu_2''$  for  $\text{NH}_3$ .<sup>19</sup> Humphries *et al.* have proposed that the  $\tilde{A}$  states of  $\text{AsH}_3$  and  $\text{PH}_3$  are pyramidal, with  $\tilde{A} \leftarrow \tilde{X}$  transitions terminating on levels that lie above the inversion barrier.<sup>19</sup> Also, the  $\text{AsH}_3$  photoelectron spectrum suggests a pyramidal geometry.<sup>24,25</sup> Thus, the equilibrium bond angle for  $\text{AsH}_3(\tilde{A})$  has been estimated to be  $112^\circ$ , *i.e.*, the  $\text{AsH}_3^+$  bond angle.<sup>26</sup> The equilibrium bond angle for the  $\text{AsH}_3(\tilde{X})$  state is  $92.1^\circ$ .<sup>27</sup> It is noteworthy that a calculation of the lowest excited singlet indicates that it has  $E$  symmetry, which would make this case quite different than the lowest excited singlets of  $\text{NH}_3$  and  $\text{PH}_3$ . This will be discussed later.

Velocity aligned Doppler spectroscopy has been used by Koplitz *et al.* to examine the 193.3 nm (hereafter referred to simply as 193 nm) photodissociation of  $\text{AsH}_3$ .<sup>28</sup> Their results indicate that  $\text{AsH}_2$  fragments are formed with average internal energies  $\sim 2/3$  the available energy. However, the low resolution of the method precluded a determination of the internal energy distribution. An  $\text{AsH}_2 \tilde{A} \rightarrow \tilde{X}$  emission spectrum has been recorded by Ni *et al.* following 193 nm photolysis of  $\text{AsH}_3$ .<sup>29</sup> Both  $\nu_2'$  and  $\nu_2''$  progressions were evident, as well as spectral features that were assigned to As. Photolysis of  $\text{AsH}_2$  was suggested as a possible mechanism for the As emission.

In the study reported here, the 193 nm photodissociation of  $\text{AsH}_3$  has been examined using HRTOF spectroscopy. Figure 3.2 shows a number of possible products.<sup>24,26,30-35</sup> Note that the photon energy is substantially larger than the  $\text{AsH}_3$  bond

dissociation energy. The results indicate that AsH<sub>2</sub> is produced with significant internal excitation. AsH<sub>2</sub>( $\tilde{A}$ ) is also produced, but it is a minor channel. The center-of-mass (c.m.) translational energy distribution,  $P(E_{c.m.})$ , consists of partially resolved structure superimposed on a broad background. Unambiguous assignment is not feasible because the structured features are broad and of modest signal-to-noise ratio (S/N) and there is a significant amount of secondary photolysis.

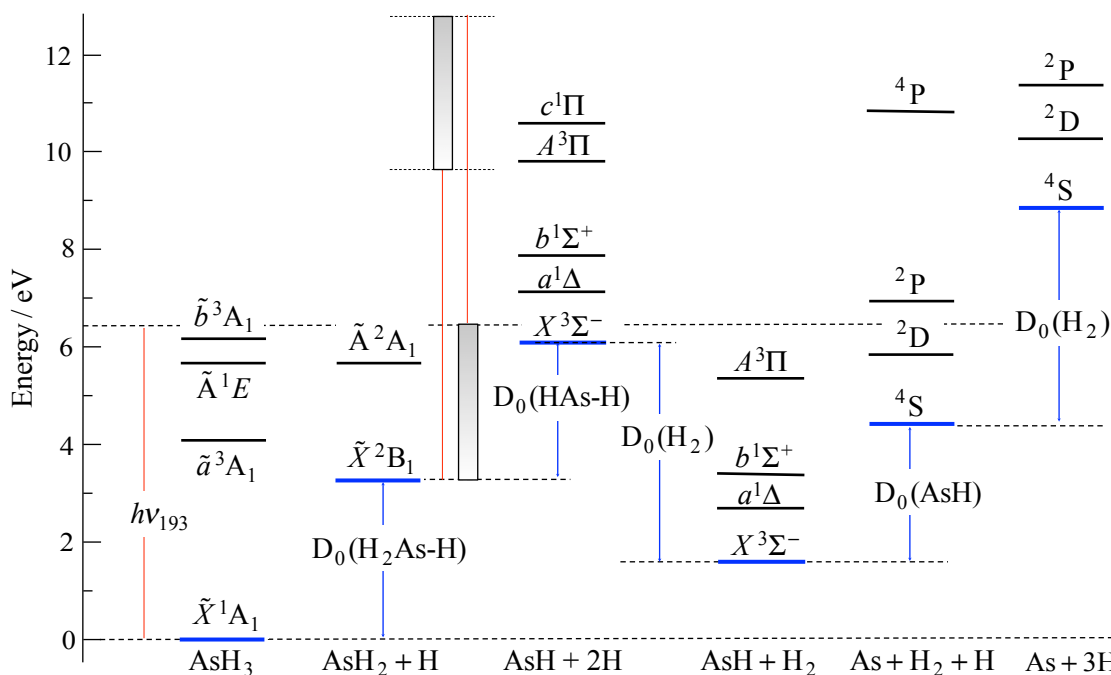


**Figure 3.2.** Energies relevant to 193 nm photolysis of AsH<sub>3</sub> are indicated, including product species that can undergo secondary photodissociation. The two red arrows and shaded rectangles to the right of the AsH<sub>2</sub> + H column indicate the range of energies associated with internally excited AsH<sub>2</sub>. Energy values were obtained as follows: AsH<sub>3</sub> excited states, ref. 26; D<sub>0</sub>(H<sub>2</sub>As-H), ref. 24; AsH<sub>2</sub>( $\tilde{A}$ ), ref. 30; D<sub>0</sub>(HAs-H), ref. 24; D<sub>0</sub>(As-H), ref. 24; AsH excited states, ref. 31-34; As excited states, ref. 35.

In consideration of the photodissociation dynamics of NH<sub>3</sub> and PH<sub>3</sub>, it is suggested that the main features arise from AsH<sub>2</sub>( $\tilde{X}$ ) with substantial *a*-axis rotation, as well as bending excitation. Secondary photolysis of AsH<sub>2</sub>( $\tilde{X}$ ) yields AsH. In light of the

similarities between the present results and those obtained with  $\text{PH}_3$ , it is interesting that the  $\text{AsH}_3(\tilde{A})$  state has been calculated to be  $^1E$ ,<sup>26</sup> whereas the  $\text{PH}_3(\tilde{A})$  state is  $^1A_1$ . The  $\text{AsH}_3$  system lies intermediate between non-relativistic and relativistic regimes. An important goal is that this system achieves the same degree of accord between theory and experiment enjoyed by lighter counterparts.

### 3.2 Experimental

The HRTOF arrangement shown in figure 3.3 has been discussed previously,<sup>36</sup> so only details that are relevant to the present study are given here. A pulsed valve (General Valve, 0.8 mm orifice) expanded

mixtures of  $\text{AsH}_3$  (Matheson Tri-Gas, 99.999%) dilute in a carrier gas (10% in  $\text{H}_2$ , 5% in  $\text{H}_2$ , and 5% in Ar). The molecular beam was collimated 2 cm downstream from

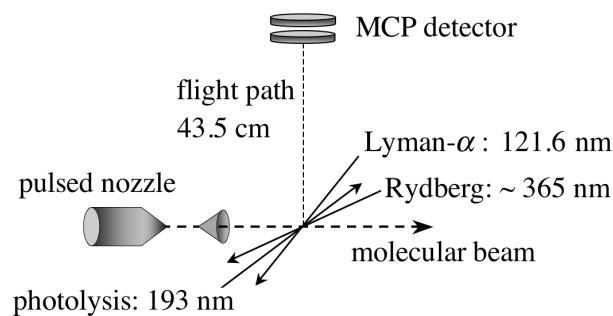


**Figure 3.3.** Interaction region of experimental setup.

the nozzle by a 1 mm diameter skimmer. At the interaction region, 5 cm downstream from the skimmer, the molecular beam was intersected by the outputs of 3 pulsed laser systems.

Photolysis radiation was from an ArF excimer laser (Lambda Physik Compex 201). HRTOF spectroscopy probed nascent H atoms by using sequential excitation to high- $n$  Rydberg levels: 121.6 nm radiation excited H atoms (Lyman- $\alpha$ ) and  $\sim 365$  nm radiation

promoted the excited H atoms to a Rydberg state with  $n \sim 50$ . Two Nd-YAG pump lasers (Continuum Powerlite 8010 and 9010) and two dye lasers were used for this "tagging" of the H atoms. The output of one dye laser (Continuum ND6000, LDS 750 dye) was frequency doubled in a KDP-C crystal, producing 364.8 nm radiation. This was focused into a 10 cm tripling cell, where Lyman- $\alpha$  radiation was generated by non-resonant frequency tripling in Kr. Dissociation of AsH<sub>3</sub> by 121.6 nm radiation was negligible due to the low efficiency of the third harmonic generation. The output of the second dye laser (Continuum ND6000, LDS 750 dye) was frequency doubled, yielding the Rydberg ( $\sim 365$  nm) radiation.

Metastable H atoms that traverse the 43.5 cm flight tube (perpendicular to the interaction region, see figure 3.3) are field ionized and detected with near unit efficiency by two back-to-back microchannel plates (MCP's) in a chevron configuration. A weak dc field applied to a pair of electrodes surrounding the interaction region eliminates ion background signals and makes space anisotropic for high- $n$  Rydberg atoms. This enables high- $n$  Rydberg atoms to be prepared with large orbital angular momentum values and consequently long spontaneous emission lifetimes after they leave the interaction region.

### 3.3 Results

An HRTOF spectrum for the photolysis of jet-cooled AsH<sub>3</sub> is presented in figure 3.4. Vertical dashed lines indicate the earliest arrival time that can be attributed to

primary photolysis using  $D_0$   
 $(H_2As-H) = 74.9 \pm 0.2 \text{ kcal/mol.}^{24}$   
 The signal that precedes the dashed line is evidence of secondary photolysis. Many such spectra were recorded, and no qualitative differences were observed. The one shown in figure 3.4 is one of the better ones.

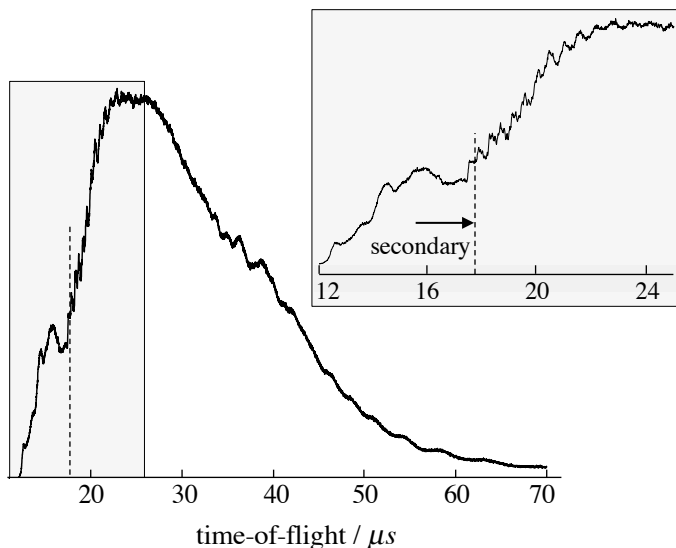


**Figure 3.4.** HRTOF spectrum obtained using 5%  $AsH_3$  and 193 nm photolysis: Results from 121,000 laser firings were summed to obtain the trace. The 193 nm energy ranged between 2.2 and 2.5 mJ. The vertical dashed lines indicate the earliest possible arrival time compatible with 1-photon  $AsH_3$  photodissociation.

Figure 3.5 shows HRTOF

spectra for the photolysis of  $AsH_3$  (10% in  $H_2$ ). These traces were obtained using 193 nm energies of 0.5 and 4.2 mJ. The 193 nm radiation is focused using a 100 cm focal length

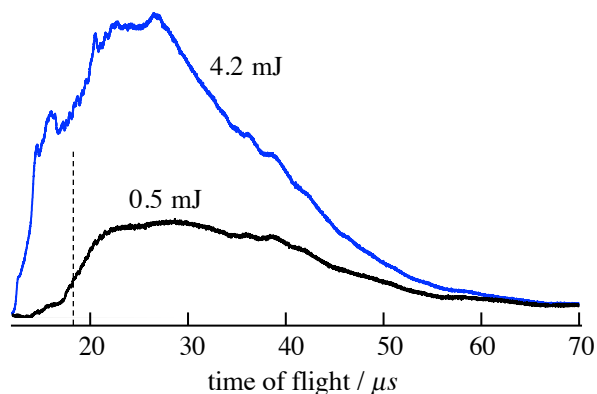


**Figure 3.5.** HRTOF spectra for photolysis energies of 0.5 and 4.2 mJ: 135,000 and 116,000 laser firings, respectively.

lens, resulting in fluences of  $\sim 5$  and  $\sim 40 \text{ J/cm}^{-2}$ , respectively. Reducing the photolysis fluence minimizes the production of fast H atoms that derive from secondary photolysis. However, the broad background was not affected.

Analogous spectra collected using supersonic expansions of 5%  $AsH_3$  in  $H_2$

and 5% AsH<sub>3</sub> in Ar showed no discernible variations from the spectrum in figure 3.4, so they are not presented. The spectrum in figure 3.4 was converted to the c.m. translational energy distribution shown in figure 3.6(a) by using the formulas:

$$E_{c.m.} = \frac{1}{2} m_H \left( \left( \frac{d}{t} \right)^2 + v_{MB}^2 \right) \left( 1 + \frac{m_H}{m_{AsH_2}} \right) \quad (3.01)$$

$$P(E_{c.m.}) \propto t^3 \cdot f(t(E_{c.m.})) \quad (3.02)$$

where  $v_{MB}$  is the molecular beam velocity,  $d$  is the length of the flight tube, and  $t$  is the H-atom arrival time. Referring to equation (3.02), the measured TOF distribution,  $f(t)$ , is converted to the corresponding c.m. translational energy distribution,  $P(E_{c.m.})$ , by using the time-to-energy Jacobian, which is proportional to  $t^3$ , and the relationship between  $t$  and  $E_{c.m.}$  given in equation (3.01). Note:  $P(E_{c.m.})$  applies only to those channels that yield H atoms.

The black dashed line to the right of the red box in figure 3.6(a) indicates the maximum  $E_{c.m.}$  allowed by energy conservation when the H atoms result from primary photolysis. Translational energies in excess of this value derive from secondary photolysis. The inset in figure 3.6(a) shows a fairly abrupt termination of  $P(E_{c.m.})$  at  $51\,800 \pm 500 \text{ cm}^{-1}$ , corresponding to dissociation of AsH<sub>2</sub> with internal energies near  $D_0$  (H-AsH) =  $66.5 \pm 0.02 \text{ kcal/mol}$ ,<sup>24</sup> and negligible AsH internal excitation. The value  $51\,800 \pm 500 \text{ cm}^{-1}$  was obtained by deconvoluting the data to account for instrument resolution.

Background subtraction was used to elucidate peaks in the ranges 1000-10000  $\text{cm}^{-1}$

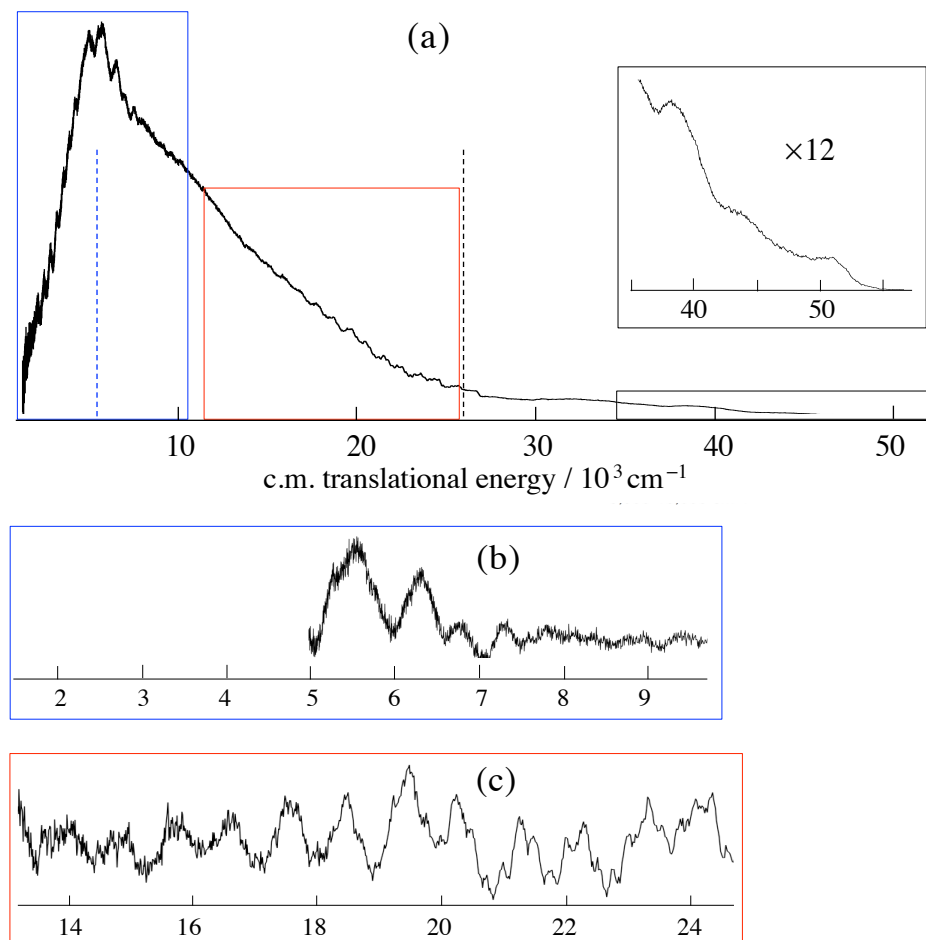


**Figure 3.6.** (a) The HRTOF spectrum in figure 3.4 has been converted to  $P(E_{c.m.})$ ; inset: expanded view of the high-energy region. The black dashed line to the right of the red box indicates the maximum  $E_{c.m.}$  available to a 1-photon process. The blue dashed line in the blue box indicates the maximum  $E_{c.m.}$  available to the  $\text{AsH}_2(\tilde{A})$  channel via a 1-photon process. (b) This pertains to the blue box in (a). To highlight peaks, the underlying continuous distribution has been suppressed (see text). (c) This pertains to the red box in (a). To highlight peaks, the underlying continuous distribution has been suppressed.

[figure 3.6(b)] and 14000-24000  $\text{cm}^{-1}$  [figure 3.6(c)]. The average spacing between peaks in the high-energy region is  $\sim 1000 \text{ cm}^{-1}$ , in rough accord with the  $\text{AsH}_2$  bend frequency.<sup>30</sup> In the low-energy region, the spacing is  $\sim 360 \text{ cm}^{-1}$  for the range 1500-5000  $\text{cm}^{-1}$ . We interpret this as due to  $a$ -axis rotation in  $\text{AsH}_2(\tilde{X})$ , as discussed in the next section.

### 3.4 Discussion

The unambiguous identification of the participating pathways and mechanisms in the 193 nm photodissociation of AsH<sub>3</sub>, as well as its nascent photofragments, is difficult for several reasons. First, the photon energy exceeds greatly the bond dissociation energies of AsH<sub>3</sub> and AsH<sub>2</sub>, thereby enabling highly internally excited fragments to be produced, with a multitude of possible reaction channels. Second, theoretical calculations on AsH<sub>3</sub> and AsH<sub>2</sub> are limited. Third, the presence of significant secondary photolysis adds an unappreciated subtlety to the assignment of the c.m. translational energy distribution. The eye is drawn to the peaks, yet the broad background contains nearly all of the signal, and therefore the real story. The above points compromise our ability to extract product internal energy distributions.

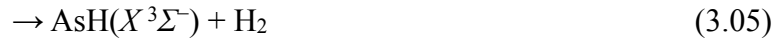
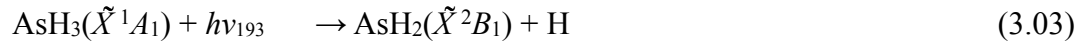
The goal of this section is a qualitative understanding of the photoinitiated decomposition dynamics of the AsH<sub>3</sub> system, in particular *vis-à-vis* its NH<sub>3</sub> and PH<sub>3</sub> counterparts. The NH<sub>3</sub> system has received a great deal of attention owing to its experimental accessibility and its relatively straightforward electronic structure. At the same time, it is important to examine heavier counterparts, and AsH<sub>3</sub> is a good candidate, as it lies intermediate between non-relativistic and relativistic regimes.

#### 3.4.1 Primary photolysis: AsH<sub>3</sub> → AsH<sub>2</sub> + H

The  $P(E_{c.m.})$  distribution shown in figure 3.6(a) is broad, with partially resolved structure and a maximum at low  $E_{c.m.}$ . Despite the presence of secondary photolysis, an

estimate of the "center-of-gravity" of the distribution indicates that AsH<sub>2</sub> internal excitation accounts for ~ 64% of the available energy [*i.e.*,  $E_{avail} = h\nu - D_0(\text{H}_2\text{As-H})$ ]. This is in agreement with the qualitative result of Koplitz *et al.*,<sup>28</sup> who reported that internal excitation accounts for ~ <sup>2</sup>/<sub>3</sub> of the available energy.

Following the absorption of a 193 nm (6.42 eV) photon, the following channels are energetically accessible (also see figure 3.2):



Given that AsH<sub>2</sub>( $\tilde{A}$ ) lies 19 909 cm<sup>-1</sup> above AsH<sub>2</sub>( $\tilde{X}$ ),<sup>30</sup> the maximum  $E_{c.m.}$  that is compatible with reaction (3.04) is 5600 cm<sup>-1</sup> (see figure 3.2). The distribution shown in figure 3.6 indicates that reaction (3.03) dominates, with high AsH<sub>2</sub>( $\tilde{X}$ ) rovibrational excitation. This is reasonable in light of the photodissociation dynamics of PH<sub>3</sub><sup>21-23</sup> and NH<sub>3</sub>.<sup>12-14,17</sup>

Ultraviolet photoexcitation results in a change of equilibrium geometry. The AsH<sub>3</sub> ( $\tilde{X}$ ) electron configuration is  $\dots(a_1)^2(e)^4(a_1)^2$ , and the equilibrium value of the  $\theta_{\text{H-As-H}}$  angle is 92.1°. <sup>27</sup> According to the Walsh diagram for this system, promotion of an  $a_1$  lone pair electron to the Rydberg  $a_1$  orbital increases the  $\theta_{\text{H-As-H}}$  equilibrium angle. <sup>37</sup> This will excite the  $\nu_2$  umbrella mode, as in the analogous  $\tilde{A} \leftarrow \tilde{X}$  transitions in NH<sub>3</sub> and PH<sub>3</sub>. <sup>9,19</sup> It should be noted that the promotion of an  $a_1$  lone pair electron to other excited orbitals in this energy region might also result in umbrella mode excitation.

The photoinitiated dissociation dynamics of NH<sub>3</sub> provides insight. The NH<sub>3</sub>  $\tilde{A} \leftarrow \tilde{X}$  absorption spectrum exhibits a resolved  $\nu_2$  progression that reflects the pyramidal-to-planar geometry change. Experimental studies of the state selected (*i.e.*,  $\nu_2'$ ) photodissociation of NH<sub>3</sub>( $\tilde{A}$ ) confirm that NH<sub>2</sub> is formed with significant internal excitation that is primarily in the form of  $a$ -axis rotation. <sup>12,17</sup> Not surprisingly, the amount of NH<sub>2</sub> internal excitation increases with photon energy. Moreover, excitation of the NH<sub>2</sub> bend has been observed following dissociation via higher  $\nu_2'$ . <sup>14,16,17</sup> Theory and experiment confirm that dissociation commencing from the  $\tilde{A}$  surface is sensitive to: (i) its vibrational state; (ii) geometries and motions sampled during fragmentation; (iii) the topography of the conical intersection region; and (iv) competition between adiabatic and nonadiabatic pathways. <sup>7-14,16,17</sup>

Dissociation to ground electronic state products is governed by the  $\tilde{A}/\tilde{X}$  conical intersection. For example, trajectory calculations of Biesner *et al.* illustrate the intersection's influence on energy disposal into product degrees of freedom. <sup>12</sup> Referring

to figure 3.1, trajectories are funneled toward the intersection, and nonadiabatic transitions are facilitated by near-planar geometry. Dissociation to  $\text{NH}_2(\tilde{X})$  can occur either on the first pass through the intersection region or, if this fails, on a subsequent pass. The intersection region has a large gradient in the angular coordinate that promotes  $\text{NH}_2(\tilde{X})$   $a$ -axis rotation. Trajectories that fail to emerge on the  $\text{NH}_2(\tilde{A})$  asymptote in the first pass through the conical intersection region can sample more of the  $\tilde{A}$  surface.<sup>12</sup>

Dissociation of  $\text{NH}_3$  from higher  $v_2'$  leads to  $\text{NH}_2$  with larger amounts of vibrational and electronic excitation.<sup>14,17</sup> Competition ensues between adiabatic and nonadiabatic pathways once the threshold for  $\text{NH}_2(\tilde{A})$  has been reached ( $v_2' \geq 3$ ).  $\text{NH}_3(\tilde{A})$  that dissociates via markedly nonplanar configurations, thereby avoiding the conical intersection region, does so on the surface that correlates to  $\text{NH}_2(\tilde{A})$ . Loomis *et al.* used time resolved Fourier transform infrared (FTIR) emission spectroscopy to investigate 193 nm  $\text{NH}_3$  photodissociation.<sup>14</sup> They found a bimodal  $\text{NH}_2(\tilde{A})$  rotational distribution that they attributed to near-planar and bent geometries that dissociate. Angular momentum conservation dictates that (for  $J = 0$  parent) the angular momentum of  $\text{NH}_2$  is equal and opposite the orbital angular momentum of the fragment pair.<sup>13</sup> Dissociation from  $\text{NH}_3(\tilde{A})$  is rapid,  $\sim 20$  fs. Thus, out-of-plane bending is manifest as  $a$ -axis rotation of the  $\text{NH}_2(\tilde{A})$  product.<sup>14</sup>

### 3.4.2 AsH<sub>2</sub> internal excitations

Given that a 193 nm photon prepares AsH<sub>3</sub>( $\tilde{A}$ ) with significant  $\nu_2$  (umbrella) vibrational excitation, and in light of the similarities between AsH<sub>3</sub> and PH<sub>3</sub> and between AsH<sub>2</sub> and PH<sub>2</sub>, it is reasonable to expect the participating pathways and dissociation dynamics of AsH<sub>3</sub> to resemble those of PH<sub>3</sub>. For example, consider the different  $\theta_{\text{H-M-H}}$  equilibrium values that exist between parent and product species. The equilibrium values of  $\theta_{\text{H-P-H}}$  for PH<sub>3</sub>( $\tilde{A}$ ) and PH<sub>2</sub>( $\tilde{X}$ ) are 114° and 91.4°, respectively.<sup>18,38</sup> This large difference of 22.6° can lead to significant bending excitation in the PH<sub>2</sub>( $\tilde{X}$ ) product that accrues via the diabatic surface that correlates PH<sub>3</sub>( $\tilde{A}$ ) to PH<sub>2</sub>( $\tilde{X}$ ).

Note that, in this regard, PH<sub>3</sub> differs (perhaps significantly) from NH<sub>3</sub>. The equilibrium values of  $\theta_{\text{H-N-H}}$  for NH<sub>3</sub>( $\tilde{A}$ ) and NH<sub>2</sub>( $\tilde{X}$ ) are 120° and 103.4°,<sup>7</sup> respectively: a change of 16.6°. This is 6° less than the 22.6° change that occurs with PH<sub>3</sub>. Without a detailed calculation, however, it is not feasible to infer the degree of vibrational excitation present in the triatom product given the  $\theta_{\text{H-M-H}}$  equilibrium angles for a parent and its triatom product. Specifically, though the angular change in going from parent to products is large, the degree of vibrational adiabaticity along the reaction coordinate must be assessed.

Because of this vibrational adiabaticity, differences of 22.6° versus 16.6° might result in larger fractional differences in the degree of triatom bending excitation. For example, Lambert *et al.* observed PH<sub>2</sub> with substantial bending excitation and *a*-axis

rotation following the ultraviolet photolysis of PH<sub>3</sub>.<sup>21</sup> In contrast, it is known that NH<sub>2</sub> is formed with a relatively modest amount of bending excitation.<sup>12-14,17</sup>

The equilibrium bond angles for AsH<sub>3</sub>( $\tilde{A}$ ) and AsH<sub>2</sub>( $\tilde{X}$ ) are 112° and 90.4°, respectively.<sup>26,39</sup> These values and their 21.6° difference are close to those of their PH<sub>3</sub> counterparts (114°, 91.4°, 22.6°, respectively). Thus, it is reasonable to expect AsH<sub>2</sub> to be formed with high internal excitation, specifically, *a*-axis rotation *and* bending excitation.

This is consistent with our data. The structure in the  $P(E_{c.m.})$  distribution at low translational energies [figure 3.6(b)] is consistent with AsH<sub>2</sub>( $\tilde{X}$ ) having significant *a*-axis rotation. For example, to rationalize the peaks in figure 3.6(b), rotational energies for AsH<sub>2</sub>( $\tilde{X}$ ), which is a near-oblate top ( $\kappa = 0.8034$ ),<sup>30</sup> were calculated using the formulas:

$$F(J, K_c) = \bar{B}J(J + 1) + K_c^2(C - \bar{B}) \quad (4.13)$$

$$\bar{B} = (A + B)/2 \quad (4.14)$$

Values of rotational constants: *A*, *B*, and *C* are 7.550, 7.162, and 3.615 cm<sup>-1</sup>, respectively,<sup>30</sup> and  $F(J, K_c)$  is the rotational energy.

Energy separations between calculated rotational levels matched the lower-energy spacings in figure 3.6(b). The structure below 5000 cm<sup>-1</sup> is fit with *J* values in the range 46-54, as indicated in figure 3.7. The large amount of AsH<sub>2</sub>( $\tilde{X}$ ) internal energy, the complex energy disposal and the scarcity of spectroscopic data make unique assignment impossible. Other sets of rotational levels also fit the data. However, the peaks cannot be fit using any reasonable choice of vibrational frequencies. Moreover, the established

propensity toward  $a$ -axis rotation is consistent with low  $K_c$  values. For example, including  $K_c$  values up to 10 does not alter the fit to the data indicated in figure 3.7. The "bottom line" is that these estimates are consistent with  $\text{AsH}_2(\tilde{X})$  being born with significant  $a$ -axis rotation.

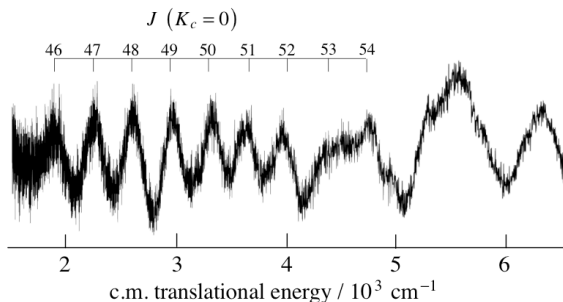


**Figure 3.7.** Low energy features can be fit using high  $J$  values and various distributions of low  $K_c$  values.

Figure 3.6(c) highlights the structure present at the higher  $E_{c.m.}$  values. Separations between peaks (though the data are of low S/N) are comparable to the bend of  $\text{AsH}_2(\tilde{X})$ .<sup>30</sup> Why does this structure occur at higher translational energy? Again, qualitative guidance is available from  $\text{NH}_3$ .  $\text{NH}_3(\tilde{A})$  that retains near- $C_{2v}$  symmetry during dissociation passes through the conical intersection region to form  $\text{NH}_2(\tilde{X})$  in low rotational states.<sup>12</sup> Loomis *et al.* used an impulsive model to rationalize the efficient disposal of energy into  $\text{NH}_2$  bending excitation for planar dissociation.<sup>14</sup>  $\text{AsH}_3(\tilde{A})$  that remains near-planar during dissociation has a high probability of undergoing a non-adiabatic transition. The resulting  $\text{AsH}_2(\tilde{X})$  will have bending excitation because of the change in equilibrium bond angle in going from  $\text{AsH}_3(\tilde{A})$  to  $\text{AsH}_2(\tilde{X})$ , but less  $a$ -axis rotation than molecules that dissociate having considerable umbrella mode excitation.

Adiabatic and nonadiabatic transitions compete.  $\text{AsH}_3(\tilde{A})$  arises from  $\text{AsH}_2(\tilde{X})$  that dissociates mainly from geometries that avoid the conical intersection region. Therefore,  $\text{AsH}_2(\tilde{A})$  is expected to have  $a$ -axis rotational excitation. Though the equilibrium angles

of  $\text{AsH}_3(\tilde{A})$  and  $\text{AsH}_2(\tilde{A})$  ( $112^\circ$  and  $123^\circ$ , respectively)<sup>26,39</sup> differ by a smaller amount than for  $\text{AsH}_3(\tilde{A})$  and  $\text{AsH}_2(\tilde{X})$  ( $112^\circ$  and  $90.4^\circ$ , respectively),<sup>26,39</sup> it is not unreasonable to anticipate  $\text{AsH}_2(\tilde{A})$  bending excitation.

$\text{AsH}_2(\tilde{A})$  is a near-prolate top ( $\kappa = -0.8249$ ).<sup>30</sup> Rotational energies were estimated using:

$$F(J, K_a) = \bar{B}J(J + 1) + K_a^2(A - \bar{B}) \quad (4.15)$$

where

$$\bar{B} = (B - C)/2 \quad (4.16)$$

and  $A$ ,  $B$ , and  $C$  values are  $17.207$ ,  $4.920$ , and  $3.740 \text{ cm}^{-1}$ .<sup>30</sup> Peak separations in figure 3.6 (b) could not be fit using these calculated spacings.

### 3.4.3 Secondary photolysis: $\text{AsH}_2 \rightarrow \text{AsH} + \text{H}$

Our considerations here are restricted to secondary photolysis processes that yield H atom fragments. Channels that yield  $\text{H}_2$  are not considered. Figures 3.4-3.6 indicate that the photodissociation of  $\text{AsH}_3$  yields  $\text{AsH}_2$  with significant internal excitation, and that this species is photolyzed. Energy conservation requires:

$$h\nu_{193} + E_{\text{AsH}_2} - D_0(\text{HAs-H}) = E_{\text{AsH}} + E_{c.m.} \quad (3.17)$$

where  $E_{\text{AsH}_2}$  and  $E_{\text{AsH}}$  are the internal energies of  $\text{AsH}_2$  and  $\text{AsH}$ , respectively. For those instances in which  $E_{\text{AsH}_2} \approx D_0(\text{HAs-H})$  and  $E_{\text{AsH}}$  is negligible,  $E_{c.m.}$  is approximately equal to  $h\nu_{193}$ . In this case, the photon energy ( $51,780 \text{ cm}^{-1}$ ) appears as  $E_{c.m.}$ .

Indeed, the inset in figure 3.6(a) a fairly abrupt termination of  $P(E_{c.m.})$  at  $51\,800 \pm 500 \text{ cm}^{-1}$ . This is also easy to see in the TOF spectrum in figure 3.4. Namely, the arrival time for which  $E_{c.m.} = h\nu_{193}$  is  $12.4 \mu\text{s}$ , which coincides with the sharp onset of signal in the TOF spectrum. Thus,  $\text{AsH}_2$  is formed with a distribution of internal energies that extends all the way up to  $D_0(\text{HAs-H})$ .

Many channels are accessible when  $\text{AsH}_2$  absorbs a 193 nm photon. Referring to figure 3.2, photodissociation of  $\text{AsH}_2(\tilde{X})$  from even its lowest rovibrational level can, on energetic grounds, access a number of product channels. Because  $\text{AsH}_2$  contains significant internal excitation, the possibilities are legion.

Though  $\text{AsH}(a^1\Delta)$  and  $\text{AsH}(b^1\Sigma^+)$  are energetically accessible via secondary photolysis, emission from these species has not been observed following 193 nm excitation.<sup>29</sup> This can be due to the fact that singlet-triplet emission is weak, or that these channels are not accessed.  $\text{AsH}(A^3\Pi)$  is energetically accessible when  $\text{AsH}_2(\tilde{X})$  contains more than  $1500 \text{ cm}^{-1}$  of internal energy prior to its photoexcitation. Nonetheless,  $\text{AsH}_2(\tilde{A})$  has not been detected in emission following 193 nm photolysis of  $\text{AsH}_3$ .

Photodissociation of  $\text{AsH}_2(\tilde{X})$  that has  $E_{\text{AsH}_2} \leq D_0(\text{HAs-H})$  can, on energetic grounds, yield  $\text{AsH}(\tilde{X})$  and  $\text{AsH}(\tilde{A})$  with  $E_{c.m.} \leq 51\,700 \text{ cm}^{-1}$  and  $\leq 21\,700 \text{ cm}^{-1}$ , respectively. The  $E_{c.m.}$  distribution in figure 3.6 is broad, peaking at  $\sim 6\,000 \text{ cm}^{-1}$ . Vibrational excitation in  $\text{AsH}$  is expected to be modest on the basis of changes of bond lengths:  $1.483 \text{ \AA}$  in  $\text{AsH}_2(\tilde{A})$ ;<sup>39</sup>  $1.534 \text{ \AA}$  in  $\text{AsH}(\tilde{X})$ ;<sup>32</sup>  $1.577 \text{ \AA}$  in  $\text{AsH}(\tilde{A})$ .<sup>32</sup> Though PES's are not available, possible pathways can be considered in light of symmetry and spin.<sup>39</sup>  $\text{AsH}_2(\tilde{X}^2B_1)$  and

AsH<sub>2</sub>( $B^4B_1$ ) correlate to AsH( $\tilde{X}^3\Sigma^-$ ) + H( $^2S$ ), whereas AsH<sub>2</sub>( $\tilde{A}^2A_1$ ) does not correlate to AsH( $\tilde{X}^3\Sigma^-$ ). For PH<sub>2</sub>, it has been noted that  $\tilde{A}$  may predissociate via  $^4B_1$  because of spin-orbit interaction.<sup>40</sup> However,  $^4B_1$  is much higher in energy than  $^2A_1$ , so predissociation of  $^2A_1$  via  $^4B_1$  is considered unlikely in the present experiments.

### 3.5 Conclusions

HRTOF spectroscopy has been used to examine the 193 nm photodissociation of AsH<sub>3</sub>. Contributions from secondary AsH<sub>2</sub> photodissociation are also present. The degree of secondary photodissociation can be minimized, but not eliminated, by using low 193 nm fluences. The experimental method is only sensitive to product channels that give H atoms, *i.e.*, an elimination channel such as AsH<sub>2</sub> → As + H<sub>2</sub> cannot be detected using the present arrangement. The main experimental result is a broad  $P(E_{c.m.})$  distribution that contains a modest amount of superimposed structure.

The dominant reaction pathway is AsH<sub>3</sub> → AsH<sub>2</sub>( $\tilde{X}$ ) + H. Nascent AsH<sub>2</sub>( $\tilde{X}$ ) has considerable rovibrational excitation. The average value of  $E_{AsH_2}$  is  $\approx 16\,300\text{ cm}^{-1}$ , which is  $\approx 64\%$  of the available energy:  $E_{avail} = h\nu - D_0(\text{H}_2\text{As}-\text{H})$ . The distribution of  $E_{AsH_2}$  values extends to values as large as  $D_0(\text{HAs}-\text{H})$ . For those cases in which  $E_{AsH_2} \approx D_0(\text{HAs}-\text{H})$  and  $E_{AsH}$  is negligible, AsH<sub>2</sub> photodissociation yields  $E_{c.m.} \approx h\nu_{193}$ . This is manifest as a fairly abrupt termination of  $P(E_{c.m.})$  at  $51\,800 \pm 500\text{ cm}^{-1}$  [inset in figure 3.6(a)], which matches  $h\nu_{193} = 51\,780\text{ cm}^{-1}$ . This confirms that AsH<sub>2</sub> is formed with a distribution of internal energies that extends all the way to  $D_0(\text{HAs}-\text{H})$ .

It is known that  $\text{AsH}_2(\tilde{A})$  is produced because its fluorescence has been detected,<sup>37</sup> though its yield could not be determined in the fluorescence measurements. In the present experiments, its yield is found to be modest. This follows from the fact that  $E_{c.m.}$  must be  $\leq 5600 \text{ cm}^{-1}$  for the  $\text{AsH}_2(\tilde{A})$  channel (figure 3.2), and this energy range accounts for a modest fraction of the observed  $P(E_{c.m.})$  distribution. Thus, most of the reactive flux passes from electronically excited  $\text{AsH}_3$  to ground electronic state products, presumably via a nonadiabatic transition mechanism similar to those of  $\text{PH}_3$  and  $\text{NH}_3$ .

The 193 nm photolysis of  $\text{AsH}_3$  has much in common with that of  $\text{PH}_3$ . On the basis of the  $\text{PH}_3$  experimental data and known  $\text{PH}_3$ ,  $\text{PH}_2$ ,  $\text{AsH}_3$ , and  $\text{AsH}_2$  geometrical properties,  $\text{AsH}_2$  bending excitation is expected. For example, note the differences between equilibrium angles  $\theta_{\text{H-M-H}}$ :  $114^\circ \rightarrow 91.4^\circ$  for  $\text{PH}_3(\tilde{A}) \rightarrow \text{PH}_2(\tilde{X})$ ; and  $112^\circ \rightarrow 90.4^\circ$  for  $\text{AsH}_3(\tilde{A}) \rightarrow \text{AsH}_2(\tilde{X})$ . The separations between adjacent peaks in the structure present in the *high-energy* region of the  $P(E_{c.m.})$  distribution [figure 3.6(c)] are in qualitative accord with  $\text{AsH}_2(\tilde{X})$  bending quanta.

Separations between adjacent peaks in the *low-energy* region of the  $P(E_{c.m.})$  distribution are in accord with  $\text{AsH}_2(\tilde{X})$  rotational levels. This is consistent with a mechanism in which parent umbrella motion evolves to *a*-axis rotation of the  $\text{AsH}_2(\tilde{X})$  product, as occurs with the lighter Group-V hydrides.

An experimental study of the photodissociation of jet-cooled  $\text{AsH}_2$  samples in which there is no contribution from  $\text{AsH}_3$  background would resolve a number of issues. For example, this could be achieved by photodissociating  $\text{AsH}_3$  in a high-pressure quartz

expansion channel, and then photodissociating expansion-cooled AsH<sub>2</sub> in spectral regions where AsH<sub>3</sub> does not absorb radiation.

Theory is in good shape for NH<sub>3</sub>, but the same is not true for AsH<sub>3</sub>. Accurate electronic structure calculations will go a long way toward elucidating mechanisms and provide a detailed quantitative understanding of the photophysics and photochemistry of the full range of Group-V hydrides. It is imperative that calculations for the heavier species are done at a high level of theory if experimental results are to be reconciled with confidence.

### 3.6 Chapter 3 References

1. Donnelly, V. M.; Karlicek, R. F. *J. Appl. Phys.* **1982**, *53*, 6399.
2. Pütz, N.; Heinecke, H.; Veuhoff, E.; Arens, G.; Heyen, M.; Lüth, H.; Balk, P. *J. Cryst. Growth* **1984**, *68*, 194.
3. Kukimoto, H.; Ban, Y.; Komatsu, H.; Takechi, M.; Ishizaki, M. *J. Cryst. Growth* **1986**, *77*, 223.
4. Aoyagi, Y.; Kanazawa, M.; Doi, A.; Iwai, S.; Namba, S. *J. Appl. Phys.* **1986**, *60*, 3131.
5. Balasubramanian, K. *Relativistic Effects in Chemistry, Parts A and B*; Wiley & Sons: New York, 1997.
6. Pitzer, K. *Acc. Chem. Res.* **1979**, *12*, 271.
7. McCarthy, M. I.; Rosmus, P.; Werner, H. J.; Botshwina, P.; Vaida, V. *J. Chem. Phys.* **1987**, *86*, 6693.
8. Ranu, R.; Peyerimhoff, S. D.; Buenker, R. J. *J. Mol. Spectrosc.* **1977**, *68*, 253.
9. Rosmus, P.; Botschwina, P.; Werner, H. J.; Vaida, V.; Engelking, P. C.; McCarthy, M. I. *J. Chem. Phys.* **1987**, *86*, 6677.
10. Nangia, S.; Truhlar, D. G. *J. Chem. Phys.* **2006**, *124*, 124309.
11. Vaida, V.; McCarthy, M. I.; Engelking, P. C.; Rosmus, P.; Werner, H. J.; Botschwina, P. *J. Chem. Phys.* **1987**, *86*, 6669.
12. Biesner, J.; Schnieder, L.; Ahlers, G.; Xie, X.; Welge, K. H.; Ashfold, M. N. R.; Dixon, R. N. *J. Chem. Phys.* **1988**, *88*, 3607.
13. Mordaunt, D.; Ashfold, M. N. R.; Dixon, R. N. *J. Chem. Phys.* **1996**, *104*, 6460.
14. Loomis, R. A.; Reid, J. P.; Leone, S. *J. Chem. Phys.* **2000**, *112*, 658.

15. Kassab, E.; Gleghorn, J. T.; Evleth, E. M. *J. Am. Chem. Soc.* **1983**, *105*, 1746.
16. Hause, M. L.; Yoon, Y. H.; Crim, F. F. *J. Chem. Phys.* **2006**, *125*, 174309.
17. Biesner, J.; Schnieder, L.; Ahlers, G.; Xie, X.; Welge, K. H.; Ashfold, M. N. R.; Dixon, R. N. *J. Chem. Phys.* **1989**, *91*, 2901.
18. Müller, J.; Ågren, H. *J. Chem. Phys.* **1982**, *76*, 5060.
19. Humphries, C. M.; Walsh, A. D.; Warsop, P. A. *Discuss. Faraday Soc.* **1963**, *35*, 148.
20. Maripuu, R.; Reineck, I.; Ågren, H.; Nian-Zu, W.; Rong, J. M.; Veenhuizen, H.; Shamma, S. H.; Karlsson, L.; Siegbahn, K. *Mol. Phys.* **1983**, *48*, 1255.
21. Lambert, I. R.; Morley, G. P.; Mordaunt, D. H.; Ashfold, M. N. R.; Dixon, R. N. *Can. J. Chem.* **1994**, *72*, 977.
22. Baugh, D.; Koplitz, B.; Xu, Z.; Wittig, C. *J. Chem. Phys.* **1988**, *88*, 879.
23. Sam, C. L.; Yardley, J. T. *J. Chem. Phys.* **1978**, *69*, 4621.
24. Berkowitz, J. *J. Chem. Phys.* **1988**, *89*, 7065.
25. Potts, A. W.; Price, W. C. *Proc. R. Soc. London Ser. A.* **1972**, *326*, 181.
26. Dai, D.; Balasubramanian, K. *J. Chem. Phys.* **1990**, *93*, 1837.
27. Binning Jr., R. C.; Curtiss, L. A. *J. Chem. Phys.* **1990**, *92*, 1860.
28. Koplitz, B.; Xu, Z.; Wittig, C. *Appl. Phys. Lett.* **1988**, *52*, 860.
29. Ni, T.; Lu, Q.; Ma, X.; Yu, S.; Kong, F. *Chem. Phys. Lett.* **1986**, *126*, 417.
30. He, S.-G.; Clouthier, D. J. *J. Chem. Phys.* **2007**, *126*, 154312.

31. Balasubramanian, K; Nannegari, V. *J. Mol. Spectrosc.* **1989**, *138*, 482.
32. Dixon, R. N.; Lamberton, H. M. *J. Mol. Spectrosc.* **1968**, *25*, 12.
33. Aren, M.; Richter, W. *J. Chem. Phys.* **1990**, *93*, 7094.
34. Buetel, M.; Setzer, K. D.; Shestakov, O.; Fink, E. H. *J. Mol. Spectrosc.* **1996**, *178*, 165.
35. Moore, C. E. *Atomic Energy Levels*; National Bureau of Standards: Washington, DC, 1971.
36. Zhang, J.; Riehn, C. W.; Dulligan, M.; Wittig, C. *J. Chem. Phys.* **1996**, *104*, 7027.
37. Walsh, A. D. *J. Chem. Soc.* **1953**, 2296.
38. Berthou, J. M.; Pascat, B.; Guenebaut, H.; Ramsay, D. A. *Can. J. Phys.* **1972**, *50*, 2265.
39. Dixon, R. N.; Duxbury, G.; Lamberton, H. M. *Proc. R. Soc. London Ser. A.* **1968**, *305*, 271.
40. Xuan, C. N; Margani, A. *J. Chem. Phys.* **1994**, *100*, 7000.

# Chapter 4

## Supplemental Data,

### Design Considerations and Safety

*- It is imperative in the design process to have a full and complete understanding of how failure is being obviated in order to achieve success.*

*- Henry Petroski*

#### 4.1 Introduction

This information in this chapter was generated over the course of experimental work in the Wittig laboratory. Many of the molecules discussed subsequently herein were the principle species of interest for HRTOF photodissociation dynamics studies, but never came to full experimental fruition. Despite these shortcomings, much useful information was collected concerning the spectroscopy, syntheses, analyses and observations from work with these systems.

The second half of this chapter is intended to aid any researchers subsequently using the experimental apparatus described in the preceding chapters. This will be particularly useful for anyone attempting to perform experiments alone or with little knowledge of the operational history of the equipment. These are challenging experiments when fully staffed and under the best of conditions.

## 4.2 Supplemental Data

Throughout the course of experimentation in the Wittig lab, several species of interest for molecular dynamics studies were generated. Although high  $n$ -Rydberg time-of-flight (HRTOF) studies eluded some of these species due to many technical and logistical challenges, several were successfully synthesized and spectroscopically characterized. Much useful information was collected and can provide use for any future experiments requiring them. This section provides an account of the syntheses performed and the spectra used to confirm the identity of the species of interest.

### 4.2.1 Antimony Trihydride (SbH<sub>3</sub>)

Although antimony trihydride (stibine, SbH<sub>3</sub>) provided many points of interest for molecular dynamics experiments, working with it was not without challenges. Along with the safety considerations mentioned later in section 4.5, stibine is not commercially available and required synthesizing. The modified synthesis of stibine<sup>1</sup> was carried out in a custom-built glass manifold (figure 4.1) designed and purpose built in a blast proof fume hood. As stibine decomposes autocatalytically to hydrogen gas and atomic antimony at room temperature, product stability is of critical concern. This inherent instability necessitated that all reaction components be made of glass, and proper cleaning and passivation of the glassware was necessary. All glassware was first treated with warm *aqua fortis*, followed by an immersion in warm methyl acetate. After a drying period, the apparatus was assembled and vacuum leak tested. The

## Antimony Trihydride ( $\text{SbH}_3$ ) Synthesis Apparatus

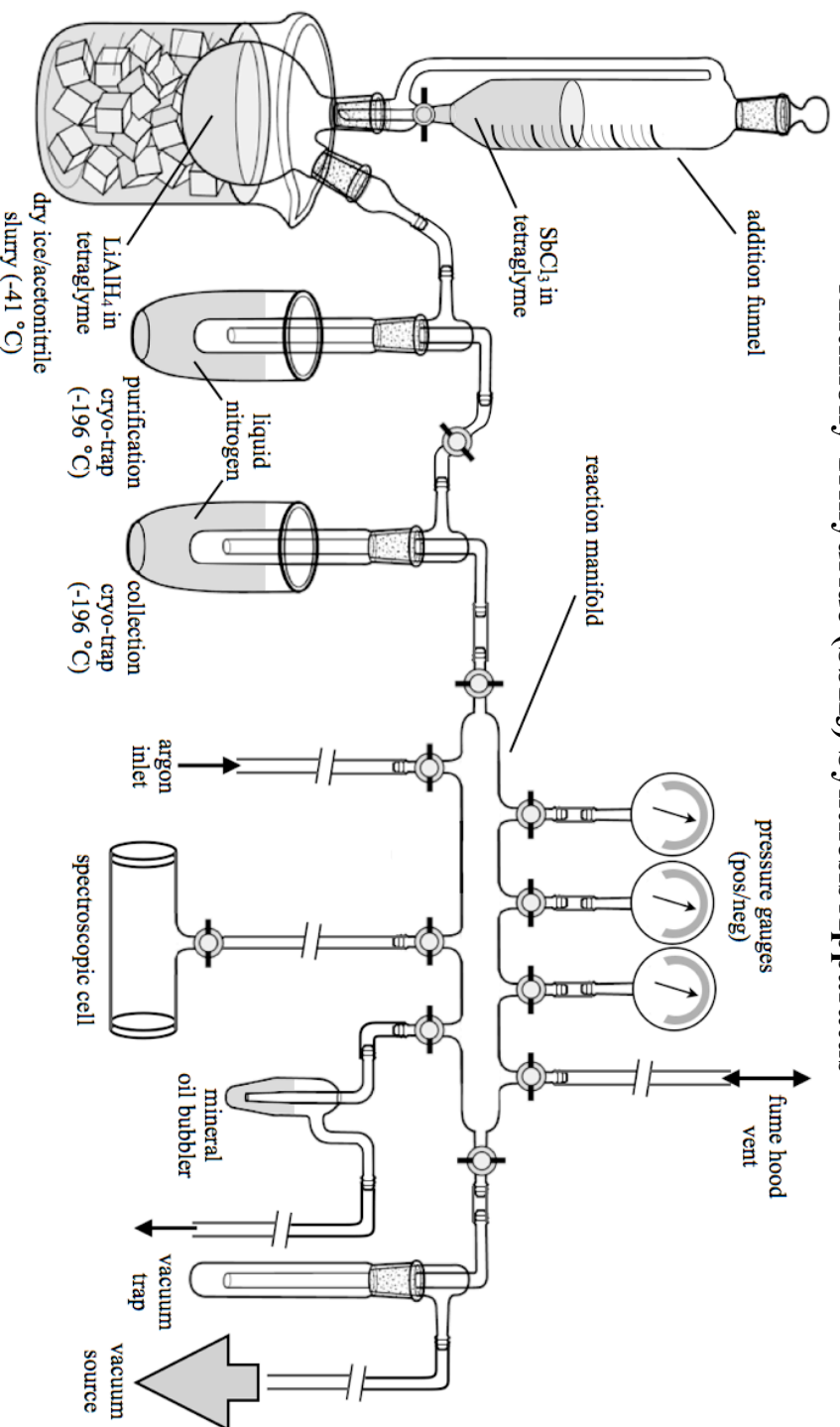


**Figure 4.1.** The custom built experimental apparatus for the synthesis, dilution, spectroscopic identification and sample preparation of stibine ( $\text{SbCl}_3$ ). The apparatus was constructed of glass inside a custom blast-proof negative pressure cabinet. The synthesis apparatus was adapted from reference 1, and modified to suit scale and other requirements for laboratory needs. The final sample of solid  $\text{SbCl}_3$  was generated in the collection cryo-trap where it could be removed and plumbed into the vacuum chamber sample introduction system.

glassware was then baked out under vacuum to drive off any unwanted water vapor from inside the system.

A suspension of  $\sim 0.50$  g of lithium aluminum hydride ( $\text{LiAlH}_4$ ) in 100 mL of tetraglyme was added to a 500 mL round bottom flask and immersed in an ice slurry of acetone.<sup>2</sup> The suspension was cooled for 30 min. A suspension of  $\sim 0.50$  g antimony trichloride ( $\text{SbCl}_3$ ) in 100 mL tetraglyme was added slowly to the round bottom flask and the reaction was allowed to evolve under vacuum. The reaction vessel was attached to two serial cryo traps immersed in liquid nitrogen. The first trap was a purification trap and the second was a collection trap to condense the solid  $\text{SbH}_3$ .

Once the reaction was complete, the manifold was evacuated and a sample of the product gas was collected in a custom built spectroscopic cell for UV-visible analysis. The collected UV-visible absorption spectra can be seen in figure 4.2, along with the reference spectrum for identity confirmation.<sup>3</sup> Figures 4.2 (A) and (B) show results from time studies performed to establish the stibine lifetime in the quartz cell. This stability time was of critical importance for preparation of the collection trap and connection hardware to the vacuum chamber for study. Upon completion of the final sample and spectroscopic confirmation, the collection trap was sealed off and detached from the reaction apparatus while remaining submerged in a liquid nitrogen dewar. This dewar and trap were then plumbed between an argon carrier gas source and the main vacuum chamber. The collection trap and plumbing were evacuated and held under vacuum. Argon was flowed through the collection trap, passed over the solid  $\text{SbH}_3$  which

## Antimony Trihydride ( $\text{SbH}_3$ ) UV-Visible Absorption Spectra

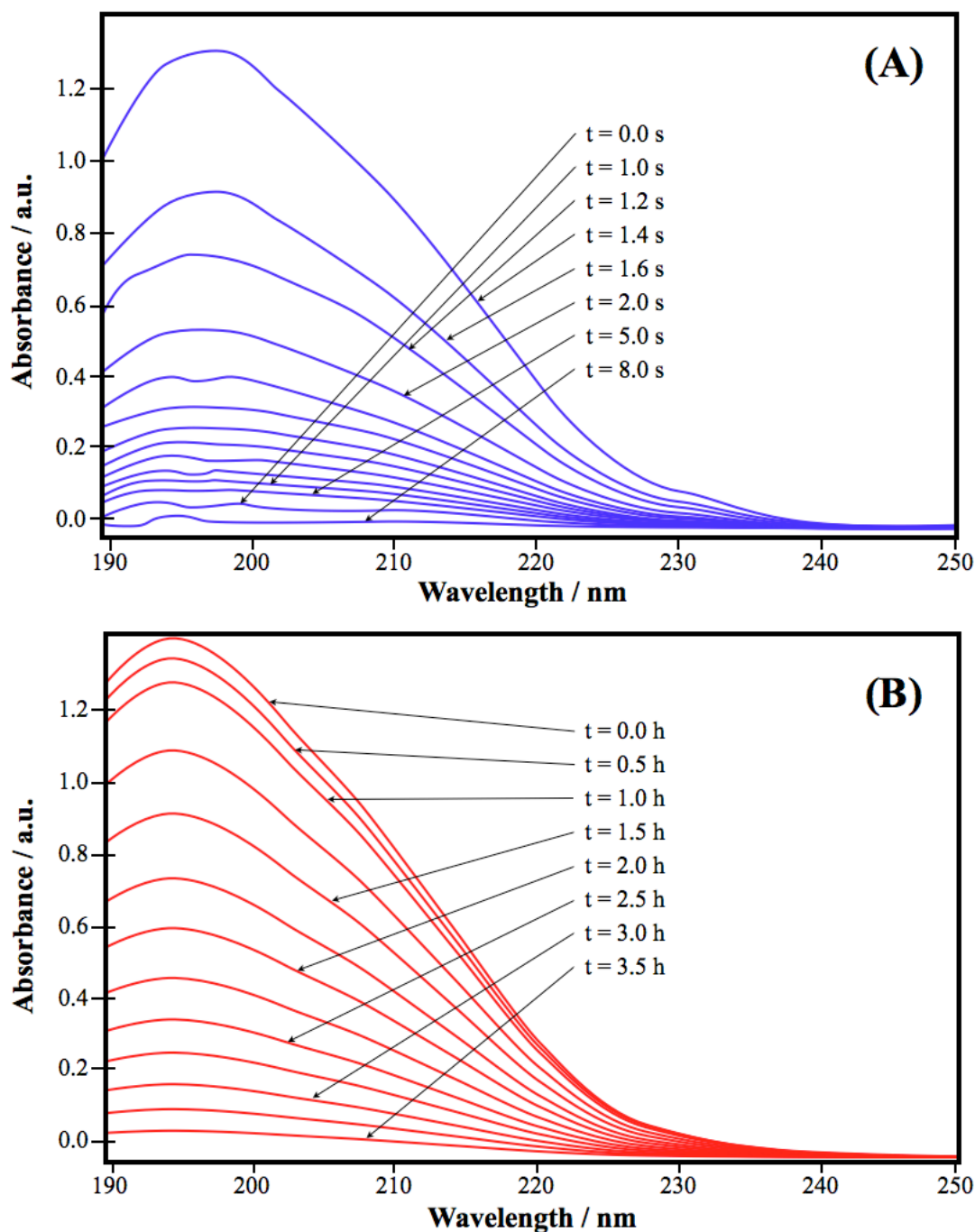


**Figure 4.2** UV-visible absorption spectra of (A)  $\text{SbCl}_3$  reference spectrum from reference 1 (collected in a micro cell) and (B)  $\text{SbCl}_3$  synthesized. The plots both show the evolution of the absorption feature at 195 nm over each samples lifetime.

sublimed the sample and carried it to the molecular beam source. A mass spectrometer (Stanford Research Systems, RGA300) was used to positively identify the sample and ensure enough stibine was surviving interaction with the stainless steel sample introduction components. The molecular beam foreline and pulsed nozzle (General Valve 9-181-900) were custom built from Sulfinert<sup>®</sup> coated stainless steel components to maximize lifetime. The concentration of the stibine in the sample was increased by slowly lowering the liquid nitrogen dewar from the collection trap and allowing it warm slightly. This concentration change was monitored by the mass spectrum in real time to confirm the presence of stibine as the experiment evolved.

Stibine HRTOF spectra were collected as described in chapter 2. Immediately after arsine data collection was complete, the instrument was expediently reconfigured to analyze stibine while experimental conditions were favorable. Ideally a high quality spectrum of this nature requires 100,000 - 200,000 shots to achieve an acceptable S/N. The laboratory conditions were favorable only long enough to collect  $\sim 21,000$  shots, and can be seen in figure 4.3. Despite the poor S/N of the distribution, some observations are still possible. Evidence of secondary photolysis (similar to that of AsH<sub>2</sub>) of SbH<sub>2</sub> can also be seen. The center-of-mass translational energy distribution is broad and the maximum is at quite low energy ( $E_{c.m.}$ ), which suggests that SbH<sub>2</sub> products were formed with significant internal excitation. This stands to reason when comparing to the photodissociation dynamics of NH<sub>3</sub>, PH<sub>3</sub> and AsH<sub>3</sub>. The SbH<sub>3</sub>  $\tilde{A} \leftarrow \tilde{X}$  transition is accompanied by a change in equilibrium geometry from  $110.5^\circ \rightarrow 91.5^\circ$  which should

result in  $\nu_2$  (umbrella mode) excitation. This out of plane bending motion may carry through the dissociation and promote  $\text{SbH}_2$   $a$ -axis rotation.

#### 4.2.2 Hydrogen Iodide (HI)

Hydrogen iodide (HI) is also an intriguing molecule of study, and likewise required care to generate and handle. Aside from the general safety considerations mentioned later in section 4.5, HI (gas) is commercially restricted reagent due to its prevalence in the illicit manufacture of methamphetamine. The only prepared sample of gaseous HI available at the time was a small lecture bottle from the laboratory of Prof. Karl Christie simply dated 1972.<sup>4</sup> The identity and purity of the sample needed to be determined to establish the cylinders usefulness. The cylinder was connected to a custom built manifold (figure 4.4) designed for preparing samples for simple absorption spectroscopy (infrared and ultraviolet) and for sample introduction to the vacuum chamber. The glassware was passivated using a similar process described for the syntheses of stibine in section 4.3.1. Samples prepared for spectroscopic analysis were diluted to 5% in argon and leaked into two 5 cm pathlength cell and analyzed using an FT-IR spectrometer (Nicolet FT50) and a UV-visible spectrometer (Varian Cary300). The IR cell windows were NaCl plates and the UV cell windows were synthetic quartz (GE024AA). The collected IR and UV spectra were compared to reference spectra and can be seen in figures 4.5 and 4.6 respectively. After confirming the identity of the hydrogen iodide by FT-IR, the relative purity of the sample was quantified by introducing standard additions of pure HI synthesized in an

## Hydrogen Iodide (HI) Synthesis Apparatus

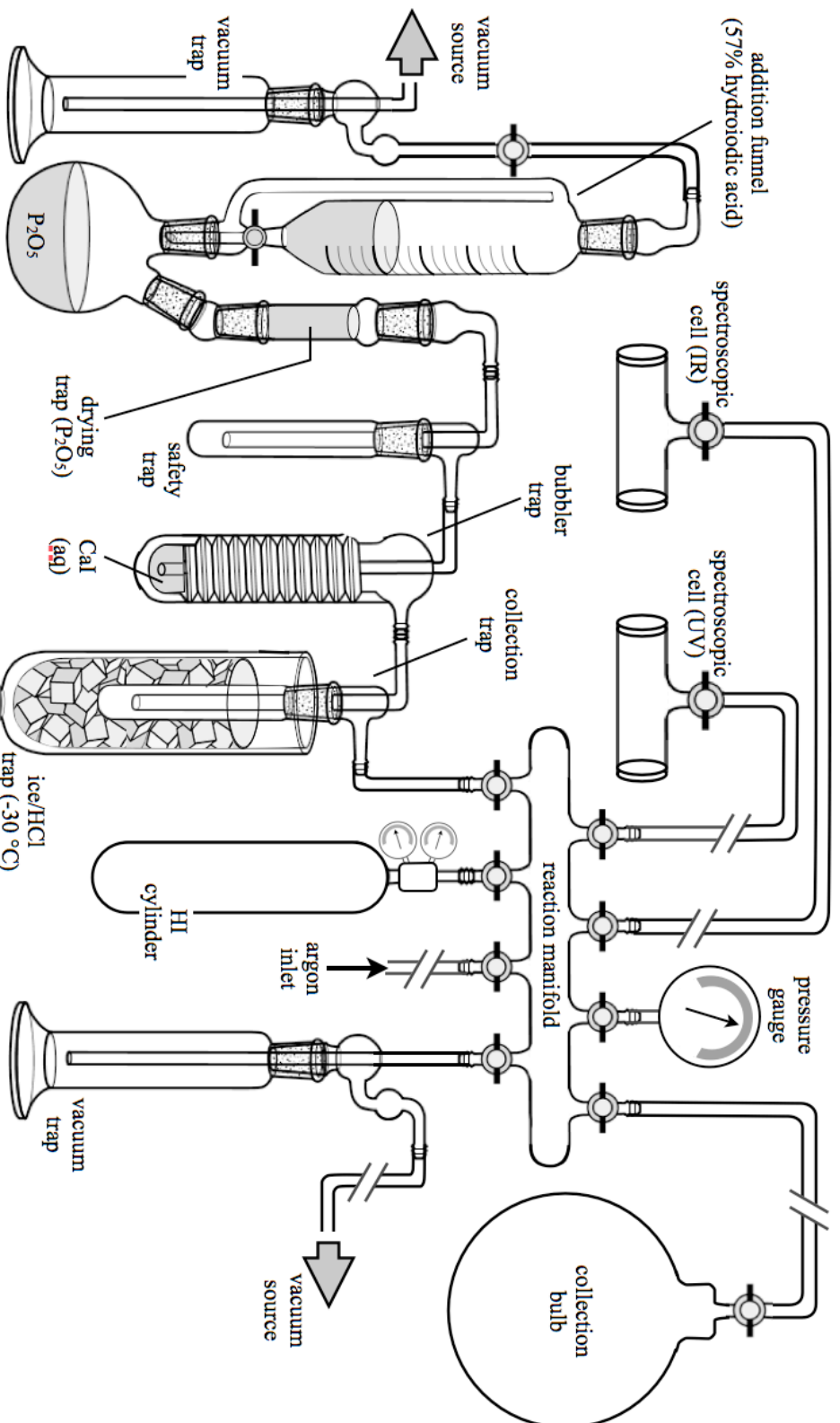


**Figure 4.4** The experimental apparatus custom built for the synthesis, dilution, spectroscopic identification and sample preparation of hydrogen iodide (HI). The apparatus was constructed mostly of glass inside a negative pressure fume hood. The synthesis apparatus was adapted from reference 5, and modified to suit scale and requirements for laboratory needs.

## Hydrogen Iodide (HI) Infrared Absorption Spectra

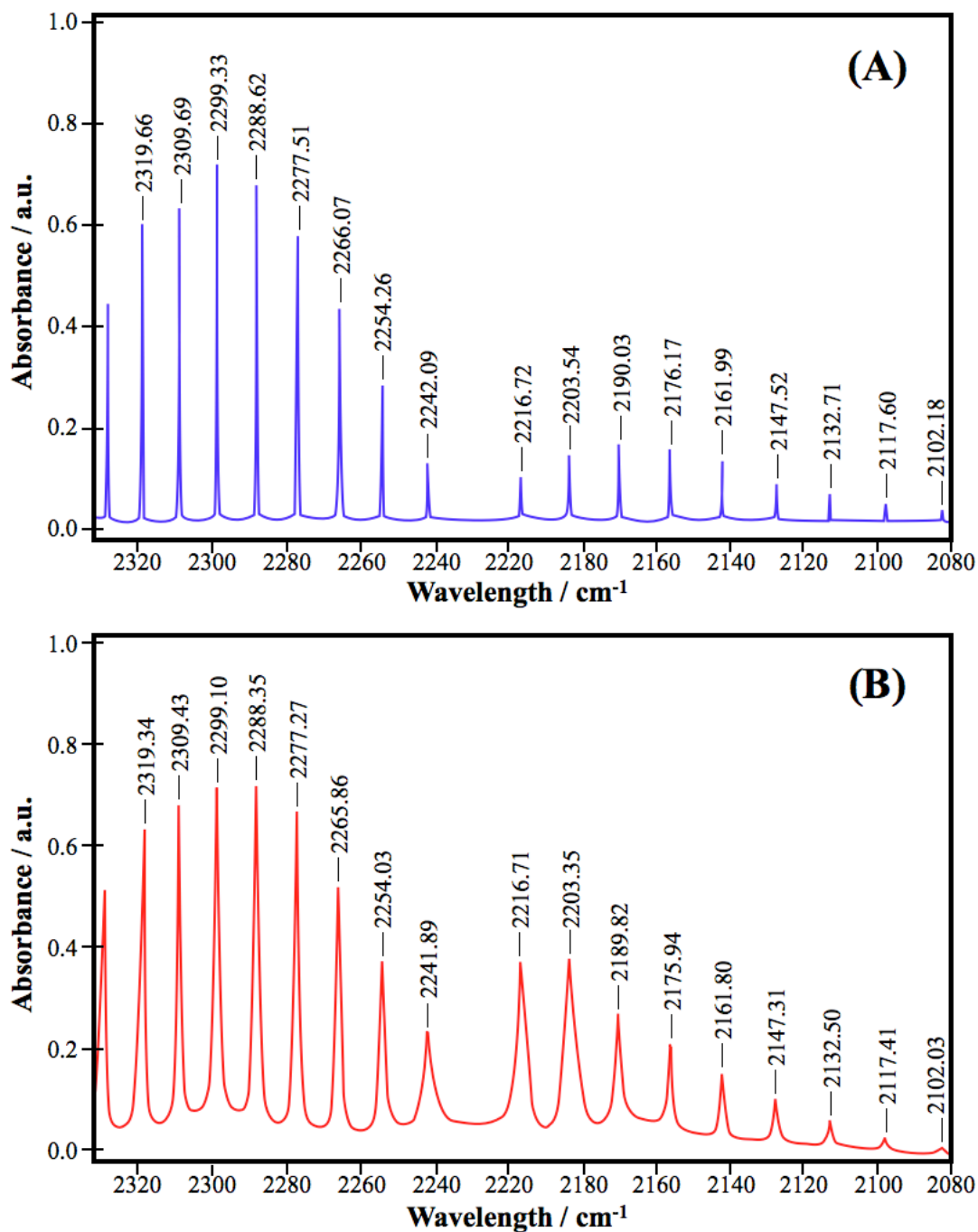


**Figure 4.5** Infrared absorption spectra in the 2000-2350  $\text{cm}^{-1}$  range of HI from (A) reference 6 and (B) synthesized product carried out in a 5 cm pathlength cell with NaCl windows in a Nicolet FT50 FT-IR spectrometer.

## Hydrogen Iodide (HI) UV-Visible Absorption Spectra

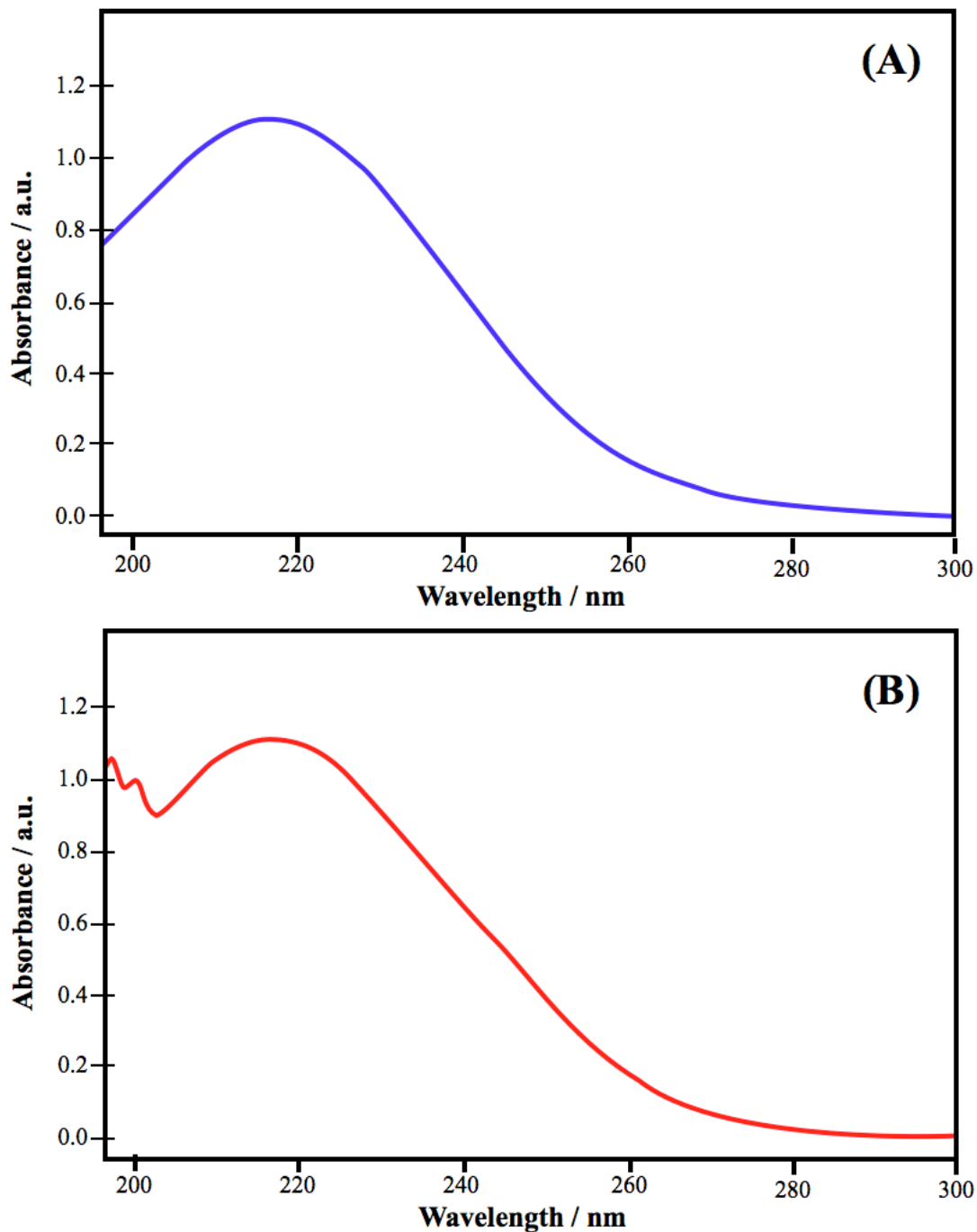


**Figure 4.6** Ultraviolet-visible absorption spectra of HI from (A) reference source 7 and (B) synthesized product carried out in a 5 cm pathlength cell with quartz windows in a Varian Cary300 spectrophotometer.

apparatus connected to the mixing manifold in figure 4.3. The synthesis of HI was consisted of an addition funnel containing a 57% (w/w) solution of hydroiodic acid connected to a reaction vessel charged with anhydrous phosphorus pentoxide ( $P_2O_5$ ).<sup>5</sup> The evolved hydrogen iodide, containing traces of iodine, water and phosphine, was purified by passage through the all glass apparatus. A glass trap filled with  $P_2O_5$  removed the mist produced by the vigorous reaction in the generating vessel. Any small amounts of phosphonium iodide present were removed by bubbling the gas through a solution of aqueous calcium iodide (CaI) maintained at 0 °C.

A glass trap filled with  $P_2O_5$  removed the mist produced by the vigorous reaction in the generating vessel. Any small amounts of iodine and phosphonium iodide present were removed by bubbling the gas through a solution of aqueous calcium iodide (CaI) maintained at 0 °C by an ice bath. A third purification to remove final traces of phosphonium iodide was achieved by use of a cold trap maintained at -30 °C by immersion in a cooling bath of crushed ice and concentrated hydrochloric acid. A saturated aqueous solution of hydrogen iodide prepared by this method produced a negative test for phosphates with ammonium molybdate. It should be noted that anhydrous hydrogen iodide in the gaseous state is easily oxidized by air and light. Because of this, it was necessary to fill the apparatus with argon for the first run, and to black out the glass apparatus to protect it from light. Despite these precautions it was necessary to discard the gas evolved from the beginning of each run.

Purity analysis of the cylinder sample was done with standard additions of pure HI (synthesized) and led to a determination of cylinder purity to be ~ 95%, which was adequate for the planned experiments.

#### **4.2.3 Diazirine (c-H<sub>2</sub>N<sub>2</sub>, 3H-diazirine)**

The adapted preparation<sup>8</sup> of cyclic diazirine was multistep requiring several days including drying and degassing periods. Production of the final product from the precursor methylenediamine sulfate salt (3CH<sub>2</sub>(NH<sub>2</sub>)<sub>2</sub>•4H<sub>2</sub>SO<sub>4</sub>) is one step and can be completed in a single day. The precursor however, required over a week to prepare with multiple steps. This was started by heating a 3:1 (w/w) formamide/paraformaldehyde mixture in a 24/40 100 mL round bottom flask to ~135 °C for 36 hours. The mixture was left to cool and crystalize for 3 days. The crystals were vacuum filtered through a 60C frit with cold methanol washes and rinsed thrice. These crystals were vacuum dried for several days and added to a 24/40 1000 mL round bottom flask in an ice/H<sub>2</sub>SO<sub>4</sub> slurry bath maintained at ~ 5 °C. A mixture of 50% H<sub>2</sub>SO<sub>4</sub> was added slowly to the crystals and allowed to cool. These crystals were refrigerated for 2 days and then vacuum filtered and rinsed thrice with cold methanol.

The synthesis of diazirine was conducted by connecting the sample flask to a glass manifold very similar in design to figure 4.1. The addition funnel containing sodium hypochlorite (NaOCl) and the reaction vessel were vacuum degassed and the ice/NaCl bath was maintained near -10 °C. The NaOCl was added drop-wise from the funnel over

## Diazirine UV-Visible Absorption Spectra

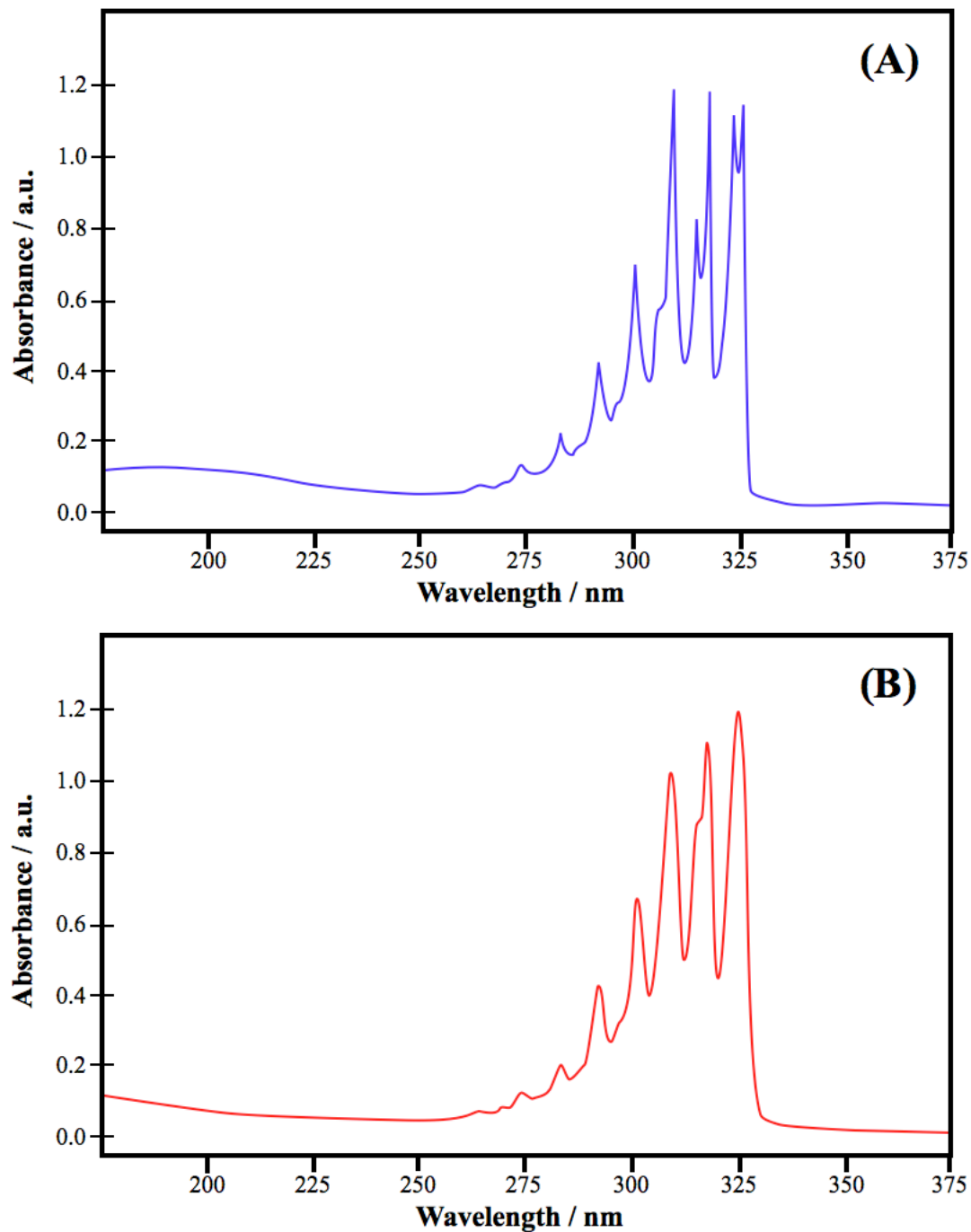


**Figure 4.7** Ultraviolet-visible absorption spectra of diazirine from (A) reference 9 and (B) synthesized product carried out in a 5 cm pathlength cell with quartz windows in a Varian Cary300 spectrophotometer.

~3 hours. A mixture of 5% diazirine was leaked into a spectroscopic cell with synthetic quartz (GE024AA) windows and an ultraviolet-visible absorption spectrum was collected. Figure 4.7 shows the collected spectrum used for identification and a reference spectrum.<sup>9</sup>

## **4.3 Design Analysis and Considerations**

### **4.3.1 Vacuum Ultraviolet Generation**

Although many design considerations must be balanced in a complicated experimental setup, there are usually particularly difficult aspects of which to be aware of. In this setup, the generation of vacuum ultraviolet (VUV) radiation from UV radiation is of particular concern. Generation of VUV radiation is achieved by non-resonant frequency tripling in a rare gas matrix. This is achieved by focusing the output of a tunable dye laser into an optical cell pressurized with ultra high purity Kr or a mixture of Kr and Ar. For tightly focused high input power densities ( $\sim 10^{12}$  W/cm<sup>2</sup>) the conversion efficiency maxes out at  $\sim 10^{-5}$ . This power limitation is caused by a dielectric breakdown in the focal point of the radiation and by intensity dependent fluctuations of the refractive index that destroy the phase matching conditions.<sup>10</sup> Reducing the input power below this threshold reduces the number density of Kr required to attain the optimal phase matching conditions, but also reduces the overall net efficiency. This can be corrected by phase matching the negatively dispersive Kr gas with a positively dispersive gas (Ar or Xe), which allows an increase in the number density of Kr and improves conversion

efficiency.<sup>11</sup> The generation efficiency curve seen in figure 4.8 was generated for an Ar/Kr mixture showing an approximate value for total pressure in the cell and proper gas ratio. Previous studies have shown that the enhancement of the conversion efficiency in this mixture can reach two orders of magnitude.<sup>12</sup>

For the generation of Lyman- $\alpha$  radiation (121.57 nm), Ar was used as the mix-in gas due primarily to its availability. This step is the limiting factor for maximization of ion or Rydberg signal even with a conversion efficiency of the VUV generation on the order of  $\sim 10^{-5}$ .<sup>13</sup> Beyond the low efficiency of the generation, the tripling process and cell require frequent attention. Adding to the difficulties is the fact that the nascent VUV radiation is not visible and must be generated in a vacuum.

The current design of the tripling cell is limiting in several ways. The method by which the gas is introduced does not allow for proper mixing, and takes some time to achieve stability. This was studied in detail to determine both the minimum time required to stabilize and the lifetime of the gas mixture at correct conditions. These studies were conducted by scanning the laser wavelength around the desired frequency and monitoring the VUV photon production with the chamber MCP detector. Each scan revealed the wavelength at which maximum efficiency was achieved. The scans were repeated at time intervals following mixing and continued for long periods of time to determine stability of the cell, as the maximum efficiency value would shift as parameters changed. It was determined that thorough mixing took a minimum of one hour and the cell was good for continual use for 12 hours reliably. This minimum start time and maximum allowable run

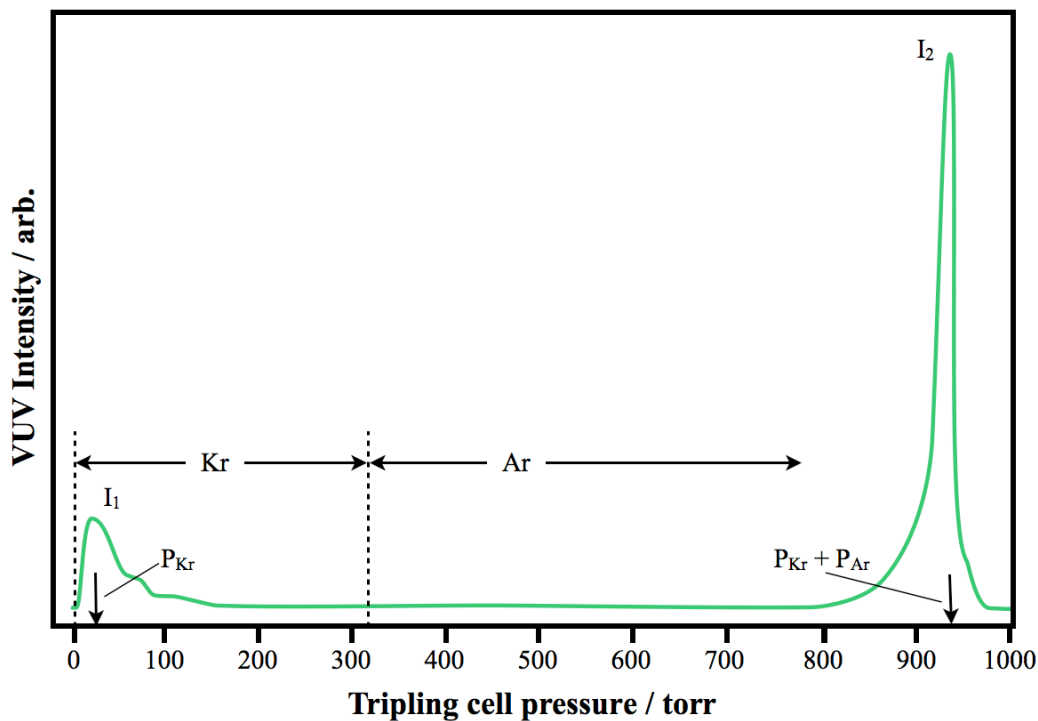


**Figure 4.8** VUV generation efficiency as a function of total cell pressure and gas ratio.  $P_{Kr}$  marks the pressure of pure Kr that produced the greatest efficiency ( $I_1$ ), and  $P_{Kr} + P_{Ar}$  marks the pressure of Kr/Ar mixture that produced the enhanced efficiency ( $I_2$ ).

time could be improved with redesign of the tripling cell incorporating a thermal mixing coil or similar device.

Determining the optimum gas mixture ratio and total operating pressure was more difficult and required many more studies. These were performed as described above, by scanning the output frequency of the tunable dye laser around the desired wavelength range and varying the individual parameters of the cell. The frequency of light generated is a function of the Ar/Kr ratio as well as the total pressure of the cell, thus multiple iterations of examining pressure ratio and total pressure were necessary to find the

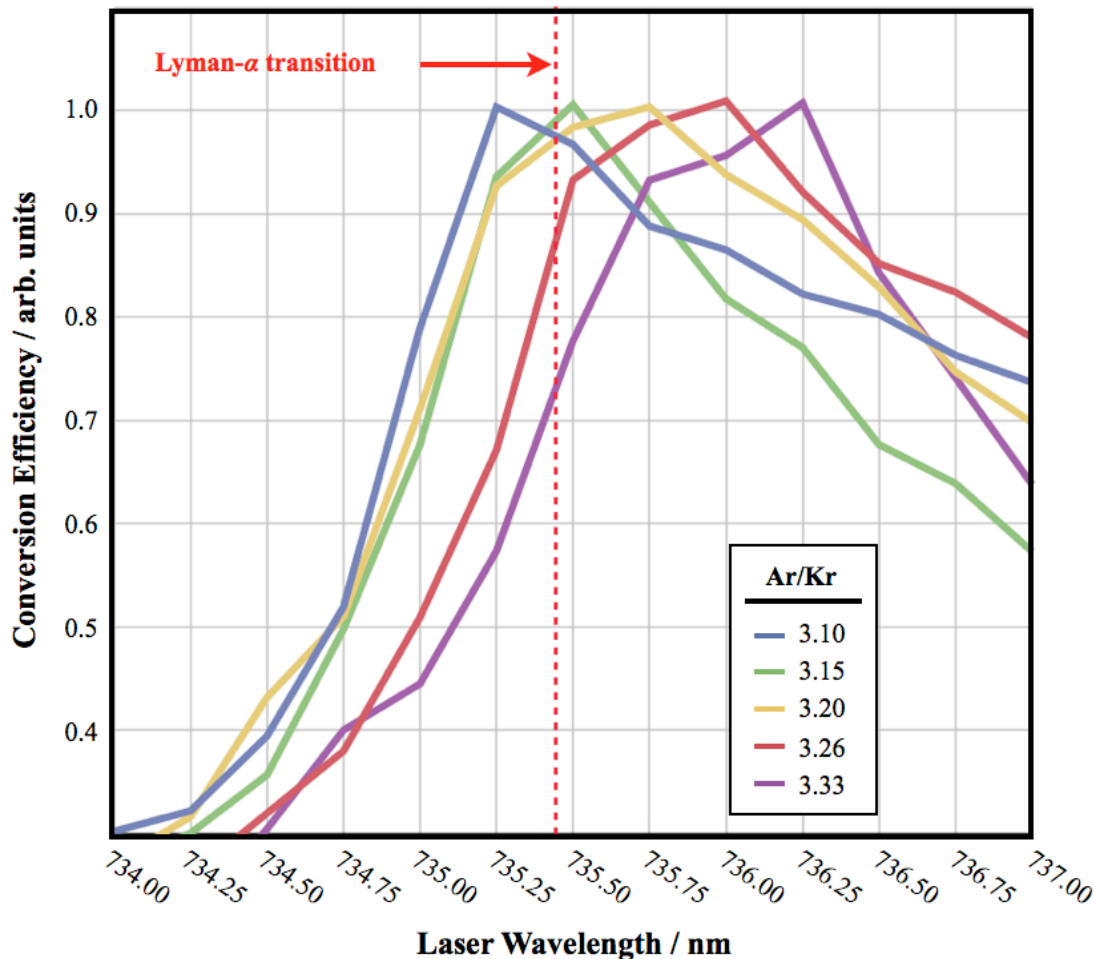


**Figure 4.9** Plot showing the frequency at maximum VUV generation efficiency for varying ratios of Ar and Kr. The laser wavelength on the x-axis represents the fundamental frequency of the dye laser (Continuum ND6000, LDS 750 laser dye). The red dashed line indicates the fundamental dye laser frequency corresponding to the Lyman- $\alpha$  transition.

optimum conditions. The gas ratio was studied by introducing a fixed quantity of Kr to the cell and adding small quantities of Ar stepwise through a ultra-low flow leak valve to change the ratio (which also changed the total pressure). This study can be seen in the plot in figure 4.9. After determining the best gas ratio from each study, the cell was pressurized with the optimized gas mixture and allowed to stand for about an hour to

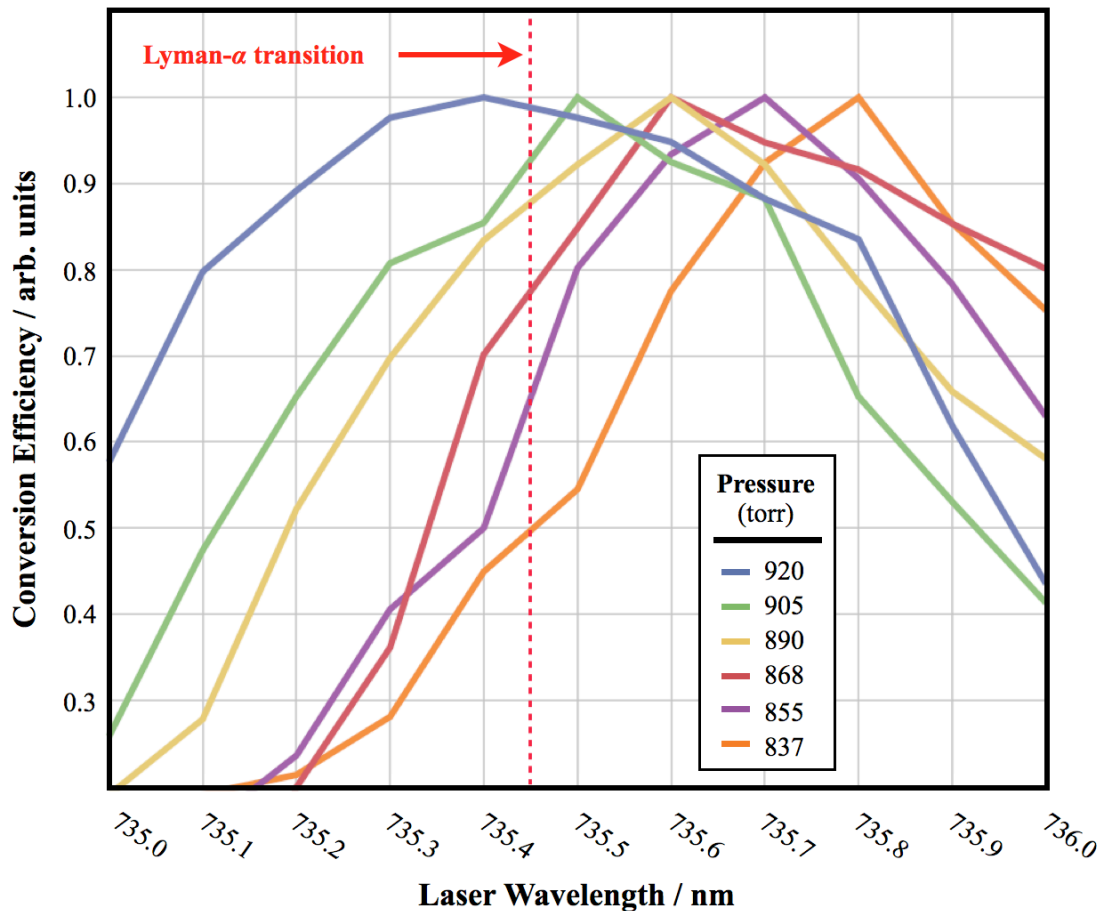


**Figure 4.10** Plot showing the frequency at maximum VUV generation efficiency for varying total pressure of Kr/Ar at the ratio determined from figure 4.9. The laser wavelength on the x-axis represents the fundamental frequency of the dye laser (Continuum ND6000, LDS 750 laser dye). The red dashed line indicates the fundamental dye laser frequency corresponding to the Lyman- $\alpha$  transition.

allow the cell to stabilize. The cell was then evacuated by small pressure increments stepwise to determine the optimum pressure at the fixed ratio. This results of this study can be seen in the plot in figure 4.10. It should be noted that these plots are the final runs from a large series of iterations to narrow in on the correct parameters.

Although determining the correct parameters allowed the tripling process to be used successfully, these studies showed that the stability of the currently designed cell was

limited to 6 - 10 hours when using significantly high power to collect spectra. This was problematic due the lengthy turn around time in preparing the cell after favorable conditions had passed. Refilling the cell with adequate recision and passivating it required nearly two hours making collection of large data sets very tedious and difficult.

#### **4.4 Safety**

Safety awareness is arguably the most important asset to any scientist in the laboratory. The laboratory in which this thesis work was conducted is dangerous on many levels. The course of these experiments has necessitated working with high pressure toxic and explosive gases, heavy metals, lacrimators, powerful reducers, carcinogens, high voltage systems and powerful ultraviolet lasers. The experiments are complex and laborious even without the great care necessary for these hazards, and is a daunting one person challenge. Throughout the course of this experimental work, and indeed for many years prior, safety has been of my utmost concern.

Photodissociation dynamics and molecular spectroscopy experiments performed with lasers in high vacuum are extraordinary tools for fundamental science. There are, however, many complexities and subtiles germane to safety inherent while conducting an experiment requiring three independent laser beams. Consideration of optical beam path requirements for lasers should be stressed among the myriad technical details in the design of a high vacuum chamber apparatus. Operating multiple high powered ultraviolet lasers traversing the lab space at eye level (some with focal points directly in

walking paths) establishes a significant personal hazard and requires vigilant safety practice and good laboratory procedures to maintain a safe working environment. Many laboratories are designed to have beam paths elevated above head level or near waist level, and facilitate a much safer working environment.

Several syntheses were performed which required specific individual safety measures. Stibine is a colorless gas at room temperature and has an offensive odor similar to hydrogen sulfide. It is an unstable flammable gas and is highly toxic with an OSHA PEL of 50 ppb in air, and it plates out on glass as an elemental metal. Both the synthesis ( $\text{SbH}_3$  synthesis is discussed further in section 4.2.1) and sample introduction of stibine in the laboratory require rigorous procedures for safe handling. A blast-proof, negative air pressure cabinet was purpose built for housing the glass sample bulb, as stibine decomposes upon contact with metal. This also required the use of Tygon<sup>®</sup> tubing in as much of the foreline as possible and special Sulfinert<sup>®</sup> coated stainless steel coated molecular beam nozzle components. A respirator was required at all times as the exhaust ventilation in the laboratory was often inadequate. Careful control of foreline pressure and laboratory conditions for sample safety necessitated full-time attention as did operation of the all laboratory equipment necessary to perform the experiment, making this a two person experiment at minimum.

Many of the gases used ( $\text{SbH}_3$ ,  $\text{AsH}_3$ , diazirine) were unstable and reacted violently to decompose into flammable and toxic products. Whether the gases were thermally labile or were autocatalytically decomposed, extreme caution was necessary for safe

handling. Aside from collection traps and bulbs of these gases requiring blast-proof and well ventilated containment structures, care had to be taken in the case of accidental gas leaks in the system plumbing. A gas leak could mean an inhalation, explosion or contact poisoning hazard, all of which had to be anticipated and prepared for. Much of the gas sample handling was done in multiple layers of personal protective equipment (PPE), making the already tedious work extremely difficult and time consuming.

Hydrogen iodide (HI) was synthesized as a standard to check available gas source purity (HI synthesis is discussed further in section 4.2.2). Hydrogen iodide is a colorless gas at room temperature and is highly corrosive (reducer) and toxic by inhalation (lacrimator), with an OSHA PEL of 50 ppb in air.

Even with commercially available gas samples, special considerations must be made for sample introduction. Several gases used in this laboratory (NO, HCl, HBr, HI) were extremely corrosive, even at purities as low as 5%, requiring high quality metal components be used and further necessitated frequent component replacement and maintenance. Maintaining concentration control of these gases was crucial as concentrated samples can easily destroy detectors and pressure sensors, as well as seals and gaskets required to maintain a high vacuum. These corrosive gases also present a challenge for the vacuum pumping system, requiring extensive abatement in the form of aggressive cooling of diffusion pumps and multi-stage cryo traps guarding the mechanical roughing pumps. Failure to properly abate the corrosive species in the pumping stream can lead to not only equipment failure and destruction, but also

accidental introduction of the corrosive gases into the laboratory. These corrosive gases can easily become trapped in dead spaces in manifolds and regulators, and require goggles and a respirator to safely handle.

It cannot be stressed enough that the time, manpower and financial considerations of adequate safety systems and equipment cannot be regarded as of minor importance. As a one person laboratory for many years, an unwillingness to compromise safety was at the root of many laboratory failures due to time constraints. More than once did the funding period for a project elapse before the safety and the experimental procedures both necessary for success of the project could be completed. While frustrating, and at many times tempting to forgo the rigorous safety procedures in order to achieve the experimental success so greatly strived for, regard for personal safety could never be compromised.

## 4.5 Chapter 4 References

1. Bellama, J.; MacDiarmid, A.G. *Inorg. Chem.* **1968**, *7*, 2070.
2. Laboratory Notebook; *WPS 002-067*. 19 Apr 2012.
3. Sans, J.; Gallarta, F.; Glaban, J.; *Anal. Chem.* **1988**, *330*, 510.
4. Laboratory Notebook; *WPS 002-108*. 27 Jul 2010.
5. Dillon, R.T.; Young, W.G. *J. Am. Chem. Soc.* **1929**, *51*, 2389.
6. Nielsen, A.H.; Nielsen, H.H. *Phys. Rev.* **1935**, *47*, 585.
7. Campuzano-Jost, P.; Crowley, J.N. *J. Phys. Chem. A.* **1999**, *103*, 2712.
8. Church, R.F.R.; Weiss, M.J. *J. Org. Chem.* **1970**, *35*, 2465.
9. Laufer, A.H.; Okabe, H. *J. Chem. Phys.* **1972**, *76*, 3504.
10. Hilbig, R.; Wallenstein, R. *IEEE J. Quant. Electron.* **1981**, *8*, 1556.
11. Mahon, R.; McIlrath, T.; Myerscough, V.; Koopman, D. *IEEE J. Quant. Electron.* **1979**, *6*, 444.
12. Wallenstein, R. *Opt. Commun.* **1980**, *33*, 119.
13. Mahon, R.; Yiu, Y.M. *Opt. Lett.* **1980**, *5*, 279.
14. Langer, H.; Puell, H.; Röhr, H. *Opt. Commun.* **1980**, *34*, 137.

# Chapter 5

## Future Directions

### 5.1 Introduction

The previous chapters discussed the photodissociation dynamics of group-V hydrides as model systems for non-adiabatic dynamics. Further experimental and theoretical exploration of the remainder of these molecules would be of great use to the semiconductor and materials industries, as well as potentially provide greater insights into the fundamental science of non-adiabatic dissociation dynamics.

### 5.2 AsH<sub>2</sub>

As the discussion in chapter 3 demonstrated, the 193 nm photodissociation dynamics of arsine are quite complicated owing to the wealth of reaction channels and secondary photodissociation of AsH<sub>2</sub>. The arsine HRTOF distribution shows superimposed structure below the minimal TOF for primary photolysis that suggests that AsH<sub>2</sub> products are formed with significant internal excitation. Clarification of these states could be achieved by monitoring the jet-cooled photodissociation of AsH<sub>2</sub> without contribution from AsH<sub>3</sub> photodissociation. This would require some modification to the present experimental setup. Figure 5.1 shows the modification necessary to photodissociate AsH<sub>3</sub> in a quartz expansion tube prior to entry into the interaction region.

The nascent AsH<sub>2</sub> would then be dissociated using radiation not absorbed by residual the AsH<sub>3</sub>.

The ground state electron configuration of AsH<sub>2</sub> is  $\dots(b_2)^2 (a_1)^2 (b_1)^1$ .<sup>1</sup> Promotion of an electron from the a<sub>1</sub> orbital to the b<sub>1</sub> orbital results in the  $\tilde{A}^2A_1 \leftarrow \tilde{X}^2B_1$  transition and leads to an increase in bond angle from 90.4° → 123.0°. AsH<sub>2</sub> ( $\tilde{X}^2B_1$ ) and AsH<sub>2</sub> ( $\tilde{A}^2A_1$ ) form a Renner-Teller pair, thus both correlate to a  $^2II$  state in linear geometry. Some experimental studies have shown that AsH<sub>2</sub>( $\tilde{A}$ ) vibrational states are predissociative due to spin-orbit interactions.<sup>2,3</sup>

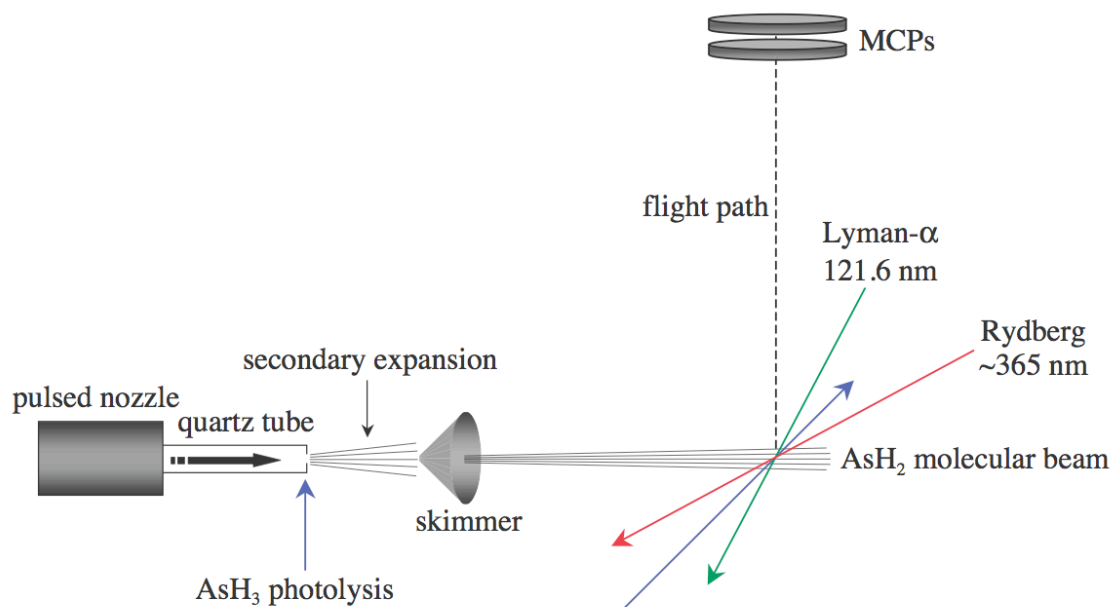


**Figure 5.1** Schematic illustration of experimental modifications necessary to study the photodissociation dynamics of AsH<sub>2</sub>. The AsH<sub>3</sub> photolysis would enter through chamber windows already in place.

### 5.3 SbH<sub>3</sub> and SbH<sub>2</sub>

Studying the photodissociation dynamics of stibine is the next logical step in gaining a better understanding of the photochemistry of the group-V hydrides. As detailed in chapter 4, stibine is not a user friendly molecule as the lack of experimental research available reflects. Theoretical complications also hinder the advancement of research due to the large number of electrons and relativistic effects. Stibine is of interest, however, to the materials industry as it is used in the manufacture of semiconductor and optoelectronic devices.<sup>4,5,6,7</sup>

The group-V hydrides NH<sub>3</sub>( $\tilde{X}$ ), PH<sub>3</sub>( $\tilde{X}$ ), AsH<sub>3</sub>( $\tilde{X}$ ) and SbH<sub>3</sub>( $\tilde{X}$ ) share the electron configuration ...( $a_1$ )<sup>2</sup> ( $e$ )<sup>4</sup> ( $a_1$ )<sup>2</sup> and the  $\tilde{A} \leftarrow \tilde{X}$  transition involve promotion of the highest occupied lone pair electron to a Rydberg  $a_1$  orbital.<sup>6,7,8</sup> The  $\tilde{A} \leftarrow \tilde{X}$  absorption band of NH<sub>3</sub> shows a progression in the  $\nu_2$  umbrella mode which reflects a pyramidal-to-planar geometry change, yet the  $\tilde{A} \leftarrow \tilde{X}$  absorption spectra for PH<sub>3</sub>, AsH<sub>3</sub> and SbH<sub>3</sub> show broad continuous absorption features.<sup>10</sup> It was found these absorption spectra that for NH<sub>3</sub>  $\nu_2' \sim \nu_2''$ , whereas  $\nu_2' \sim \nu_2'' / 2$  for PH<sub>3</sub>, AsH<sub>3</sub> and SbH<sub>3</sub>. This has led to the suggestion that the  $\tilde{A}$  states of PH<sub>3</sub>, AsH<sub>3</sub> and SbH<sub>3</sub> are pyramidal with transitions terminating on vibrational levels above the inversion barrier.<sup>11</sup> Given that the ground states of PH<sub>3</sub><sup>+</sup> (114°), AsH<sub>3</sub><sup>+</sup> (112°) and SbH<sub>3</sub><sup>+</sup> (110.5°) are non-planar,<sup>12,13,14</sup> it is not unreasonable to assume that PH<sub>3</sub> ( $\tilde{A}$ ), AsH<sub>3</sub> ( $\tilde{A}$ ) and SbH<sub>3</sub> ( $\tilde{A}$ ) are also non-planar. The potential energy surfaces of PH<sub>3</sub> ( $\tilde{A}$ ), AsH<sub>3</sub> ( $\tilde{A}$ ) and SbH<sub>3</sub> ( $\tilde{A}$ ) are also qualitative similar.

The photodissociation dynamics of PH<sub>3</sub> and AsH<sub>3</sub> mirror those of NH<sub>3</sub> with a few

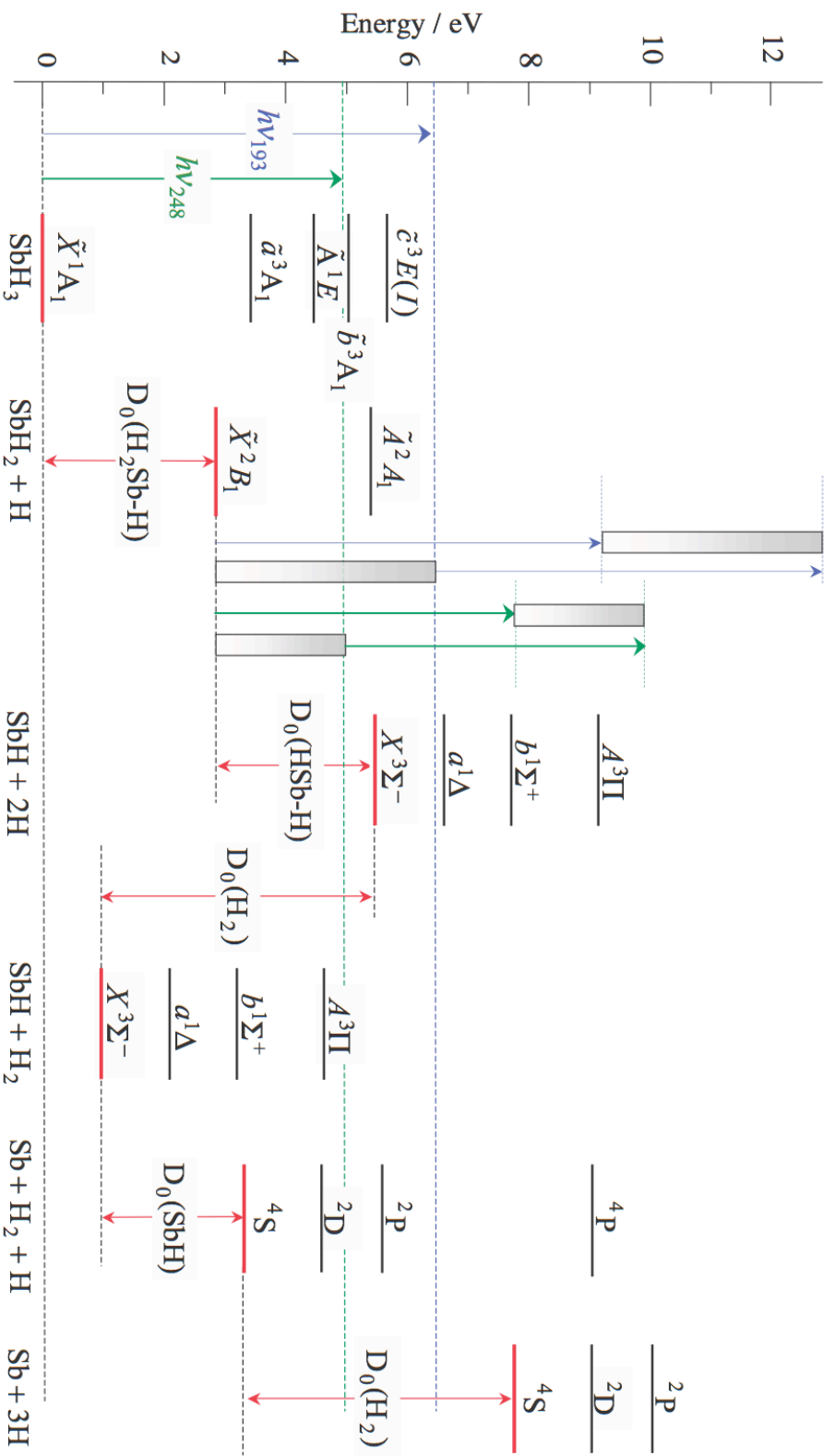


**Figure 5.2.** Energy level diagram for the 193.3 and 248 nm photolysis of  $\text{SbH}_3$ . The 193 nm photon energy is significantly greater than the  $\text{SbH}_3$  bond dissociation energy. The product species that can undergo secondary photodissociation are also shown. The shaded rectangles indicate possible energy ranges for internally excited  $\text{SbH}_2$ . The spin-orbit  $\text{SbH}$  states are not shown here.

notable differences. HRTOF spectroscopy has been used to investigate the UV photolysis of PH<sub>3</sub> and AsH<sub>3</sub>. Structured translational energy distributions indicate that the internal excitation of PH<sub>2</sub> ( $\tilde{X}$ ) and AsH<sub>2</sub> ( $\tilde{X}$ ) accounts for ~62% and ~64% of the available energy [*i.e.*  $h\nu - D_0(H_2P-H / H_2As-H)$ ], respectively. The PH<sub>2</sub> and AsH<sub>2</sub> products are formed with significant *a*-axis rotation, as well as bending excitation.<sup>15</sup> The change in bond angle from PH<sub>3</sub> ( $\tilde{A}$ ) to PH<sub>2</sub> ( $\tilde{X}$ ) and AsH<sub>3</sub> ( $\tilde{X}$ ) to AsH<sub>2</sub> ( $\tilde{X}$ ) is suggested as a plausible source for the product vibrational excitation.<sup>15</sup>

It is reasonable to assume that the photodissociation dynamics of SbH<sub>3</sub>( $\tilde{A}$ ) will exhibit marked similarities with PH<sub>3</sub> and AsH<sub>3</sub>. It should be noted that calculations of the lowest excited singlet surfaces indicate that SbH<sub>3</sub> ( $\tilde{A}$ ) and AsH<sub>3</sub>( $\tilde{A}$ ) have *E* symmetry, which differs from the lowest excited singlets of NH<sub>3</sub> and PH<sub>3</sub>.<sup>6,8,16</sup> An SbH<sub>2</sub>  $\tilde{A} \rightarrow \tilde{X}$  emission spectrum has been recorded by Ni *et. al.* following the 193.3 nm photolysis of SbH<sub>3</sub>.<sup>17</sup> Their results indicated that SbH<sub>3</sub>( $\tilde{A} \ ^2A_1$ ) was formed in highly-excited vibrational states. Emission from nascent Sb atoms ( $6s \rightarrow 5p$ ) was also observed using 193.3 nm and 248 nm photolysis radiation. Photolysis of SbH<sub>2</sub> was suggested as a possible mechanism for the Sb emission. It is interesting to note that the 248 nm photolysis of AsH<sub>3</sub> yielded no detectable fluorescence.<sup>18</sup> Figure 5.2 shows the possible products from primary and secondary photolysis processes. Unfortunately, results from the HRTOF experiment were inconclusive.

## 5.4 BiH<sub>3</sub> and BiH<sub>2</sub>

Bismuthine, (BiH<sub>3</sub>), the final member of the group-V hydrides. BiH<sub>3</sub> ( $\tilde{X}^1A_1$ ) has the smallest bond angle (90.3°) compared with its lighter group-V relatives and is a near-spherical oblate symmetric top ( $B_0 \sim C_0$ ).<sup>6,19,20</sup> The severe instability of BiH<sub>3</sub> and the difficulty associated with the synthesis has frustrated experimental research. Prior to 2002, no one was able to successfully replicate the BiH<sub>3</sub> synthesis first reported by E. Amberger in 1961.<sup>21</sup> The bismuth hydrides, especially BiH, have garnered theoretical interest due to the large role played by relativistic and spin-orbit effects. It is probable that these effects dramatically influence the photodissociation dynamics of BiH<sub>3</sub>. Assuming the ability to repeat the Amberger synthesis, the investigation of BiH<sub>3</sub> *via* HRTOF spectroscopy should provide valuable insight as to how relativistic effects influence photodissociation dynamics. In keeping with recent studies on AsH<sub>3</sub> and SbH<sub>3</sub>, 193.3 and 248 nm radiations are reasonable choices. The photon energy at both 193.3 nm and 248 nm has sufficient energy to break two H-bonds. Figure 5.3 presents an energy level diagram of possible BiH<sub>n</sub> products. The photodissociation dynamics of BiH<sub>2</sub> could also be studied utilizing the experimental set-up described to study AsH<sub>2</sub> in section 5.2.

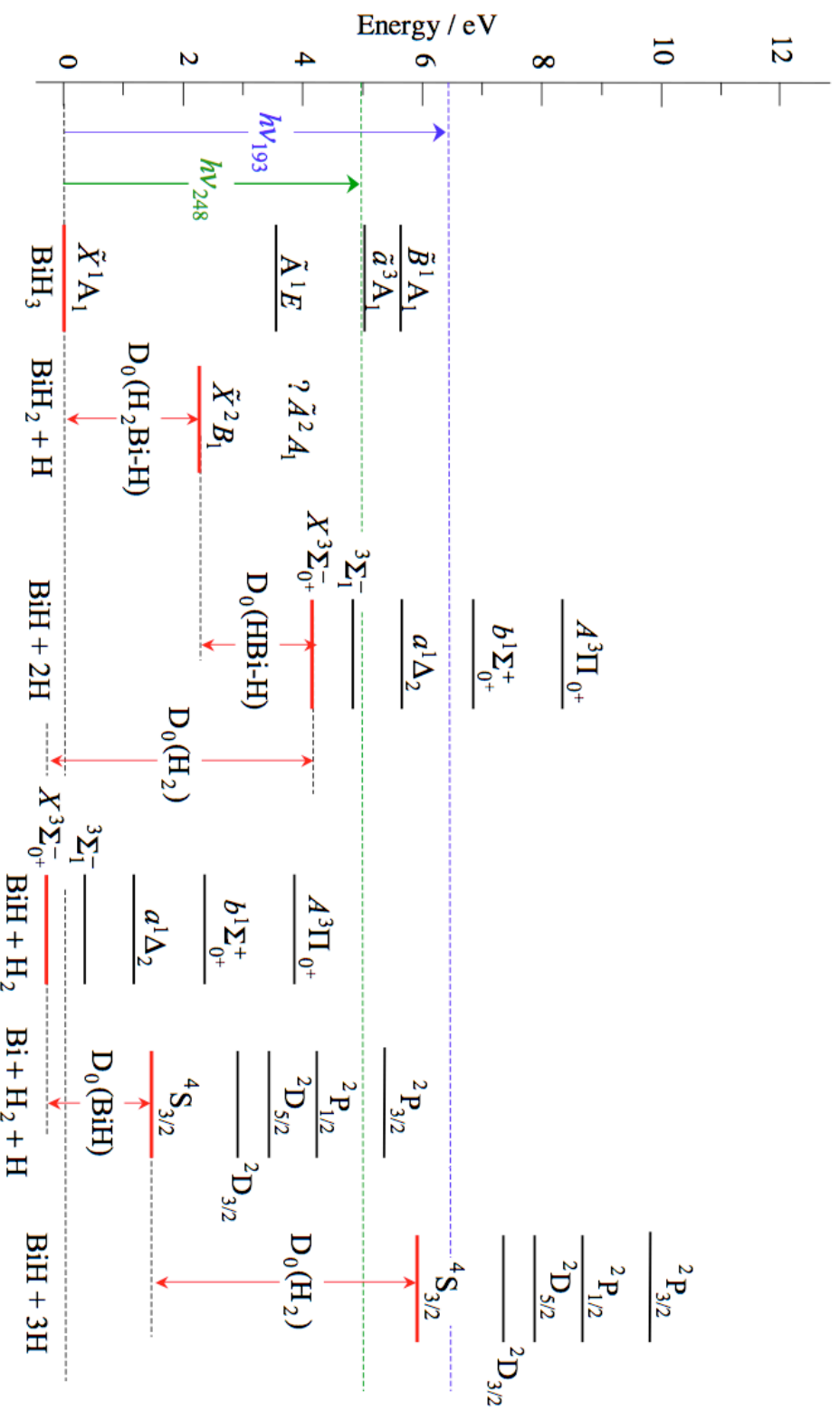


**Figure 5.3.** Energy level diagram for the 193.3 and 248 nm photolysis of  $\text{BiH}_3$ . It should be noted that spin-orbit coupling splits the electronic states of  $\text{BiH}$  into numerous relativistic states. Only a few  $\text{BiH}$  spin-orbit states are <sup>6:22-24</sup>

## 5.5 Chapter 5 References

1. Alekseyev, A.; Buenker, R. J.; Liebermann, H.-P.; Hirsch, G. *J. Chem. Phys.* **1994**, *100*, 2989.
2. He, S.-G.; Clouthier, D. J. *J. Chem. Phys.* **2007**, *126*, 154312.
3. Dixon, R. N.; Duxbury, G.; Lamberton, H. M. *Proc. R. Soc. London Ser. A* **1968**, *05*, 271
4. Greenswood, N. N.; Earnshaw, A. *Chemistry of the Elements*; Butterworth-Heinemann: Oxford, 1997.
5. Herman, I. P. *Chem. Rev.* **1989**, *89*, 1323.
6. Dai, D.; Balasubramanian, K. *J. Chem. Phys.* **1990**, *93*, 1837.
7. Ruscic, B.; Berkowitz, J. *J. Chem. Phys.* **1993**, *99*, 5840.
8. Biesner, J.; Schneider, L.; Schmeer, J.; Ahlers, G.; Xie, X.; Welge, K. H.; Ashfold, M. N. R.; Dixon, R. N. *J. Chem. Phys.* **1988**, *88*, 3607.
9. Lambert, I. R.; Morley, G. P.; Mordaunt, D. H.; Ashfold, M. N. R.; Dixon, R. N. *Can. J. Chem.* **1994**, *72*, 977.
10. Vaida, V.; McCarthy, M. I.; Engelking, P. C.; Rosmus, P.; Werner, H. J.; Botshwina, P. *J. Chem. Phys.* **1987**, *86*, 6669.
11. Humphries, C. M.; Walsh, A. D.; Warsop, P. A. *Discuss. Faraday Soc.* **1963**, *35*, 148.
12. Maripuu, R.; Reineck, I.; Ågren, H.; Nian-Zu, W.; Rong, J. M.; Veenhuizen, H.; Al-Shamma, S. H.; Karlsson, L.; Siegbahn, K. *Mol. Phys.* **1983**, *48*, 1255.
13. Berkowitz, J. *J. Chem. Phys.* **1988**, *89*, 7065.
14. Potts, A. W.; Price, W. C. *Proc. R. Soc. London, Ser. A* **1972**, *326*, 181.
15. Smith-Freeman, L. A.; Schroeder, W. P.; Wittig, C. *J. Phys. Chem. A* **2009**, *113*, 2158.

16. Müller, J.; Ågren, H. *J. Chem. Phys.* **1982**, *76*, 5060.
17. Ni, T.; Yu, S.; Ma, X; Kong, F. *Chem. Phys. Lett.* **1986**, *128*, 270.
18. Ni, T.; Lu, Q.; Ma, X; Yu, S.; Kong, F. *Chem. Phys. Lett.* **1986**, *126*, 417.
19. Jerzembeck, W.; Bürger, H.; Constantin, F. L.; Margulès, L.; Demaison, J. *Mol. Spectrosc.* **2004**, *226*, 24.
20. Jerzembeck, W.; Bürger, H.; Constantin, F. L.; Margulès, L.; Demaison,; Breidung, W. T. *Angew. Chem. Int.* **2002**, *41*, 2550.
21. Amberger, E. *Chem. Ber.* **1961**, *94*, 1447.
22. Alekseyev, A.; Buenker, R. J.; Liebermann, H.-P.; Hirsch, G. *J. Chem. Phys.* **1994**, *100*, 2989.
23. Balasubramanian, K. *J. Mol. Spectrosc.* **1989**, *115*, 258.
24. Moore, C. E. *Atomic Energy Levels*: National Bureau of Standards: Washington, DC, 1971.

## Bibliography

- Alekseyev, A.; Buenker, R. J.; Liebermann, H.-P.; Hirsch, G. *J. Chem. Phys.* **1994**, 100, 2989.
- Amberger, E. *Chem. Ber.* **1961**, 94, 1447.
- Anderson, C.D. *Physical Review.* **1933**, 43, 491.
- Aoyagi, Y.; Kanazawa, M.; Doi, A.; Iwai, S.; Namba, S. *J. Appl. Phys.* **1986**, 60, 3131.
- Aren, M.; Richter, W. *J. Chem. Phys.* **1990**, 93, 7094.
- Ashfold, M. N. R.; Baggott, J. E. *Molecular Photodissociation Dynamics*; Royal Society of Chemistry: Piccadilly, 1987.
- Ashfold, M. N. R.; Lambert, I. R.; Mordaunt, D. H.; Morley, G. P.; Western, C. M. *J. Phys. Chem.* **1992**, 96, 2938.
- Balasubramanian, K. *Relativistic Effects in Chemistry, Part A*; John Wiley & Sons, Inc: New York, 1997.
- Balasubramanian, K. *Relativistic Effects in Chemistry, Part B*; John Wiley & Sons, Inc.: New York, 1997.
- Balasubramanian, K. *J. Mol. Spectrosc.* **1989**, 115, 258.
- Balasubramanian, K.; Nannegari, V. *J. Mol. Spectrosc.* **1989**, 138, 482.
- Barysz, M.; Ishikawa, Y. *Relativistic Methods for Chemists*. Springer Science & BusinessMedia: New York, 2010
- Baugh, D.; Koplitz, B.; Xu, Z.; Wittig, C. *J. Chem. Phys.* **1988**, 88, 879.
- Bellama, J.; MacDiarmid, A.G. *Inorg. Chem.* **1968**, 7, 2070.
- Berkowitz, J. *J. Chem. Phys.* **1988**, 89, 7065.
- Berthou, J. M.; Pascat, B.; Guenebaut, H.; Ramsay, D. A. *Can. J. Phys.* **1972**, 50, 2265.

- Biesner, J.; Schnieder, L.; Ahlers, G.; Xie, X.; Welge, K. H.; Ashfold, M. N. R.; Dixon, R. N. *J. Chem. Phys.* **1989**, *91*, 2901.
- Biesner, J.; Schnieder, L.; Schmeer, J.; Ahlers, G.; Xie, X.; Welge, K. H.; Ashfold, M. N. R.; Dixon, R. N. *J. Chem. Phys.* **1988**, *88*, 3607.
- Binning Jr., R. C.; Curtiss, L. A. *J. Chem. Phys.* **1990**, *92*, 1860.
- Born, M; Oppenheimer, J.R. *Annalen der Physik.* **1927**, *389*, 457.
- Buetel, M.; Setzer, K. D.; Shestakov, O.; Fink, E. H. *J. Mol. Spectrosc.* **1996**, *178*, 165.
- Butler, L. J.; Neumark, D. M. *J. Phys. Chem.* **1996**, *100*, 12801.
- Campuzano-Jost, P.; Crowley, J.N. *J. Phys. Chem. A.* **1999**, *103*, 2712.
- Christiansen, P. A.; Ermler, W. C.; Pitzer, K. S. *Annu. Rev. Phys. Chem.* **1985**, *36*, 407.
- Church, R.F.R.; Weiss, M.J. *J. Org. Chem.* **1970**, *35*, 2465.
- Dai, D.; Balasubramanian, K. *J. Chem. Phys.* **1990**, *93*, 1837.
- Dillon, R.T.; Young, W.G. *J. Am. Chem. Soc.* **1929**, *51*, 2389.
- Dirac, P.A.M. *Proceedings of the Royal Society A: Mathematical, Physical and Engineering Sciences.* **1928**, *177*, 778.
- Dixon, R. N.; Duxbury, G.; Lamberton, H. M. *Proc. R. Soc. London Ser. A* **1968**, *05*, 271
- Dixon, R. N.; Lamberton, H. M. *J. Mol. Spectrosc.* **1968**, *25*, 12.
- Donnelly, V. M.; Karlicek, R. F. *J. Appl. Phys.* **1982**, *53*, 6399.
- Gallagher, T. F. *Rydberg Atoms*; Cambridge Univ. Press: Cambridge, 1994. 4142
- Greenswood, N. N.; Earnshaw, A. *Chemistry of the Elements*; Butterworth-Heinemann: Oxford, 1997.
- Greiner, W. *Relativistic Quantum Mechanics*; Springer: New York, 1997.

- Harvey, Jeremy N. *Phys. Chem. Chem. Phys.* **2006**, *9*, 331.
- Hause, M. L.; Yoon, Y. H.; Crim, F. F. *J. Chem. Phys.* **2006**, *125*, 174309.
- He, S.-G.; Clouthier, D. J. *J. Chem. Phys.* **2007**, *126*, 154312.
- Herman, I. P. *Chem. Rev.* **1989**, *89*, 1323.
- Hilbig, R.; Wallenstein, R. *IEEE J. Quant. Electron.* **1981**, *8*, 1556.
- Humphries, C. M.; Walsh, A. D.; Warsop, P. A. *Discuss. Faraday Soc.* **1963**, *35*, 148.
- Jerzembeck, W.; Bürger, H.; Constantin, F. L.; Margulès, L.; Demaison, J. *Mol. Spectrosc.* **2004**, *226*, 24.
- Jerzembeck, W.; Bürger, H.; Constantin, F. L.; Margulès, L.; Demaison, J.; Breidung, W. T. *Angew. Chem. Int.* **2002**, *41*, 2550.
- Kassab, E.; Gleghorn, J. T.; Evleth, E. M. *J. Am. Chem. Soc.* **1983**, *105*, 1746.
- Koplitz, B.; Xu, Z.; Wittig, C. *Appl. Phys. Lett.* **1988**, *52*, 860.
- Kukimoto, H.; Ban, Y.; Komatsu, H.; Takechi, M.; Ishizaki, M. *J. Cryst. Growth* **1986**, *77*, 223.
- Langer, H.; Puell, H.; Röhr, H. *Opt. Commun.* **1980**, *34*, 137.
- Laufer, A.H.; Okabe, H. *J. Chem. Phys.* **1972**, *76*, 3504.
- Lambert, I. R.; Morley, G. P.; Mordaunt, D. H.; Ashfold, M. N. R.; Dixon, R. N. *Can. J. Chem.* **1994**, *72*, 977.
- Lee, Y.T.; McDonald, J. D.; Lebreton, P. R.; Herschbach, D. R. *Rev. Sci. Instrum.* **1969**, *40*, 1402.
- Loomis, R. A.; Reid, J. P.; Leone, S. J. *J. Chem. Phys.* **2000**, *112*, 658.
- Mahon, R.; McIlrath, T.; Myerscough, V.; Koopman, D. *IEEE J. Quant. Electron.* **1979**, *6*, 444.

- Mahon, R.; Yiu, Y.M. *Opt. Lett.* **1980**, *5*, 279.
- Maripuu, R.; Reineck, I.; Ågren, H.; Nian-Zu, W.; Rong, J. M.; Veenhuizen, H.; Shamma, S. H.; Karlsson, L.; Siegbahn, K. *Mol. Phys.* **1983**, *48*, 1255.
- McCarthy, M. I.; Rosmus, P.; Werner, H. J.; Botshwina, P.; Vaida, V. *J. Chem. Phys.* **1987**, *86*, 6693.
- Miller, W. H. *Dynamics of Molecular Collisions, Part B*; Plenum Press: New York, 1976.
- Moore, C. E. *Atomic Energy Levels*; National Bureau of Standards: Washington, DC, 1971.
- Mordaunt, D.; Ashfold, M. N. R.; Dixon, R. N. *J. Chem. Phys.* **1996**, *104*, 6460.
- Müller, J.; Ågren, H. *J. Chem. Phys.* **1982**, *76*, 5060.
- Nangia, S.; Truhlar, D. G. *J. Chem. Phys.* **2006**, *124*, 124309.
- Ni, T.; Lu, Q.; Ma, X.; Yu, S.; Kong, F. *Chem. Phys. Lett.* **1986**, *126*, 417.
- Ni, T.; Yu, S.; Ma, X.; Kong, F. *Chem. Phys. Lett.* **1986**, *128*, 270.
- Nielsen, A.H.; Nielsen, H.H. *Phys. Rev.* **1935**, *47*, 585.
- Pitzer, K. *Acc. Chem. Res.* **1979**, *12*, 271.
- Potts, A. W.; Price, W. C. *Proc. R. Soc. London Ser. A.* **1972**, *326*, 181.
- Pütz, N.; Heinecke, H.; Veuhoff, E.; Arens, G.; Heyen, M.; Lüth, H.; Balk, P. *J. Cryst. Growth* **1984**, *68*, 194.
- Pyykkö, P.; Desclaux, J.-P. *Acc. Chem. Res.* **1979**, *12*, 276.
- Ranu, R.; Peyerimhoff, S. D.; Buenker, R. J. *J. Mol. Spectrosc.* **1977**, *68*, 253.
- Rich, R. *Periodic Correlations*; W. A. Benjamin: New York, 1965.

- Rosmus, P.; Botschwina, P.; Werner, H. J.; Vaida, V.; Engelking, P. C.; McCarthy, M. I. *J. Chem. Phys.* **1987**, *86*, 6677.
- Ruscic, B.; Berkowitz, J. *J. Chem. Phys.* **1993**, *99*, 5840.
- Sam, C. L.; Yardley, J. T. *J. Chem. Phys.* **1978**, *69*, 4621.
- Sans, J.; Gallarta, F.; Glaban, J.; *Anal. Chem.* **1988**, *330*, 510.
- Schnieder, L.; Meier, W.; Welge, K. H.; Ashfold, M. N. R.; Western C. M. *J. Chem. Phys.* **1990**, *92*, 7027.
- Schroeder Laboratory Notebook; *WPS 002-067*
- Schroeder Laboratory Notebook; *WPS 002-108*
- Scoles, G. *Atomic and Molecular Beam Methods*; Oxford University Press: New York, 1988, Vol. 1.
- Shinke, R. *Photodissociation Dynamics*; Cambridge University Press: Cambridge, 1993.
- Shinke, R. *Photodissociation Dynamics*. *John Wiley & Sons* [online publication]. CPA11. <http://www.wiley.com/legacy/wileychi/ecc/samples/sample03.pdf>
- Simmons, J. P. *J. Phys. Chem.* **1984**, *88*, 1287.
- Smith-Freeman, L. A.; Schroeder, W. P.; Wittig, C. *J. Phys. Chem. A* **2009**, *113*, 2158.
- Thayer, John S. *J. Chem. Educ.* **2005**, *11*, 1721
- Vaida, V.; McCarthy, M. I.; Engelking, P. C.; Rosmus, P.; Werner, H. J.; Botschwina, P. *J. Chem. Phys.* **1987**, *86*, 6669.
- Wallenstein, R. *Opt. Commun.* **1980**, *33*, 119.
- Walsh, A. D. *J. Chem. Soc.* **1953**, 2296.
- Wittig, C.F. *unpublished manuscript*.
- Wiza, J. L. *Nuclear Instruments and Methods*, **1979**, *162*, 587.

Xie, X.; Schnieder, L.; Wallmeier, H.; Boettner, R.; Welge, K. H.; Ashfold, M. N. R.  
*J. Chem. Phys.* **1990**, *92*, 1608.

Xuan, C. N.; Margani, A. *J. Chem. Phys.* **1994**, *100*, 7000.

Zhang, J.; Dulligan, M.; Wittig, C. *J. Phys. Chem.* **1995**, *99*, 7446.

Zhang, J.; Dulligan, M.; Wittig, C. *J. Phys. Chem.* **1997**, *107*, 1403.

Zhang, J.; Riehn, C. W.; Dulligan, M.; Wittig, C. *J. Chem. Phys.* **1996**, *104*, 7027.